Dissertation
submitted to the
Combined Faculties of the Natural Sciences and Mathematics
of the Ruperto-Carola-University of Heidelberg, Germany
for the degree of
Doctor of Natural Sciences

Put forward by
Nikolay M. Kacharov, MSc
Born in: Sliven, Bulgaria
Oral examination: 04 February 2015

Chemical abundances and kinematic properties
of Galactic globular clusters

Referees: Dr. A. Koch
              Dr. S. Reffert

Abstract

High-resolution spectroscopic studies of globular clusters (GC) have been a major break-through in our understanding of these ancient stellar systems. The observations carried out in the last decade revealed a very heterogeneous population of objects – not only have GCs undergone a complex star formation history resulting in large chemical inhomogeneities common amongst all of them, but there are also non-negligible cluster-to-cluster differences in both chemistry and kinematics that are not yet fully understood. In this thesis, we present the first ever high-resolution studies of two poorly known GCs M 75 and NGC 4372. M 75 is a massive, relatively metal-rich, outer halo GC with extremely broad horizontal branch. We found that, besides the typical light-element variations, it shows a marginal spread in metallicity and likely has a small s-process rich population. Surprisingly for its metallicity, the majority of the analysed stars lack s-process enrichment, which hints to a formation in an environment that built metals very quickly. On the other hand, NGC 4372 is one of the most metal-poor GCs in the Galaxy. It is found in the inner halo and has experienced multiple disk crossings. The chemical analysis revealed it as a standard representative of the old, metal-poor halo group. More interesting are its structural and kinematic properties as the cluster has an unusually high intrinsic rotation for its metallicity and appears to be rotationally flattened. Furthermore, since GCs trace the chemical properties of their environment, the thesis also includes the first homogeneous study of the Galactic halo evolution of the poorly studied α element sulphur traced by GC stars covering a large metallicity span.

Zusammenfassung

Die Untersuchung von Kugelsternhaufen mittels hochaufgelöster Spektroskopie hat unser Verständnis dieser alten Sternsysteme revoluziniert. Derartige Beobachtungen im Verlauf des letzten Jahrzehnts förderten eine sehr vielfältige Population von Objekten zu Tage. Komplexe Sternentstehungsgechichten und damit verbundene große chemische Inhomogenitäten scheinen allen Kugelsternhaufen gemein zu sein. Jedoch gibt es auch nicht vernachlässigbare Unterschiede in den Elementhäufigkeiten und der Kinematik von Sternhaufen zu Sternhaufen, welche derzeit noch wenig verstanden sind. In dieser Arbeit zeigen wir die Ergebnisse der ersten hochaufgelösten Spekroskopischen Unterschuchung von zwei wenig unterschuchten Kugelsternhaufen, M 75 und NGC 4372. M 75 ist ein massereicher, relativ metallreicher Kugelsternhaufen im äußeren Halo mit einem extrem breiten Horizontalast. Neben den typischen Variationen in der Häufigkeit leichter Elemente zeigen meine Ergebnisse auch eine geringfügige Variation in der Metallizität in diesem Sternhaufen und Hinweise auf eine kleine s-Prozess-reiche Population. Ungewöhnlich für die Metallizität von M 75 weist die Mehrzahl der untersuchten Sterne kein s-Prozess Anreicherung auf. Dies deutet darauf hin, dass der Haufen in einer Umgebung entstand, in der die Anreicherung mit Metallen sehr schnell vonstatten ging. Im Kontrast dazu ist NGC 4372, im inneren Halo nahe der Galaktischen Scheiben, einer der metallärmsten Galaktischen Kugelsternhaufen. Die Analyse seiner Elementhäufigkeiten zeigt den Haufen als typischen Vertreter der alten, metallarmen Halo-Population. Ungewöhnlicher sind seine Struktur und Kinematik, denn es zeigt sich, dass der Haufen für seine Metallizität eine ungewöhnlich hohe intrinsische Rotation sowie Rotationsabflachung aufweist. Kugelsternhaufen zeichnen die chemische Entwicklung ihrer Umgebung nach. In diesem Zusammenhang zeigt diese Arbeit ausserdem die erste homogene Analyse der Entwicklung des wenig untersuchten α-Elements Schwefel im Galaktischen Halo anhand von Sternen in Kugelsternhaufen, die einen grossen Metallizitätsbereich abdecken.

Contents

1

Introduction

1.1 The Galactic globular cluster system

Similar to many giant galaxies, the Milky Way hosts a large population of about 150 known globular clusters (GC) extending out to more than 100 kpc (Harris 1996) and there are likely a few more, yet to be discovered (e.g. Ivanov et al. 2005). The GCs are massive, dense, old, stellar systems, typically containing from several ten thousand to several hundred thousand stars born at roughly the same time more than 10 Gyr ago and sharing the same primordial chemical signature of the environment they were formed in (Figure 1.1). However, as it will be discussed further in this thesis, all of them, studied to date, have undergone complex processes of chemical self-enrichment that altered the abundances of some chemical elements in the majority of their stars. Furthermore, the interplay of internal (stellar collisions, close encounters, energy equipartition, and relaxation processes) and external (tidal interactions) forces substantially changed their structure and kinematics, making it difficult to trace back their initial properties.

It is with no doubt that the Galactic GCs have attracted a lot of attention with the advancement of astronomical instruments and observational techniques due to their relative proximity and suitability for stellar evolution studies. Moreover, with ages of $10 - 14$ Gyr, GCs represent the oldest stellar systems in the Galaxy and therefore reflect its earliest evolutionary stages. Many such systems were likely involved in the assembly of the Milky Way itself.

The Galactic GCs, however, do not represent a homogeneous system of objects. While the majority of them belong to the Galactic halo, some clusters are associated kinematically with the Galactic bulge and disk. The latter are predominantly (but not exclusively) metal-rich (van den Bergh 1999). But even if the Galactic halo GC system appears homogeneous (e.g. Cohen & Meléndez 2005; Koch et al. 2009) and well compatible with the stellar halo in many regards, including chemical composition (e.g. Pritzl et al. 2005; Geisler et al. 2007), numerous properties show broad differences between individual clusters and several sub-populations can be identified.

About a quarter of all halo GCs are associated with the "outer Galactic halo" (van den Bergh & Mackey 2004) – a vaguely distinct stellar component of the Milky Way halo found at galactocentric distances typically larger than ~ 15 kpc, exhibiting a different spatial density profile, stellar orbits, metallicities, and possibly a different origin through dissipationless, chaotic merging of low mass systems, similar to present day low-luminosity dwarf spheroidal galaxies (dSph Zinn 1993, 1996;
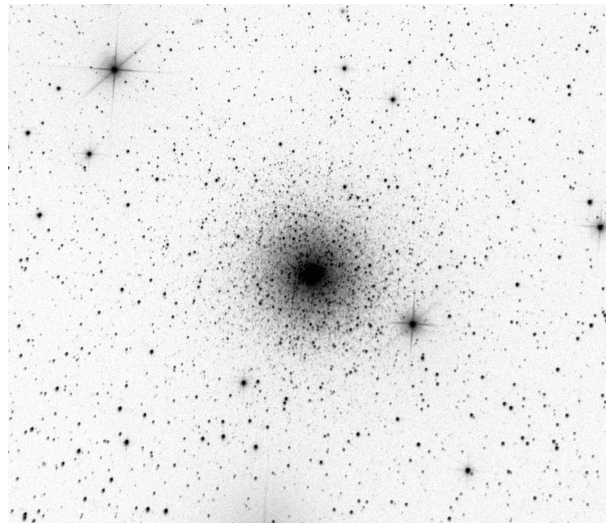
Figure 1.1: An image of the GC M 15 obtained by me during the Astronomy Summer School "Beli Brezi" in Bulgaria in 2007.

Carollo et al. 2007; An et al. 2012). The inner and outer GC halo groups appear to follow two different age-metallicity relations (e.g. Marín-Franch et al. 2009; Leaman et al. 2013; VandenBerg et al. 2013) and many of the outer halo GCs are found to be $1-2$ Gyr younger than the typical, old, inner halo clusters, as prompted by different horizontal branch (HB) morphologies of GCs of the same metallicity (e.g. Dotter et al. 2010) – an effect well known as the "second parameter problem", which needs to explain discordant HB morphologies at any given metallicity. Suggested solutions to this problem include a broad age range amongst the GCs (Searle & Zinn 1978) or variations in their helium content (e.g. D'Antona et al. 2002), while mass loss, α-abundances, rotation, deep mixing, binary interactions, core concentration, or planetary systems cannot be ruled out as possible second parameters (see Catelan 2009, for a detailed review). Coupled with the lack of a metallicity gradient in the outer halo GC system, the outer halo clusters second parameter problem has prompted the first suggestion by Searle & Zinn (1978) and further work by Mateo (1996); Côté et al. (2000); Mackey & Gilmore (2004); Lee et al. (2007); Marín-Franch et al. (2009); Forbes & Bridges (2010) that those GCs could have been donated by accreted dwarf galaxy-like systems. This scenario is further supported by the observations of GCs donated by the currently disrupting Sagittarius dSph galaxy (Ibata et al. 1995). The presumably *in situ* born, old GCs of the inner halo, on the other hand, probably formed during the early dissipative collapse of the proto-Galactic halo, as suggested by Eggen et al. (1962) and in accordance with the modern understanding of galaxy formation within the ΛCDM cosmological model (Blumenthal et al. 1984; Bundy et al. 2005; Governato et al. 2007).

For a long time GCs were considered as true examples of simple stellar populations. In the last couple of decades, however, an increasing abundance of evidence revealed a very complex nature of these objects - all GCs studied to date contain multiple stellar populations with distinct chemistry (see reviews by Gratton et al. 2004, 2012a, and references therein) and kinematics (Bekki 2010; Lardo et al. 2011; Bellazzini et al. 2012; Richer et al. 2013). First noticed by Osborn (1971), the observed chemical inhomogeneities include large variations in the abundance of light elements Li, C, N, O, F, Na, Al, and sometimes Mg. The abundances of these elements show strong correlations with each other (see the right panel of Figure 1.2 and Carretta et al. 2009b,c; Lardo et al. 2012a,c). In Figure 1.2 the stars with typical halo-like chemistry (e.g. low Na and high O) are marked with blue and are often referred to as the "primordial population". On the other hand, the stars with modified chemical abundances (e.g. high Na and low O) are marked with red and are only found
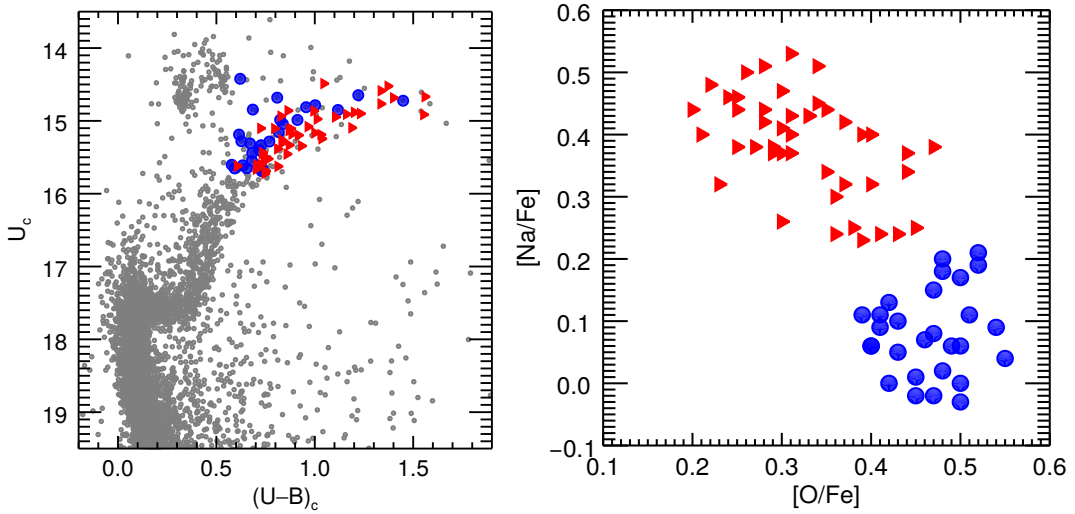
Figure 1.2: *Left panel:* A differentially dereddened U-B, U CMD of the GC M 4 showing the separation of Na-rich (red triangles) and Na-poor (blue dots) stars in the RGB of the cluster. Note the presence of a few AGB stars. *Right panel:* The Na-O anticorrelation in M 4. The photometric and abundance data is taken from Marino et al. (2008). The dereddening of the CMD is performed as described in Chapter 3.

in GCs. Such large chemical inhomogeneities are not found amongst open clusters and have been proposed as a defining property of a GC (Carretta et al. 2010). Sometimes spreads amongst the n-capture elements are also observed (Marino et al. 2009; Carretta et al. 2011b; Kacharov et al. 2013). These chemical anomalies are tightly related to multiple populations observed in the GC colour-magnitude diagrams (CMD Piotto et al. 2007; Marino et al. 2008; Piotto et al. 2012; Piotto et al. 2014). Depending on the choice of photometric filters (Sbordone et al. 2011), we often observe multiple main sequences (MS), extended turn-off regions, broadened red giant branches (RGB), and extended HBs. The complex CMDs of GCs are commonly attributed to significant variations of the He content (D'Antona et al. 2005; Renzini 2008), the C, N, and O abundances (Yong et al. 2008; Ventura et al. 2009; Yong et al. 2014), and/or some age spread (Gratton et al. 2012b). Figure 1.2 gives an example for a clear separation between the Na-poor (halo-like chemistry) and Na-rich (modified chemistry) stars in the RGB of M 4. The difference is most pronounced in the $U - B$ colour where strong NH, CN, and CH molecular bands are present in the spectrum. Furthermore, the abundance variations of light-elements, which are efficient electron donors, change the opacity of the stellar atmospheres. When the opacity is increased, the continuum flux is coming from upper, cooler layers and hence the star appears redder.

Although the general picture of chemical inhomogeneities in GCs seems to be ubiquitous, differences are observed from cluster-to-cluster. The unique properties of individual GCs seem to be driven mainly by their total mass but metallicity, age, and possibly other parameters also play a role and need to be better understood. The chemical inhomogeneities are an integral part of the second parameter problem and hold important clues about the formation and early evolution of GCs.

1.2 Multiple populations and possible formation scenarios

Most likely the elevated abundances of the light-elements in GCs are produced through proton capture reactions during the hot bottom hydrogen burning phases of massive asymptotic giant branch (AGB) stars ($M > 4 - 5$ $M_\odot$) or the hydrostatic hydrogen burning in massive ($M > 8$ $M_\odot$) stars, when the CNO, NeNa ($T_c > 20 \times 10^6$ K), and possibly the MgAl ($T_c > 70 \times 10^6$ K) cycles are

simultaneously in operation. Since He is the direct outcome of these reactions, the chemically en-riched stars[1] are also He enriched. Abundance variations are also observed amongst MS GC stars (Harbeck et al. 2003; Lardo et al. 2012a) and thus, it is now established that the unique chemistry of GCs is coming from external pollution with nuclear processed material, rather than a result of stellar evolution (e.g. dredged up material from the cores of evolved stars; see Briley et al. 1994; Gratton et al. 2001, for discussion). Moreover, the low-mass stars simply do not reach the core temperatures, necessary to alter the light element abundances. Likewise, the chemical peculiarities cannot be only due to surface contamination since they would be erased after the first dredge-up and they are found amongst all stellar evolutionary stages. Note that there are indications that no pol-luted stars are present in the AGBs of some clusters but this could be because the extreme HB stars (He rich and associated with the enriched population) fail to ascend the AGB and evolve straight to the white dwarf cooling sequence (Campbell et al. 2013; Charbonnel et al. 2013). To this day, however, the nature of the polluters and early evolution of GCs remain a mystery.

Several formation scenarios have been put forward competing to explain the chemically peculiar (or polluted) GC stars but they all face still unsolved problems and challenges. The most promising sources of pollution with p-capture elements while producing only little or no α- and Fe-peak-elements are the winds of massive ($\sim 4 - 11\,M_\odot$) AGB and super-AGB stars (D'Antona et al. 2002; D'Ercole et al. 2008; Pumo et al. 2008; Bekki 2010), or winds of fast rotating massive ($M > 20\,M_\odot$) stars (FRMS Prantzos & Charbonnel 2006; Decressin et al. 2007) and massive binaries (De Mink et al. 2009). Both mechanisms work on very different timescales: The winds of FRMS and binary stars enrich the interstellar medium (ISM) with p-capture products in $\sim 6 \times 10^6$ yrs, slightly before the explosions of the bulk of SNe II take place. On the other hand, the long-lived AGB stars take a few 10^8 yrs before they enrich the ISM with these elements (Gratton et al. 2012a). An article by Valcarce & Catelan (2011) attempts to combine both mechanisms. A problem in all theories is the small fraction of primordial, unenriched stars ($\sim 30\%$) with respect to the polluted stars ($\sim 70\%$) in present-day GCs, since the observed mass of the primordial population is not sufficient to supply enough processed gas into the ISM to form the numerous, enriched population by a factor of ~ 10 (D'Ercole et al. 2008). For both mechanisms to work, one has to either invoke a top-heavy initial mass function (IMF) for the primordial population, a truncated IMF for the polluted population, so that only low mass stars were formed, or to assume that the GCs were much more massive and they lost a large fraction of their primordial population. In the last year, a new idea was proposed that relies on a single burst of star formation and accounts for multiple problems in the previous models - "The accretion disk scenario" (Bastian et al. 2013b, detailed explanation below).

A successful GC formation scenario must meet a number of constraints stemming not only from the most recent photometric and spectroscopic observations of the Galactic GC population but also from GCs and young massive clusters[2] in external galaxies. Following Bastian et al. (2013b), the successful model has to address the following points:

i) The chemically enriched population is more centrally concentrated (Lardo et al. 2011);

ii) Na-O anticorrelations of different extent should be reproduced correctly in different clusters, e.g. the model has to allow variations in the observed abundance spreads in order to explain cluster-to-cluster differences (Carretta et al. 2009b);

iii) All GCs show large Al spreads but only a handful, specifically the more massive and/or metal-poor GCs have some Mg spread (Carretta et al. 2009c);

iv) Multiple, *discrete* MS and broad (bimodal or trimodal) HBs, likely caused by different He

---

[1]In this work, we refer to the stars that have been polluted with nuclear processed material as chemically enriched or polluted stars. They are enhanced in N, Na & Al and depleted in C & O. Likewise, we call primordial or unenriched the stars with typical halo-like chemistry (low Na, N, & Al, and enhanced in O, & C).

[2]This assumes that the same processes should be at work in young massive (up to $10^7\,M_\odot$) clusters as well, otherwise the model should state why this is not the case.

content (Piotto et al. 2007), and split subgiant branches (SGB) and RGBs in UV filters (Sbordone et al. 2011), possibly caused by total CNO variations (Yong et al. 2008, 2014) or individual C and N abundance variations (Lardo et al. 2012a) are observed in many GCs, while the spectroscopic studies show *continuous* abundance spreads. Note, however, that in most GCs the total CNO abundance is preserved constant (Cohen & Meléndez 2005);

v) Allow for small Li variations (Monaco et al. 2012);

vi) Iron and iron-peak elements have constant abundances or show very small spreads increasing with the cluster mass (Carretta et al. 2009a)[3], e.g. no SNe enriched material participates in the formation of the enriched GC stars;

vii) Allow for small variations in the n-capture elements in some clusters. A spread in the r-process element abundances has been detected in several metal-poor GCs (e.g. Roederer 2011; Roederer & Sneden 2011) and attributed to inhomogeneities of the gas cloud from which they formed. However, variations of s-process element abundances seem to be a result of the cluster's self-enrichment (Yong & Grundahl 2008; Villanova et al. 2010; Marino et al. 2011; Carretta et al. 2011b; Kacharov et al. 2013);

viii) Explain the large fraction of polluted stars ($\sim 70\%$ are enriched with nuclear processed material), while satisfying the mass-budget within the cluster. Larsen et al. (2012, 2014b) showed that the metal-poor GCs in the Fornax dwarf spheroidal galaxy, which also show abundance variations, could not have been more than 5 times more massive at birth than they are now. Similar conclusions apply for the GCs in the WLM and IKN dwarf galaxies (Larsen et al. 2014a). There are simply not enough metal-poor stars in the fields of these galaxies to account for a severe mass loss from their GCs;

ix) Intermediate-age ($1 - 3$ Gyr), populous clusters in the Large Magellanic Cloud (LMC) do not show abundance variations (Mucciarelli et al. 2008; Colucci et al. 2012), while the old LMC GCs do have them (Mucciarelli et al. 2009). Moreover, no young clusters (< 300 Myr) with masses up to 10^5 M$_\odot$ in the LMC (Bastian & Silva-Villa 2013) and 10^7 M$_\odot$ in other galaxies show multiple bursts of star formation or age variations of more than 30 Myr (Bastian et al. 2013a). Observations show that no gas is retained in massive clusters older than 3 Myr (Bastian et al. 2013a);

We briefly outline the accomplishments, advantages, and problems of the existing models.

• **The AGB scenario.** The AGB scenario is perhaps the most developed theoretical interpretation of the observed chemical inhomogeneities in GCs. The massive AGB stars were first proposed by Cottrell (1981); D'Antona et al. (1983) as candidate polluters. D'Ercole et al. (2008) and subsequent works by the same group carried out comprehensive hydro-dynamical and N-body simulations to test the plausibility of the model. The AGB stars reach the high temperatures to ignite hydrogen burning at the bottom of their convective envelopes (hot bottom burning) and undergo the nucleosynthesis reactions producing the altered abundances. The efficient mixing of their interiors, and the substantial mass loss through slow winds allow the enriched ejecta to remain in the potential well of the cluster and accumulate in the centre, where a new, centrally concentrated generation of stars can form. However, the formation of a second generation from pure AGB ejecta would result into a Na-O correlation, instead into the observed anticorrelation. To overcome this problem, some dilution with pristine gas is additionally required. Different dilution models also allow for cluster-to-cluster differences in their chemical patterns and naturally explain the observed continuous abundance spreads, while maintaining discrete He populations as observed in the MS of some GCs. In the limited mass range around 4 M$_\odot$ (at lower masses hot bottom burning is not possible), the stars may also experience a third dredge-up episode and bring s-process elements and carbon (hence increasing the total CNO abundance) to the surface. The yields of the super-AGB

---

[3]The most massive GCs with large Fe-spreads like ω Cen and M 54 might have completely different origin and are often considered to be the nuclear star clusters of disrupted dwarf galaxies rather than genuine GCs.

stars ($9 - 11$ M$_\odot$) can produce the observed extreme He abundances in some clusters (Pumo et al. 2008).

The AGB scenario, however, also faces a number of problems and drawbacks. For instance, in order to form such a numerous second generation of stars from the primordial one, the clusters must have been $10 - 100$ times more massive than we see them now. Although the preferential loss of a large number of stars from the first generation in the early evolution of the cluster and the subsequent mixing through two-body relaxation processes have been proposed to be at work, we still lack a convincing mechanism of such an efficient mass loss shortly after the GC formation. We note here in passing that it is extremely difficult to recognize chemically normal GC stars that are lost to the Milky Way halo because they bear the same chemical signature as genuine field stars. Martell & Grebel (2010) and Martell et al. (2011) surveyed the Galactic halo for polluted GC stars and found that they make only $2 - 3\%$ of the halo and if such a substantial GC mass loss has taken place, then at least 17% of the halo stars should have originated in GCs. And while the Milky Way halo has the potential to accommodate the possible large fraction of lost GC stars, this is not the case for dwarf galaxies that host GCs (see above discussion). An alternative idea is that all GCs were born in the centres of now disrupted larger systems like dwarf galaxies and accumulated yields of a much larger AGB population (Bekki et al. 2007). While, it is indeed possible that this is the case for the most massive Milky Way GCs like ω Cen, M 54, and possibly M 22, they all show spreads in iron and have therefore also been able to retain gas enriched from SNe ejecta. There is also not a good explanation of where the pristine gas needed for dilution is coming from. The SNe II ejecta should have removed all gas from the cluster potential since we do not see their signature in the enrichment pattern of the second generation. The in-fall of pristine gas on a later stage has been suggested as a possible solution. This brings us to the next problem, namely that the AGB scenario requires a delayed and/or continuous star formation epoch ranging from ~ 50 to ~ 300 Myr after the formation of the first generation but there is no evidence for continuous star formation in any young massive cluster to date, nor is observed any star-forming cluster of similar mass in this age regime (Bastian et al. 2013a, and references therein). There are a number of $1 - 3$ Gyr old LMC clusters with extended or double turn-off regions (Milone et al. 2009), which could be explained by an age spread of $400 - 500$ Myr (Goudfrooij et al. 2009), in good agreement with predictions of the AGB scenario. Surprisingly, however, it is now established that these clusters are good representatives of simple stellar populations where no chemical peculiarities have been detected (Mucciarelli et al. 2008, 2014; Colucci et al. 2012).

• **The spin stars scenario.** The scenario was first proposed by Prantzos & Charbonnel (2006) and put on a more quantitative basis by Decressin et al. (2007). The FRMS (often also called spin stars) are particularly interesting candidate polluters since they can directly produce the observed abundance anticorrelations without the need of dilution with pristine gas and naturally predict high He enrichment. Some dilution is still required to explain the Li abundances in GC stars, though, since their ejecta must be Li-free, considering the high-temperatures in their cores. These stars can reach critical rotational velocities, existing on the brink of disruption, already at the MS. The large angular momentum leads to a very efficient rotational mixing, which brings CNO processed material from the core and the associated substantial low-velocity mass-loss helps to eject the material into the ISM. On a time scale of ~ 6 Myr the enriched gas accumulates in the cluster and the eruptions of the majority of SNe II, which take place on a similar time scale, trigger a new star formation episode, leading to a second, chemically enriched generation of GC stars. This scenario assumes the presence of a large number of massive stars that had a significant amount of rotation already at birth and the angular momentum did not dissipate through stellar winds until the stars reached critical velocities. There are some indications that dense stellar environments favour fast stellar rotation (Strom et al. 2005; Huang & Gies 2006). The FRMS scenario also suffers from

a severe mass-budget problem to form the numerous second generation and fails to explain the discrete He-populations found in the MS of some GCs.

• **The massive binaries scenario.** In this scenario, a second generation of GC stars is formed from the ejecta of massive binary stars. Massive binaries, where one of the companion stars is filling its Roche lobe, form a common envelope and efficiently lose mass through the Lagrangian points L_1 and L_2 with low enough velocity, so that the lost mass remains in the cluster. According to Petrovic et al. (2005), binaries with initial periods of $3-6$ days lose $70-80\%$ of the transferred mass into the ISM. De Mink et al. (2009) demonstrated that their ejecta are He, N, Na, and Al enriched and depleted in C & O, hence bear the chemical signatures of polluted GC stars. Although, the current fraction of binaries in GCs is only a few percent, there are indications that it has been much higher for massive stars, up to $60-75\%$ (Sana et al. 2008; Mason et al. 2009). The biggest success of this model is that it manages to significantly reduce the mass-budget problem, owing to the much larger number of stars, compared to the previously discussed scenarios, that can contribute with chemically polluted material. Under the extreme assumption that all massive stars capable to produce the required chemical enrichment were in binaries, segregated in the centre of the proto-GC, and that the transferring material companion lost its entire envelope, and assuming some pristine gas dilution (needed for Li), De Mink et al. (2009) manage to create an equally populous second generation of stars. While the AGB models naturally predict the Mg-Al anticorrelation, a potential drawback of any massive stars model are the Mg spreads observed in some GCs, since the majority of massive stars (spin stars or binaries) do not reach the necessary high temperatures for Mg depletion in the layers that would be normally mixed through convection. Note, however, that models of stars exceeding $40M_\odot$ do predict a weak Mg-Al anticorrelation that could be made stronger under some assumptions of the nuclear reaction rates and the isotopic distribution of Mg (Decressin et al. 2007; De Mink et al. 2009). This might explain why Mg-variations are rather an exception in GCs than a norm.

• **The accretion disk scenario.** While the discussed above models introduced new types of polluters but always invoked the formation of multiple generations of stars through several starburst events, the "Accretion disk scenario" proposes a new mechanism for the pollution of the chemically peculiar stars within a single burst of star formation. Bastian et al. (2013b) put forward the idea that ejecta of massive binaries and spin stars can be swept up by the accretion disks of the still forming, low-mass pre-MS stars. Stars with initial masses of 0.5, 1, & 2 $M_\odot$ have pre-MS life-times of 90, 25, & 6 Myr, respectively (Siess et al. 2000), consistent with the time-scale of pollution from massive binaries and spin stars. Bastian et al. (2013b) assume a gas-free cluster with a Kroupa (2001) IMF with a primordial mass-segregation (see Portegies Zwart et al. 2010), so that the polluter stars are concentrated in the centre. The still forming low-mass, pre-MS stars that pass through or live in the central regions of the cluster (estimated to be roughly half of all pre-MS stars) sweep up the enriched material onto their proto-stellar disks, which is then accreted onto and mixed within their highly convective envelopes. The different amount of time that the stars spend in the central region determines the amount of pollution they will get and hence, the model allows for continuous spreads in the light-element abundances. The model predicts that stars in the outer parts of the cluster on radially anisotropic orbits should be more enriched than stars on circular orbits. An evidence supporting that prediction was recently provided by Richer et al. (2013) for the GC 47 Tuc. The higher mass stars have lost their accretions disks earlier and do not participate in the enrichment process. Thus, only low-mass stars can be polluted, which removes the mass-budget problem, as the mass of the ejected, polluted gas is sufficient to form the enriched population observed in nowadays GCs without forcing very strong constraints on the polluters as is the case in the De Mink et al. (2009) scenario. The most extreme abundances require that the star accreted half of its mass. Moreover, this explains why we do not see abundance variations

in young and intermediate-age clusters, as our data comes primarily from more massive stars. We should be able, however, to detect different He-populations in the MS of these clusters if we acquire deep enough, high-quality CMDs. The model also offers an elegant solution to the Li problem; in the multiple generation scenarios formed entirely from the ejecta of massive stars, the second generation has to be Li-free, which is in contrast to the observations; in the accretion disk scenario, the stars are already in place at the time of the accretion of the Li-free, enriched material and the primordial Li abundance of the star is only mildly depleted.

Possible caveats of the model are connected to the survival time of the accretion disks and the efficiency of the necessary convective mixing. In the Solar neigbourhood, the accretion disk life-times are in the order of $5-15$ Myr in low-mass stars (Haisch et al. 2001; Bell et al. 2013) but the dense environment of the early GCs might have been much more hostile to the circumstellar disks, leading to quicker destruction. A follow up study by D'Antona et al. (2014) showed that the accreting star does not remain fully convective during the entire period of accretion. The authors argued that accretion of polluted gas is only possible in the first $2-3$ Myr after the formation of the proto-stellar disk, which would greatly reduce the amount of accreted gas and hence revitalise the mass-budget problem.

1.3 The current dynamical state of GCs – structure and internal kinematics

In this section, we outline some of the most common models describing the dynamical processes that lead to the present day morphology and internal kinematics of GCs. After the violent relaxation in the early evolution due to SNe eruptions, gas loss, and rapid expansion, the current dynamical state of GCs is dominated by two-body relaxation processes taking place on a Hubble time-scale. Therefore, the GCs reach a quasi-relaxed state, characterised by a velocity distribution function not far from Maxwellian. They are generally viewed as spherically symmetric, successfully described to first order by spherical, isotropic models (see e.g. Trager et al. 1995; McLaughlin & van der Marel 2005).

• **Plummer models.** Power law stellar density profiles have been proven to be successful in describing massive star clusters (EFF models Elson et al. 1987). In the line of sight projection the EFF models describing the the surface density $\mu(r)$ as a function of radius can be summarised with the following expression:

$$\mu(r) = \mu_0 \left(1 + \frac{r^2}{a^2}\right)^{-\gamma/2}, \tag{1.1}$$

where a is the scale radius and μ_0 the central surface brightness. They are characterised by a roughly constant density near the core region and approaching zero at large radii. The case of $\gamma = 4$ is known as the Plummer model and is perhaps the best studied because of its simple analytic properties (Plummer 1911). Assuming a single-mass, single particle (no binary stars) cluster the scale-radius a is practically the half-light radius. This can be shown by integrating Equation 1.1 in the case of a Plummer sphere:

$$\frac{\int_0^{2\pi} \int_0^a \mu(r)\, r\, dr\, d\varphi}{\int_0^{2\pi} \int_0^\infty \mu(r)\, r\, dr\, d\varphi} = \frac{1}{2}. \tag{1.2}$$

The deprojection of the stellar density is reduced to simply substituting γ in Equation 1.1 with $\gamma+1$. For the Plummer family the deprojected stellar density $\rho(r)$ is given by:

$$\rho(r) = \rho_0 \left(1 + \frac{r^2}{a^2}\right)^{-5/2}. \tag{1.3}$$

Solving the Poisson equation

$$\nabla^2 \Phi = 4\pi G \rho \tag{1.4}$$

gives the potential of the Plummer sphere:

$$\Phi = -\frac{GM}{\sqrt{r^2 + a^2}}, \tag{1.5}$$

as in Binney & Tremaine (1987), from where we can derive simple formulae for the mass distribution $M(r)$ and the velocity dispersion $\sigma(r)$ as a function of radius:

$$M(r) = \frac{4}{3}\pi \rho_0 r^3 \left(1 + \frac{r^2}{a^2}\right)^{-3/2}, \tag{1.6}$$

$$\sigma^2(r) = \frac{2\pi G \rho_0 a^2}{9\sqrt{1 + \frac{r^2}{a^2}}}. \tag{1.7}$$

The Plummer models are successful in describing the inner parts (within a few half-light radii) of some well-behaved GCs (e.g. without central cusps) as we show in Chapter 3 but they start to deviate from the observations at large radii, since GCs are tidally truncated systems. The power-law family of models intrinsically assumes an infinite density profile.

● **King models.** The King family of models are the best known and widely used GC models. King (1962) published an empirical formula describing the surface brightness of a GC as a function of radius:

$$\mu(r) = k \left[\frac{1}{(1 + (r/r_0)^2)^{1/2}} - \frac{1}{(1 + (r_t/r_0)^2)^{1/2}} \right]^2, \tag{1.8}$$

where r_0 is the natural scale-length of the model, referred to as a "core radius" and r_t is the "tidal radius" of the cluster – the distance at which the stellar density drops to zero. The empirical King models are therefore fully defined by the concentration parameter $c = \log(r_t/r_0)$. Provided that $r_t >> r_0$, the core radius is the radial distance at which the surface brightness is half of the central value. It is different from the half-light radius, which is defined as the radius, in which is contained half of the total light of the system. The GCs reside in the tidal field of the Milky Way (or other parent galaxies) and are thus tidally truncated systems. Stars that have large enough velocities can become unbound and leave the cluster by crossing the Roche surface – a hypothetical equipotential surface around the GC locked between the Lagrangian points L_1 and L_2, where the gravitational potential of the cluster is equal to the potential of the galaxy (Figure 1.3). The tidal radius is therefore a proxy for the more physical Jacobian radius (r_J) – the distance from the centre of the cluster to the Lagrangian points L_1 and L_2, which can be written with the following expression (as in Ernst & Just 2013):

$$r_J = \left(\frac{GM_{cl}}{\Omega^2 - \frac{d^2\Phi}{dR^2}} \right)^{1/3} \sim \left(\frac{M_{cl}}{M_G} \right)^{1/3} R, \tag{1.9}$$

where M_{cl} and M_G are the masses of the cluster and the Galaxy, respectively, Ω is the cluster's angular velocity, R is its the Galactocentric distance, and Φ is the gravitational potential of the Galaxy. Note that the observational, tidal radius is not exactly equal to the Jacobian radius for a number of reasons discussed in Binney & Tremaine (1987).

Although, the formula in Equation 1.7 is derived purely empirically, the King models have a solid physical interpretation (King 1966). Very similar profiles are predicted naturally by solving the
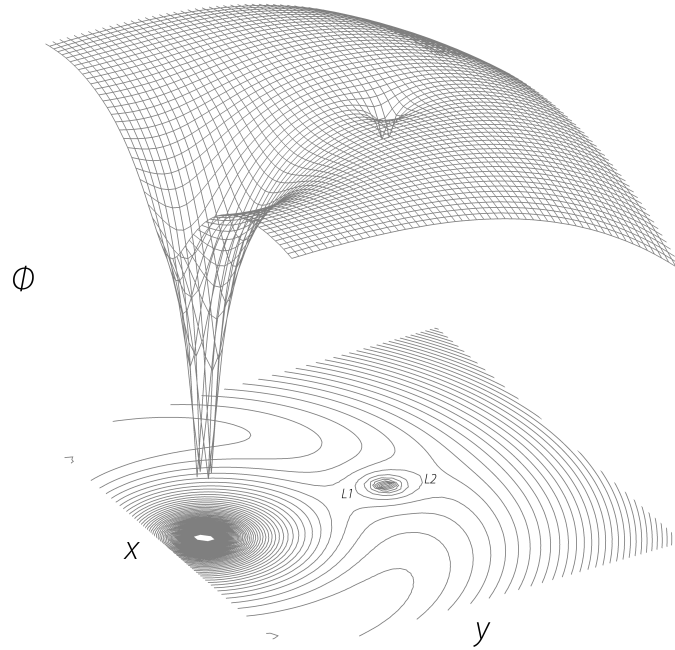
Figure 1.3: An illustration of the gravitational potential wells of the Galactic centre (deep dip) and an orbiting GC (shallower potential well). A 2-dimensional contour map of the gravitational potential in the bottom of the figure indicates the positions of the Lagrangian points L_1 and L_2. Stars outside the enclosed contour are no longer bound to the cluster.

Poisson equation assuming a truncated Maxwellian distribution (also called lowered Maxwellian) function in phase-space of the kind[4]:

$$f(E) \propto \begin{cases} \rho(2\pi\sigma^2)^{-3/2}(e^{-E/\sigma^2} - 1), & E < 0, \\ 0, & E \geq 0, \end{cases} \tag{1.10}$$

where E is the stellar energy, ρ is the stellar density as a function of radius, and σ is a velocity dispersion parameter. The dynamical King models cannot be expressed analytically and need to be computed numerically. They describe relaxed systems of equal-mass stars and isotropic velocity distribution.

The increasing abundance of observational data, however, has revealed noticeable deviations from this simple picture. McLaughlin & van der Marel (2005) showed that many GCs are more extended than the predictions of the tidally truncated King models arguing for the presence of unbound stellar halos or tidal streams. They demonstrated that isotropic Wilson (1975) models that assume a modified King distribution function, allowing for more extended profiles, are more suitable for these systems. Moreover, radial anisotropy (Ibata et al. 2013), significant degree of mass segregation (Da Costa 1982) caused by energy equipartition, signatures of core-collapse (a runaway collapse of the central regions of a GC caused by the diffusion of kinetic energy towards the outer regions Newell & Oneil 1978; Djorgovski & King 1984), velocity dispersion inflated by binaries (Bradford et al. 2011), and mild deviation from sphericity often associated with the presence of tidal

---

[4]The gravitational potential is linked to the phase-space distribution function $f(r,v,t)$ through the collisionless Boltzmann equation. According to the Jeans theorem, any function of the integral of motion is a solution to the collisionless Boltzmann equation. Models, in which the density distribution determines the potential of the system and vice versa are called self-consistent.

tails (White & Shawl 1987; Odenkirchen et al. 2001; Belokurov et al. 2006; Chen & Chen 2010) have been observed in many GCs. Additionally, significant amounts of internal rotation (Lane et al. 2011; Bellazzini et al. 2012; Bianchini et al. 2013) have been detected in most Milky Way GCs. This has motivated the development of dynamical models, including the effects of external tides, mass segregation, core-collapse, and binary stars (Gunn & Griffin 1979; Küpper et al. 2010; Zocchi et al. 2012) as well as a significant degree of rotation (Wilson 1975; Satoh 1980; Davoust 1986; van de Ven et al. 2006; Fiestas et al. 2006; Varri & Bertin 2012). These works demonstrated that internal rotation significantly accelerates the dynamical evolution of GCs. Most relevant for this thesis are the Varri & Bertin rotational models used in Chapter 3 to describe the dynamical state of NGC 4372, which we present here in more detail.

● **Rotating models.** Varri & Bertin (2012) developed self-consistent axisymmetric, rotating models with a distribution function based solely on the energy and z-component of the angular momentum. These models are defined such as they predict differential rotation – rigid in the core and vanishing in the outer parts of the system, where the energy truncation becomes effective. The velocity dispersion is isotropic in the central regions.

In the case of rigid rotation, the distribution function is similar to the distribution function of the isotropic King models, although instead of the energy E, in a rotating system the conserved quantity is the Jacobi integral $H = E - \omega J_z$, where ω is the angular velocity of the rigid rotation and J_z is the z-component of the angular momentum. In the limiting case of ($\omega \to 0$), the rigid models are reduced to the spherical King models. The predicted surface density profile has an elliptical shape – flattened in the equatorial plane. Pure rigid rotation models, however, are not physical and serve only as a basis for the development of more realistic differential rotation models.

In the case of differential rotating models, the integral of motion is given by:

$$I(E, J_z) = E - \frac{\omega J_z}{1 + b J_z^{2c}}, \tag{1.11}$$

where ω, b and $c > 1/2$ are positive constants. Since the integral is reduced to the Jacobi integral for small J_z, ω can be interpreted as a parameter denoting rigid angular momentum in the central regions of the cluster, while b and c determine the shape of the radial profile of the rotation profile. If the truncation in the phase-space is based solely on the energy of each star with respect to reference value E_0, the underlying distribution function can be written as

$$f(I) = \begin{cases} A e^{aE_0} [e^{-a(I-E_0)} - 1 + a(I - E_0)], & E < E_0, \\ 0, & E \geq E_0, \end{cases} \tag{1.12}$$

which is reduced to the distribution function of the spherical Wilson (1975) models in the limiting case of no rotation ($\omega \to 0$). The integration of the Poisson equation is done via an iterative procedure seeded by the solution for the spherical Wilson model. At variance with the rigid rotation model, the predicted surface density profile is more "boxy"-shaped in the centre – resembling a toroidal structure in the case of very rapid rotation.

The differentially rotating models predict realistic velocity dispersion profiles with pressure isotropy and radial anisotropy in the central and intermediate regions, respectively. Depending on the truncation parameters, the outer regions may have tangential anisotropy. Such tangential anisotropy is not generally predicted by equilibrium models but is observed in rapidly rotating GC, such as ω Cen (van de Ven et al. 2006). Additionally, it hints that tidal interactions may have implications on the presence of rotation, since stars on radial orbits are preferentially lost and thus tangential anisotropy is established (Baumgardt & Makino 2003). Differential rotation may also induce non-trivial gradients in the projected velocity dispersion profile. In this respect, internal rotation is an important effect to be taken into account when discussing the dynamical state of

a GC and issues such as the presence of a central black hole (e.g. Lützgendorf et al. 2013, and references therein). This family of models has been successfully applied to ω Cen, 47 Tuc, and M 15 (Bianchini et al. 2013). In this thesis, we extend this sample, including the slowly rotating GC NGC 4372.

1.4   Deriving chemical abundances from stellar absorption lines

One of the main aims of the present work is to measure element abundances in GC stars in order to investigate the aforementioned questions pertaining GC formation. Thus, we will briefly introduce the basic principles of deriving chemical abundances from stellar spectroscopy. We measure the chemical composition of a star by analysing the absorption lines of different chemical elements in the stellar spectrum. The absorption lines are formed from the combined effect of an ensemble of atoms that absorb photons with a defined energy and thus decrease the intensity of the radiation field (bound-bound transitions). The stellar atmospheres contain mainly hydrogen (X $\sim$ 74%) and helium (Y $\sim$ 24%), and only traces of heavier elements (Z), typically $<$ 2% of the total mass per volume for Sun-like stars but the precise quantities can vary broadly in different stellar populations. Namely, the heavier elements are responsible for the majority of spectral lines we observe in the photospheres of cool stars. By measuring absorption lines in the stellar spectrum, we are able to infer the column number density of a particular absorber (responsible for the formation of the line of interest) along the line of sight. Most often the element abundance is given in logarithmic scale, relative to the Solar abundance – the square bracket notation ([A/B]):

$$[A/B] = \log \frac{N_A}{N_B} - \log \frac{N_A^\odot}{N_B^\odot},$$ (1.13)

where N_A and N_B are the column number densities of element A and element B in the star and the Sun, respectively. The column number densities are often given per 10^{12} hydrogen atoms. So, our goal is to derive the number of absorbing atoms responsible for the formation of a particular spectral line and then compute the total abundance of this element. Besides on the chemical abundance of the element, the intensity of the spectral lines depends on the physical conditions in the stars (e.g. effective temperature, gravity, microturbulence velocity) and on specific properties of the quantum transition (most importantly, the excitation potential and the oscillator strength of the transition). Generally, some quantum transitions are more probable than others. Transitions can be spontaneous or triggered by collisions or other environmental effects, such as electric and magnetic fields. The probability for a transition between two energy levels is determined by the Einstein coefficients: A_{21} gives the probability for a spontaneous emission, B_{21} gives the probability for a stimulated emission, and B_{12} gives the probability for a photo-absorption. The Einstein coefficients can be expressed as the net effect of an ensemble of quantum harmonic oscillators. Thus, the oscillator strength is a dimensionless quantity, which gives the effective number of quantum oscillators that have the same probability for a particular transition as the absorbing atom. To understand the impact of the physical conditions on the line intensity, we need to know which are the most probable/populated energy levels in the absorbing atom, what are the probabilities for transition, what is the relative number of atoms at different ionisation states, and what is the velocity distribution of the gas particles.

The electron distribution in the atoms is governed by a fundamental result of the statistical mechanics – higher energy levels are less probable than lower energy levels. The number of atoms in stellar atmospheres is so large that the probability distribution of different quantum states is practically equal to the number of absorbers. The number ratio of atoms in two energy levels

$E_b > E_a$ is determined by Boltzmann's equation:

$$\frac{n_b}{n_a} = \frac{g_b}{g_a} e^{-(E_b - E_a)/kT}, \tag{1.14}$$

$k = 1.38 \times 10^{-16}\,\mathrm{erg\,K^{-1}}$ is the Boltzmann constant, T is the gas temperature, and g is the statistical weight, which reflects the energy degeneracy of the different quantum states ($g_n = 2n^2$ gives the number of states that have energy E_n). Note that, according to the Boltzmann's equation, we need temperatures in the order of 85000 K to reach an equilibrium between the electrons on the first and second energy levels in the hydrogen atom but the Balmer lines (transitions from the second to higher energy levels) are strongest at temperatures around 10000 K, where we have much lower number of atoms in the first excitation state. To understand this, we have to look into the distribution of atoms at different ionisation states.

The number ratio of atoms at two different ionisation states n_i and n_{i+1} with ionisation energy χ_i is given by the Saha equation:

$$\frac{n_{i+1}}{n_i} = \frac{2u_{i+1}}{n_e u_i} \left(\frac{2\pi m_e kT}{h^2} \right)^{3/2} e^{-\chi_i/kT}, \tag{1.15}$$

where n_e is the electron density, h is the Planck constant, m_e is the mass of the electron, and u is the partition function. The partition function is the sum of possible energy states of the atom before and after ionisation. If E_n is the energy of level n, the partition function is defined as:

$$u = g_1 + \sum_{n=2}^{\infty} g_n e^{-(E_n - E_1)/kT}. \tag{1.16}$$

The factor of 2 in the Saha formula is due to the two possible spin numbers of the free electron. Half of the hydrogen atoms are ionised at a temperature ~ 9600 K and almost all of them are ionised at $T \sim 11000$ K, which explains the decrease of the Balmer lines intensity in hotter stars.

1.4.1 The line profile and spectral synthesis

Spectral synthesis is a common method for deriving chemical abundances. It requires proper modelling of the stellar atmospheres (the change of temperature, gas and electron pressure with optical depth, which govern the radiation transport) and understanding of the mechanisms that determine the intensity and shape of the absorption lines. The line profile is determined by $r_\lambda = F_\lambda/F_{cont}$, where F_λ is the flux in the line as a function of the wavelength and F_{cont} is the flux of the continuum. It contains a lot of information for the environment, in which the line forms. The opacity of the stellar atmosphere is highest in the centre of the line and decreases in the wings. In result, the centre of the line is formed in upper, cooler layers of the atmosphere, while the radiation from the wings reaches us from lower, hotter layers. There are three main processes that determine the broadening of the spectral lines:

• **Radiation damping**. The spectral lines have finite widths even in the idealised case when the atom is isolated and not in motion. This natural broadening is a consequence of the Heisenberg uncertainty principle $\Delta E \Delta t \sim h/2\pi$. The electrons remain a finite time Δt in excited states before leaving them. In result the energy levels are fuzzy (broadened). The ground state has the longest life time and is hence the least broadened. On the contrary, energy levels with high probability of transition are most affected by the radiation damping. The natural broadening is given by the following expression:

$$\Delta \lambda_E = \frac{\lambda^2}{2\pi c} \Gamma_{ik}, \tag{1.17}$$

where Γ_{ik} is the damping constant, which is defined by the Einstein coefficients for spontaneous radiation transitions. The line shape is determined by a Lorentzian profile with a width of $\Delta\lambda_E$.

• **Doppler broadening**. The atoms in the stellar atmosphere are in constant motion and their line of sight velocities cause an additional Doppler broadening of the line profile. For a gas in local thermodynamic equilibrium (LTE), the number of particles with a given velocity ($dn(v)$) in unit volume is constant and is described by the Maxwell-Boltzmann distribution:

$$dn(v) = \left(\frac{m}{2\pi kT}\right)^{3/2} e^{-mv^2/2kT} 4\pi v^2 dv, \tag{1.18}$$

where m is the mass of the particles. We can write the expression that determines the Doppler broadening using the Doppler effect and the most probable velocity $v_{mp} = \sqrt{2kT/m}$ according to to the Maxwell-Boltzmann distribution:

$$\Delta\lambda_D = \frac{2\lambda_0}{c}\sqrt{\frac{2kT\ln 2}{m}}. \tag{1.19}$$

Besides the thermal motion of the gas particles, there are also turbulent movements of large volumes of gas, especially in cool stars with convective envelopes. If the turbulent velocities on a micro-scale (microturbulence – the photons pass multiple gas cells before leaving the star) follow the Maxwell-Boltzmann distribution and their most probable velocity is v_{mic} we can write that

$$\Delta\lambda_D = \frac{2\lambda_0}{c}\sqrt{\left(\frac{2kT}{m} + v_{mic}^2\right)\ln 2}. \tag{1.20}$$

Since the projected on the line of sight Maxwellian distribution becomes Gaussian, the Doppler broadening is well described by a Gaussian profile with a width of $\Delta\lambda_D$. There might also be turbulent velocities on a macro-scale (macroturbulence) when the photons remain in a single gas cell from the time they are created until they leave the star. The net effect is a line broadening due to the convolution of multiple Doppler shifted spectra. The macroturbulence, however, does not change the line intensity.

• **Broadening due to particle collisions. Pressure effects.** The absorbing/emitting atoms are never isolated and the effect of the surrounding particles leads to an additional broadening of the lines - pressure effects. Common reasons for pressure broadening are the collisions between the particles. The transfer of energy from an excited atom to another particle shortens its average lifetime and leads to additional broadening of the energy levels. The line profile is the same as the natural line profile and described by a Lorentzian profile with a width of $\Delta\lambda_c$ but the broadening can be much larger:

$$\Delta\lambda_c = \frac{\lambda^2}{2\pi c} n\sigma\sqrt{\frac{2kT}{m}}, \tag{1.21}$$

where σ is the cross-section of the collision and n is the particle density. The presence of charged particles around the absorbing atoms also causes broadening due to the inverse Stark effect and perturbation by van der Waals forces.

The Doppler broadening dominates the central regions of the line but when moving away from the central wavelength, its effect decreases quickly and the line wings are generally dominated by particle collisions and the radiation damping. Narrower lines are observed in the spectra of giant and supergiant stars due to the low density in their expanded atmospheres. The pressure effects are responsible for the broad lines in MS stars.

Most commonly, the spectral lines are modelled with a Voigt profile, which is a probability density function resulting from a convolution of a Gaussian (responsible for the Doppler broadening)
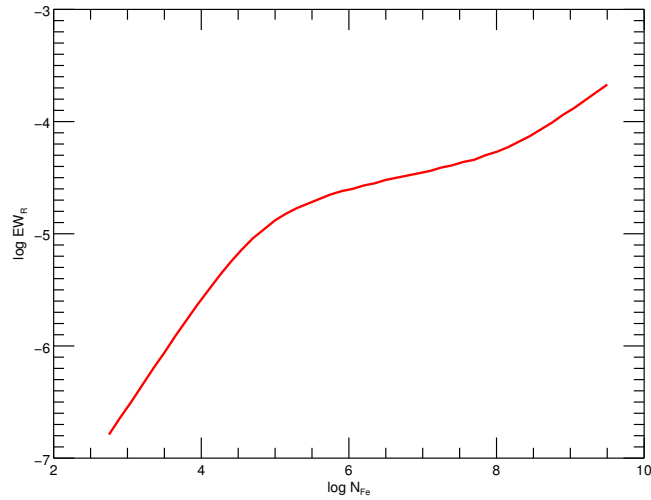
Figure 1.4: Curve of growth of the Fe I line at 5957 Å in a typical RGB star with $T_{eff} = 4150$ K, $\log g = 0.9$ dex, and $v_{mic} = 2.1$ km s^{-1}.

and a Lorentzian (responsible for the broadening due to particle collisions and radiation damping) profiles. Finally, the intensity of the spectral line is proportional to the number of absorbers, which we can estimate by fitting a synthetic line that takes into account all described effects to the observed spectrum. The total number of atoms of a particular chemical element can then be computed using the Boltzmann and Saha equations.

1.4.2 Equivalent widths and the curve of growth

A different approach to derive the chemical abundance from a stellar spectrum is to use the equivalent widths (EW) of the lines instead of synthesising their profiles. The latter can be computationally expensive and the line profiles can be very complex, modified by stellar rotation, macroturbulence, or motions of unknown origin. Furthermore, in reality, the observed line profile is a convolution between the intrinsic shape of the line and the spectrograph broadening function. With limited spectral resolution, a lot of the information encoded in the line profile is lost. The EW is an integral property of the line, which quantifies its intensity. It is defined as the width of a rectangle, which has the height of the continuum level and area equal to the area covered by the spectral line and is invariant to the above effects:

$$EW = \int_{-\infty}^{+\infty} \frac{F_{cont} - F_\lambda}{F_{cont}} d\lambda. \tag{1.22}$$

The curve of growth determines the theoretical EW as a function of the number of absorbers. In Figure 1.4 we have plotted the rise of the reduced EW ($EW_R = \log EW/\lambda$) of the Fe I line at 5957 Å as a function of the Fe abundance. The reduced EW is a wavelength independent estimate of the strength of the line. When the number of absorbers is small, the EWs rise linearly with increasing the element abundance. As the number of absorbers continues to grow the optical depth at the central wavelength becomes increasingly larger and leads to saturation of the line. This means that there are no more available photons to excite the atoms and the curve of growth forms a slowly rising plateau ($EW \propto \sqrt{\ln N_A}$) governed by the still optically thin line wings. The further increase of the number of absorbers leads to a significant increase of the optical depth away from the central

wavelength and to the formation of strong damping wings coming from increasingly deeper layers. The EW starts to grow again following $EW \propto \sqrt{N_A}$.

In an explicit form the curve of growth for any transition can be written by integrating the line profile and substituting with the Boltzmann and Saha equations to get the full element abundance (Gray 1992):

$$EW_R = \log C + \log N_A + \log gf\lambda - \theta_x \chi - \log \kappa_\nu, \tag{1.23}$$

where C is a constant specific for the star and the particular quantum transition, N_A is the number of atoms of element A relative to the number of hydrogen atoms, g is the statistical weight of the transition, f is the oscillator strength, $\theta_x = 5040/T$, χ is the excitation potential, and κ_ν is the continuum absorption coefficient. Note that a change of the elemental abundance is analogous to changes in the $gf\lambda$, $\theta_x \chi$, and κ_ν. Thus, curves of growth for different lines of the same species in the same star will only be shifted due to their individual χ, $\log gf\lambda$, and κ_ν but will have the same shape. Therefore, assuming we know the stellar atmosphere well, we can compute a generalised curve of growth for this star by adopting $\chi = 0$, $\log gf = 0$, $\lambda = \lambda_0$, and $\kappa_\nu = \kappa_0$ and vary only the abundance. Then, we can construct an empirical curve of growth by plotting the measured, reduced EWs of multiple lines of the same species against the known quantity $\Delta N_A = \log gf + \log(\lambda/\lambda_0) - \theta_x \chi - \log(\kappa_\nu/\kappa_0)$. A simple shift along the x-axis of the generalised curve of growth to the empirical curve of growth will give the real abundance of the element. The shape of the curve of growth is most significantly affected by the microturbulence, which tends to desaturate the spectral lines and is generally a free parameter in the abundance analysis. Generalised curves of growth incorporating different v_{mic} values can be then computed and the one that best describes the empirical curve of growth is considered representative for the star.

In practice, the atmospheric parameters are not well known. In this case a computation of a generalised curve of growth is not possible and we use an iterative procedure, where we derive the abundances from the individual curves of growth of all available lines by adopting a model atmosphere with effective temperature and gravity estimated from photometry, and empirical calibrations for the microturbulence velocity. Then the initial guess for the effective temperature is refined until all lines with different excitation potentials converge to the same abundance. The microturbulence velocity is inferred by removing any trend of the EWs of the various lines with the derived abundances. These steps are repeated until the derived abundances from all lines converge to a single value. Since the ionisation equilibrium is pressure sensitive, we can estimate the gravity by forcing the same abundance results from lines of different ionisation states of the element. If the distance to the star is known, however, as is the case with studying GCs, we can analyse separately neutral and ionised species, which should ideally converge to the same abundance. This is usually not the case due to departures from LTE (Heiter & Eriksson 2006; Lind et al. 2012; Bergemann et al. 2012), or an inappropriate choice of atmospheric models (e.g. using plane-parallel models, instead of spherical, or 3D models Bergemann et al. 2012).

Random errors arise from problems in measuring the EWs (e.g. blended lines) and poorly known atomic data but larger systematic errors come from uncertainties in the effective temperature (usually only known to a $100 - 150$ K precision), gravity, microturbulence, or inaccuracies in the model atmosphere. A way to deal with the poorly known atomic data is to perform a differential abundance analysis, where the EWs of the star of interest are directly compared to the EWs of a reference star with well known abundances and stellar parameters.

1.5   This thesis

The aim of this thesis is to study in detail the chemical and kinematic properties of Galactic GCs in order to put further constraints on their formation and evolution. We carry out detailed element

abundance measurements to look for chemical inhomogeneities and distinct multiple populations in poorly studied GCs and discuss the results in the framework of the existing GC formation scenarios. Detailed kinematic studies, on the other hand, are important to understand the long-term evolution of GCs and their current dynamical state. The thesis is organized as follows: Chapter 2 presents a comprehensive chemical abundance analysis of the massive GC M 75. Possible scenarios for the formation of the cluster are discussed in the frame-work of the models discussed in Section 1.2. Chapter 3 presents the structural and kinematic properties of the GC NGC 4372. The results are interpreted in the terms of elliptical Plummer and dynamical rotating models. We also discuss some possible relations of the amount of rotation in GCs with other structural and morphological properties. Chapter 4 is dedicated to the abundance analysis of NGC 4372. In Chapter 5, we investigate the behaviour of the poorly studied chemical element Sulphur in GC stars covering a large metallicity range. Chapter 6 summarizes the results of the thesis and gives an outlook.

2

A comprehensive chemical abundance study of the outer halo globular cluster M 75 [1]

2.1 Introduction

In this chapter we present the first ever chemical element abundances derived from high-resolution spectra for the GC M 75. The cluster is located at a galactocentric distance of 15 kpc, which tenants the transition region between the inner and outer Milky Way halo (Zinn 1993; Carollo et al. 2007). Its younger age ($\sim$ 10 Gyr; Catelan et al. 2002) and high metallicity ([Fe/H]$= -1.16$ dex, this work) are compatible with the properties of the outer halo GC system and suggest a possible extragalactic origin. On the other hand, M 75 is amongst the most concentrated GCs ($c = \log(r_t/r_c) = 1.80$), which could be contrasted to the extended and loose clusters in the outer halo (Koch & Côté 2010; Koch et al. 2009). This unique GC also has a trimodal horizontal branch (HB), the origin of which is not explicable under canonical stellar evolutionary models (Catelan et al. 2002). Apart from the well separated red HB (RHB) and blue HB (BHB), its CMD shows a distinct third extension of a very blue, faint tail. Moreover, it has an anomalously low ratio of RGB to HB stars, indicating higher He-content of the cluster. Thus, it is very important to assess possible multiple populations, which could be related to the peculiar HB morphology and to look for peculiarities in its chemical composition, which might reveal clues for its origin and early evolution.

2.2 Observations and data reduction

Our spectroscopic observations of 16 giant stars in M 75 were taken using the Magellan Inamori Kyocera Echelle (MIKE) spectrograph at the 6.5-m Magellan2/Clay Telescope at Las Campanas Observatory, Chile. The instrument consists of two arms sensible in the red and blue parts of the visible spectrum, which cover an entire wavelength range of 3340 Å to 9150 Å. Our data were collected over one night in April and four nights in July 2011. By using a slit width of 0.7$''$ and 2×1 binning of the CCD in spatial and spectral direction, we obtained a spectral resolution of approximately 30000. The typical seeing during the runs was $\sim 1''$ on average. We reached a

[1]The work presented in this chapter was done in collaboration with Andreas Koch and Andrew McWilliam. The results were published in Kacharov et al. (2013).

Table 2.1: Observing Log.

Star ID[1]	V_0 [mag]	Date	Exp. time [s]
239	15.04	Jul. 25 2011	3×1600
251	14.48	Jul. 23 2011	3×900
442	14.81	Jul. 26 2011	$1200 + 518$
461	14.29	Jul. 26 2011	2×800
483	14.84	Jul. 24 2011	3×1200
486	15.27	Jul. 25 2011	3×2000
503	14.30	Jul. 23 2011	1×2700
512	15.12	Jul. 25 2011	3×1600
583	14.19	Apr. 04 2011	2400
612	15.32	Jul. 26 2011	3×2000
655	14.84	Jul. 24 2011	3×1200
876	15.42	Jul. 26 2011	$2000 + 1600 + 3 \times 900$
901	14.71	Jul. 24 2011	3×1200
1251	15.10	Jul. 24 2011	$1600 + 1541$
1312	14.46	Jul. 23 2011	3×900
1459	14.70	Jul. 23 2011	3×1200

Notes. [1] Based on the catalogue of Kravtsov et al. (2007).

relatively high S/N of ~ 70 per pixel around 6500 Å on the red CCD and ~ 40 per pixel around 4500 Å on the blue CCD. The observing log is presented in Table 2.1. The targets were selected from the catalogue of Kravtsov et al. (2007), choosing stars with a high membership probability, i.e. those within the tidal radius of the cluster, yet avoiding the crowded central regions. This was aided by visual inspection of archival FORS preimaging (Program ID 69.B-0305, P.I. E. Tolstoy). A colour-magnitude diagram (CMD) of M 75, highlighting our spectroscopic sample, is presented in Figure 2.1. We also overplotted an isochrone of age 10 Gyr and metallicity $Z = 0.003$ from the Padova library (Girardi et al. 2010; Marigo et al. 2008), which best represents the photometric data. This adopts an extinction value $A_V = 0.49$ mag ($E(B-V) = 0.147$ mag) from Schlegel et al. (1998), and a distance modulus of $(m-M)_0 = 16.4$ mag (linear distance 19 kpc; Catelan et al. 2002). Our sample consists of 13 RGB stars and 3 possible AGB stars.

The data were processed with the MIKE pipeline reduction package (Kelson et al. 2000; Kelson 2003), which comprises flat field division, order tracing from quartz lamp flats, and wavelength calibration using built-in Th-Ar lamp exposures that were taken immediately following each science exposure. Continuum normalisation was performed by dividing the extracted spectra by a high-order polynomial fit to a spectrum of an essentially line-free hot rotating star, taken as part of our observing runs.

We computed the radial velocities of our targets by crosscorrelating the spectra with a synthetic RGB spectrum with stellar parameters similar to the target stars using the *fxcor* tool in IRAF. From this, we found a mean heliocentric velocity of -186.2 ± 1.9 km s^{-1}(standard deviation 8.1 km s^{-1}), confirming the cluster membership of all stars. This is in an excellent agreement with the mean systematic radial velocity of M 75 of -189.3 km s^{-1}, $\sigma = 10.3$ km s^{-1}(Harris 1996, 2010 version). Whilst this dispersion may seem large for a GC, it has to be kept in mind that M 75 is a very massive and concentrated system, so that this value is fully compatible with the large velocity dispersions found in other comparably luminous systems (Pryor & Meylan 1993).
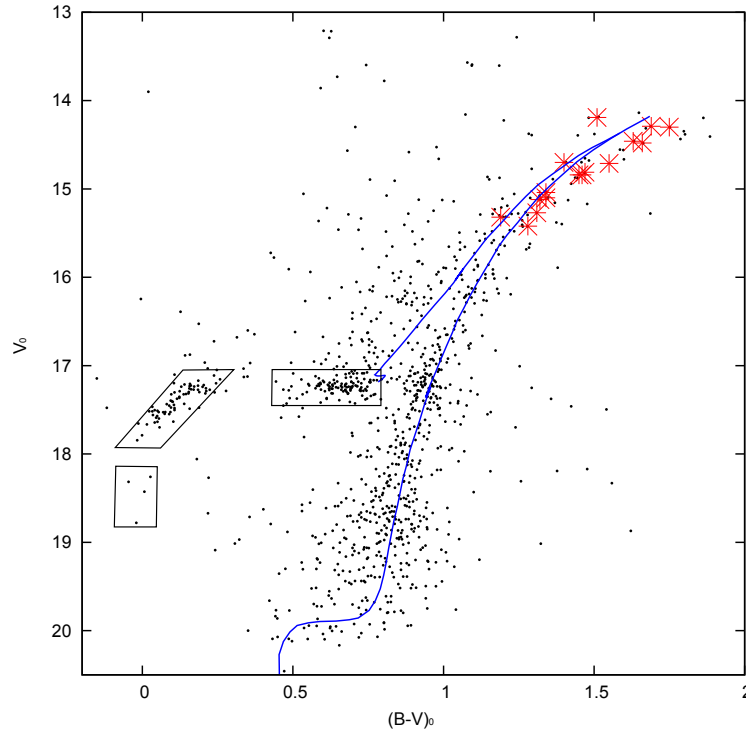
Figure 2.1: CMD from Kravtsov et al. (2007). The stars from our sample are indicated by larger red symbols. An isochrone for [Fe/H] ~ -1.2 dex and age of 10 Gyr from the Padova library (Marigo et al. 2008; Girardi et al. 2010) is overplotted for comparison. The three HBs are indicated by black rectangles.

2.3 Abundance analysis

2.3.1 Line list

We derived chemical element abundances through an EW analysis, complemented by spectral synthesis using the stellar abundance code MOOG (Sneden 1973). We used an absolute abundance analysis method, which closely follows the procedures described in Koch et al. (2009); Koch & Côté (2010). The line list was assembled from various sources (Koch & Côté 2010, and references therein), and complemented with atomic data from the Kurucz data base[2]. Additional transitions for some heavier elements were adopted from Sadakane et al. (2004) and Yong et al. (2008). The EWs of the lines were measured by fitting Gaussian profiles to the absorption features using the *splot* task in IRAF. We restricted our measurements to lines having reduced EWs less than -4.5 to avoid the saturated parts of the curves of growth. A major source of random error in the EWs estimates, especially in the bluer regions (below 5500 Å), comes from difficulties in placing the continuum due to the strong blending owing to the relatively high metallicity of M 75. We used the deblending option in IRAF's task *splot* to account for blended lines where necessary.

For the elements Rb, Zr, Gd, Dy, Er, Hf, and Th, we used spectral synthesis instead. Accurate EW measurements were not possible because of strong blending, too weak lines, or too low S/N ratio.

We applied corrections for Hyperfine Structure (HFS) splitting for the odd-Z elements V, Mn, Co, Cu, Rb, La, and Eu using the *blends* driver of MOOG and atomic data for the splitting from McWilliam et al. (1995); McWilliam et al. (2013). HFS corrections for Sc and Ba were small

---

[2]http://www.cfa.harvard.edu/amp/ampdata/kurucz23/sekur.html

Table 2.2: Line list and equivalent widths.[1]

Element	λ [Å]	χ [eV]	log gf	EWs [mÅ] for each star										
				#239	#251	#442	#461	#483	#486	#503	#512	#583	#612	...
[OI]	6300.31	0.00	-9.819	58	63	30	100	31	21	59	51	53	...	
[OI]	6363.79	0.02	-10.303	23	27	18	47	13	6	32	31	42	...	
Na I	5682.63	2.10	-0.700	86	142	141	111	143	109	131	82	105	98	
Na I	6154.23	2.10	-1.560	19	58	64	40	73	43	61	28	36	33	
Na I	6160.75	2.10	-1.260	31	77	82	64	102	66	79	26	49	44	
Mg I	5528.42	4.35	-0.357	199	247	214	233	221	206	243	199	227	206	
Mg I	5711.09	4.33	-1.728	113	147	129	126	127	122	136	111	124	104	
Al I	6696.03	3.14	-1.347	23	69	87	50	76	54	47	24	46	40	
Al I	6698.67	3.14	-1.647	...	32	40	20	39	26	24	...	20	22	
Al I	7835.31	4.02	-0.649	13	39	46	30	52	38	35	17	23	30	
Al I	7836.13	4.02	-0.494	17	49	56	33	60	47	36	20	26	35	
Si I	5684.48	4.95	-1.650	46	55	56	40	70	56	47	45	50	49	
Si I	5948.55	5.08	-1.230	69	67	79	69	81	72	60	66	57	70	
Si I	6155.13	5.61	-0.750	49	48	50	55	49	48	50	55	45	53	
Ca I	5261.71	2.52	-0.580	126	173	152	175	144	121	158	120	153	114	
Ca I	5590.13	2.52	-0.570	124	166	139	166	145	120	140	120	134	114	
Ca I	5601.29	2.53	-0.520	131	183	163	188	145	127	175	133	171	120	
Ca I	5857.46	2.93	0.230	147	182	166	150	159	142	176	146	163	128	
Ca I	6166.44	2.52	-1.140	96	129	113	141	120	99	133	97	120	77	
Ca I	6169.04	2.52	-0.800	120	152	145	144	133	126	150	114	139	102	
Ca I	6169.56	2.52	-0.480	132	169	146	179	150	139	173	134	158	128	
Ca I	6455.60	2.52	-1.290	89	110	100	112	101	92	117	80	110	70	
Ca I	6471.67	2.52	-0.875	122	162	149	157	151	126	162	124	154	118	
Ca I	6499.65	2.52	-0.820	123	155	138	160	135	123	149	116	145	100	
Ca I	6717.69	2.71	-0.610	146	193	170	188	170	152	188	142	180	137	
...														

Notes. [1] The full table is available in electronic form at the CDS via `http://cdsarc.u-strasbg.fr/viz-bin/qcat?J/A+A/554/A81`.

compared to the 1σ measurement uncertainty and we ignored them. HFS corrections for the lighter odd-Z elements are generally negligible.

Finally, the derived abundances were placed on the solar scale of Asplund et al. (2009). The full linelist and the measured EWs are available online. The first rows and columns of this table are presented to guide the eye (Table 2.2).

2.3.2 Stellar atmospheres

We interpolated the new grid of Kurucz[3] plane-parallel, one-dimensional models without convective overshoot. These include the α-enhanced opacity distribution functions (AODFNEW; Castelli & Kurucz 2003)[4].

As an initial guess, we calculated effective temperatures of our targets based on the $(V-I)_0$ colours from the photometric catalogue of Kravtsov et al. (2007). This was complemented with photometry from 2MASS to obtain temperature-estimates based on the $(V-J)_0$, $(V-H)_0$, and $(V-K)_0$ colour indices. We used the temperature-colour calibrations of Ramírez & Meléndez (2005). Additionally, we obtained spectroscopic temperatures by measuring the EWs of a large number, typically about 60, Fe I lines and establishing excitation equilibrium. This is achieved by changing the temperature until there is no correlation between the derived abundances from different Fe I lines and their excitation potential. As a result, the mean temperature from all three 2MASS based indicators is lower than the temperature based on the $(V-I)_0$ colour alone and the spectroscopic

---

[3] `http://www.cfa.harvard.edu/grids.html`
[4] `http://wwwuser.oat.ts.astro.it/castelli`
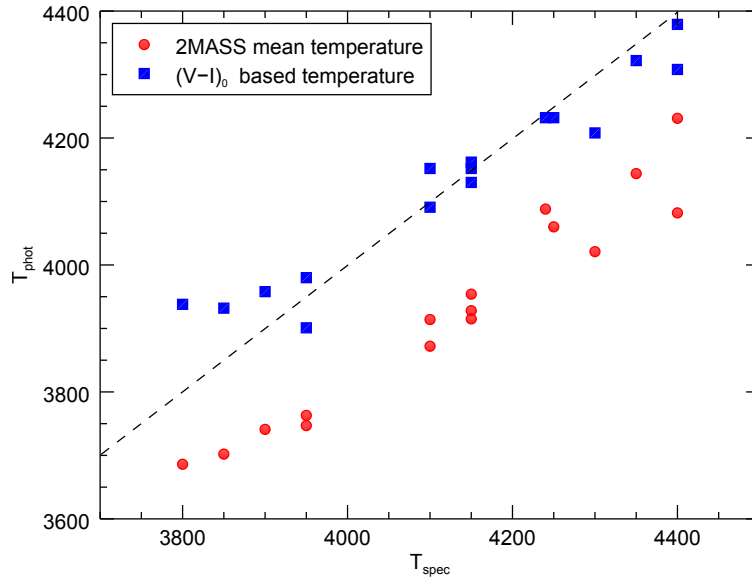
Figure 2.2: A comparison between the spectroscopic and photometric temperature estimates. The average temperature calculated from $(V-J)_0$, $(V-H)_0$, and $(V-K)_0$ colours is indicated by red circles and the $(V-I)_0$ calibration is indicated by blue squares. The dashed line is unity.

estimates by 200 K on average (Figure 2.2). A similar trend was also noted by Fabbian et al. (2009). One possible explanation is the larger pixel size of the 2MASS detectors, which can lead to an undersampling in the crowded GC field compared to better sampled optical images. This way, additional flux contributions per pixel would yield overestimated infrared magnitudes and thus lower effective temperatures. We use the spectroscopic temperatures in the following analysis. The mean difference between the temperatures from the $(V-I)_0$ colours and the spectroscopic ones is only 2 K with a 1σ-scatter of 60 K, which we adopted as the temperature error for our targets.

We derived physical gravities from the canonical Equation 2.1, using the dereddened V_0 magnitudes with a bolometric correction interpolated from the Kurucz grid, the spectroscopic temperatures, and adopting the known distance to the cluster (19 kpc). We adopted a mass $\mu = 0.78 \, M_\odot$ for all stars, which is consistent with the masses from the reference isochrones. Adopting lower masses for the possible AGB stars in our sample would lead to a small change in gravity, which would have a negligible effect on the derived abundances (See Section 3.3).

$$\log g = \log(\mu/\mu_\odot) + 4\log(T/T_\odot) - 0.4(M_\odot - M) + \log g_\odot \tag{2.1}$$

In the above equation, $M = M_V - BC$ denotes the absolute bolometric magnitude of the stars. We did not adjust the gravities to enforce ionisation equilibrium. As a result, the abundances from the Fe II lines are higher by 0.18 dex ($\sigma = 0.10$ dex) on average, compared to the neutral species (Figure 2.3). We note that the differences are larger for cooler stars, which might be due to the use of plane-parallel models instead of spherical or 3D ones (Bergemann et al. 2012), departure from LTE (Heiter & Eriksson 2006; Bergemann et al. 2012; Ruchti et al. 2013), or unknown blends. Additionally, the use of iron lines with a broad range of excitation potentials (from 1 to 5 eV) could also cause some discrepancy, as noted by Worley et al. (2010) and Worley & Cottrell (2010). The discrepancy in Fe I vs. Fe II is too large to be explained by systematic errors. Shifting the gravities by 0.5 dex would restore ionisation equilibrium, but this implies more than a 50% error in the distance to the cluster, which is rather unlikely. A change in the interstellar extinction towards M 75 by $\Delta E(B-V) = 0.35$ mag or an increase of the temperature scale by 100 K (200 K for the coolest stars) will also restore ionisation equilibrium. We deemed both possibilities unlikely, given
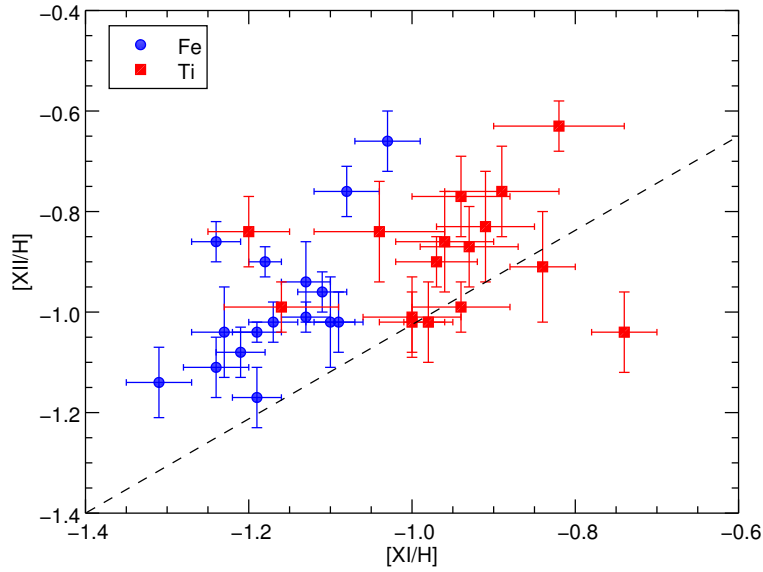
Figure 2.3: A comparison between the abundance results from neutral and ionised species. Fe abundances are shown with blue circles and Ti abundances with red squares. The dashed line is unity.

the large, required changes compared to the small uncertainties in the parameters and our overall excellent excitation equilibrium. Likewise, the Ti abundances from the ionised species are larger than the ones based on Ti I lines by 0.07 dex ($\sigma = 0.15$ dex).

Microturbulent velocities (ξ) were determined by removing any trend in the plot of abundances versus EW of the Fe I lines. The derived values for M 75 are in the order of 2.1 km s^{-1}. A typical error of this method is ~ 0.1 km s^{-1}: variations within this range still allow reasonably flat slopes in the EW plot.

Since we did not have a prior knowledge of the metallicities of the individual stars, we started with atmosphere models for [M/H] $= -1.2$ dex, as representative for the cluster mean (Catelan et al. 2002), and updated it iteratively based on the Fe I estimates from the previous step. Note that all the parameters were iterated upon convergence. The derived stellar parameters for all 16 red giants are summarized in Table 2.3.

2.3.3   Abundance errors

We calculated the random error of the abundances as $\sigma_{EW}/\sqrt{N}$, where N is the number of lines used for those elements where we measured more than one line and σ_{EW} is the standard deviation. For those elements, for which we used the EW of a single line, we adopted a typical random error based on the mean abundance spread of all stars in our sample. For the abundances derived via synthesis, we adopted random errors based on the minimum and maximum abundance values that still yielded acceptable fits to the observed spectra.

To investigate the systematic abundance errors caused by the uncertainties of the stellar atmosphere parameters, we calculated a grid of new model atmospheres, varying the effective temperature by ± 60 K, the surface gravity by ± 0.2 dex, the microturbulent velocity by ± 0.1 km s^{-1} and the metallicity by ± 0.1 dex for three stars spanning a large difference in their parameters. We also included calculations for Solar [α/Fe] ratios using the Kurucz ODFNEW models (column labeled 'ODF' in Table 2.4). Then we recomputed the abundances of all elements with the modified atmosphere models. The results are summarized in Table 2.4 in terms of difference to the default values. The column labeled *total* lists the errors of all parameters combined in quadrature, including a

Table 2.3: Stellar parameters.

Star ID	T_{eff}^{2MASS} [K]	$T_{eff}^{(V-I)}$ [K]	T_{eff}^{spec} [K]	log g $\log[\mathrm{cm\,s^{-2}}]$	ξ [km s^{-1}]	[Fe I/H] [dex]	[Fe II/H] [dex]
239	4021	4208	4300	1.07	2.1	-1.19 ± 0.03	-1.17 ± 0.06
251	3741	3958	3900	0.49	2.2	-1.08 ± 0.04	-0.76 ± 0.05
442	3914	4152	4100	0.82	2.1	-1.13 ± 0.03	-0.94 ± 0.08
461	3686	3938	3800	0.31	2.1	-1.03 ± 0.04	-0.66 ± 0.06
483	3928	4162	4150	0.87	2.0	-1.10 ± 0.03	-1.02 ± 0.09
486	4082	4308	4400	1.23	2.1	-1.09 ± 0.03	-1.02 ± 0.06
503	3702	3932	3850	0.36	2.3	-1.24 ± 0.03	-0.86 ± 0.04
512	4060	4232	4250	1.07	2.0	-1.19 ± 0.03	-1.04 ± 0.02
583[1]	3747	3901	3950	0.42	2.2	-1.24 ± 0.04	-1.11 ± 0.06
612[1]	4231	4379	4400	1.25	2.1	-1.18 ± 0.02	-0.90 ± 0.03
655	3954	4152	4150	0.87	2.1	-1.21 ± 0.03	-1.08 ± 0.05
876	4144	4322	4350	1.26	2.0	-1.13 ± 0.03	-1.01 ± 0.03
901	3872	4091	4100	0.78	2.1	-1.11 ± 0.03	-0.96 ± 0.04
1251	4088	4232	4240	1.05	2.4	-1.23 ± 0.04	-1.04 ± 0.09
1312	3763	3980	3950	0.53	2.4	-1.31 ± 0.04	-1.14 ± 0.07
1459[1]	3915	4130	4150	0.81	2.1	-1.17 ± 0.03	-1.02 ± 0.04

Notes. [1] Possible AGB stars.

0.1 dex uncertainty in [α/Fe]. The latter corresponds to 1/4 of the abundance difference between the AODFNEW and ODFNEW Kurucz models. We note, however, that these are upper limits due to the covariance of the atmospheric parameters (e.g. McWilliam et al. 1995).

The change in temperature has a larger effect on the species with a lower excitation potential (e.g. K I, Ti I, V I, Cr I), while the change in gravity affects mostly the ionised species. For warm GK giants the dominant Fe II species are more sensitive to gravity and the Fe I species to changes in temperature. But we note that the stars studied here, especially the coolest stars of our sample, have so low temperatures that they are in the transition from Fe being dominated by the ionised species to Fe dominated by the neutral species. That is why Fe II is so sensitive to variations of the effective temperature in this case. We note that our prior ignorance of the metallicity of the model atmospheres has only a negligible effect on the derived abundances. The overall, typical, systematic uncertainties are of the order of 0.1 dex.

Table 2.4: Systematic abundance errors.

Ion	ΔT_{eff}		$\Delta \log g$		$\Delta \xi$		Δ[M/H]		ODF	total
	+60 K	−60 K	+0.2 dex	−0.2 dex	+0.1 dex	−0.1 dex	+0.1 km/s	−0.1 dex		
					#461					
Fe I	−0.02	+0.01	+0.02	−0.06	−0.08	+0.06	+0.03	−0.02	−0.12	0.09
Fe II	−0.14	+0.14	+0.06	−0.13	−0.03	+0.03	+0.08	−0.00	−0.18	0.18
O I	+0.02	−0.02	+0.07	−0.08	−0.01	+0.01	+0.05	−0.03	−0.15	0.10
Na I	+0.06	−0.05	−0.02	+0.01	−0.01	+0.02	0.00	+0.01	−0.01	0.06
Mg I	−0.01	+0.02	0.00	−0.03	−0.04	+0.05	+0.02	+0.01	−0.05	0.05
Al I	+0.04	−0.04	−0.01	0.00	−0.01	+0.01	0.00	0.00	−0.02	0.04
Si I	−0.07	+0.08	+0.02	−0.06	−0.01	+0.02	+0.05	+0.01	−0.09	0.09
K I	+0.06	−0.06	0.00	−0.02	−0.10	+0.09	+0.02	−0.01	−0.18	0.12
Ca I	+0.07	−0.05	−0.01	+0.01	−0.06	+0.08	+0.02	+0.01	−0.08	0.10
Sc II	−0.01	+0.02	+0.06	−0.08	−0.03	+0.05	+0.06	−0.01	−0.13	0.09
Ti I	+0.09	−0.07	+0.02	−0.01	−0.07	+0.08	+0.02	−0.01	−0.13	0.12
Ti II	−0.03	+0.02	+0.04	−0.05	−0.05	+0.04	+0.05	−0.01	−0.12	0.08
V I	+0.09	−0.09	+0.02	−0.02	−0.07	+0.06	+0.03	−0.03	−0.14	0.12
Cr I	+0.07	−0.07	0.00	−0.01	−0.08	+0.07	+0.01	−0.01	−0.10	0.11
Mn I	+0.02	0.00	+0.02	−0.04	−0.07	+0.08	+0.04	0.00	−0.09	0.09
Co I	+0.01	0.00	+0.04	−0.05	−0.07	+0.09	+0.05	−0.01	−0.11	0.10
Ni I	+0.01	−0.01	+0.04	−0.06	−0.05	+0.05	+0.04	−0.01	−0.11	0.08
Cu I	+0.01	0.00	+0.04	−0.06	−0.08	+0.09	+0.05	−0.01	−0.12	0.11
Zn I	−0.07	+0.07	−0.01	−0.03	−0.04	+0.04	+0.03	+0.02	−0.05	0.09
Y II	0.00	0.00	+0.05	−0.07	−0.04	+0.04	+0.04	−0.02	−0.13	0.08
Ba II	+0.01	0.00	+0.06	−0.07	−0.10	+0.12	+0.06	−0.02	−0.17	0.14
La II	+0.02	−0.02	+0.06	−0.07	−0.03	+0.04	+0.05	−0.02	−0.13	0.09
Ce II	+0.01	0.00	+0.06	−0.07	−0.01	+0.02	+0.04	−0.02	−0.12	0.08
Pr II	+0.02	−0.02	+0.03	−0.07	−0.03	+0.02	+0.04	−0.03	−0.13	0.08
Nd II	+0.01	−0.01	+0.05	−0.06	−0.06	+0.06	+0.05	−0.02	−0.13	0.09
Sm II	+0.02	−0.02	+0.05	−0.05	−0.05	+0.06	+0.04	−0.01	−0.12	0.09
Eu II	−0.01	+0.01	+0.06	−0.08	−0.02	+0.02	+0.05	−0.02	−0.14	0.09
					#612					
Fe I	+0.05	−0.05	+0.01	−0.03	−0.06	+0.05	0.00	−0.01	−0.04	0.08
Fe II	−0.08	+0.08	+0.08	−0.12	−0.03	+0.03	+0.03	−0.04	−0.14	0.14
Na I	+0.04	−0.05	−0.01	+0.01	−0.02	+0.01	−0.01	0.00	+0.02	0.05
Mg I	+0.04	−0.04	−0.01	0.00	−0.03	+0.03	0.00	+0.01	0.00	0.05
Al I	+0.04	−0.05	−0.01	0.00	−0.01	0.00	−0.01	0.00	+0.01	0.05
Si I	−0.02	+0.03	+0.03	−0.04	−0.01	+0.02	+0.02	−0.01	−0.05	0.05
K I	+0.11	−0.10	+0.01	−0.01	−0.06	+0.07	−0.01	+0.02	−0.04	0.13
Ca I	+0.06	−0.07	−0.02	0.00	−0.05	+0.04	−0.02	+0.01	0.00	0.08
Sc II	−0.02	+0.01	+0.06	−0.10	−0.04	+0.03	+0.03	−0.03	−0.11	0.10
Ti I	+0.12	−0.13	0.00	0.00	−0.04	+0.04	−0.01	+0.01	−0.01	0.13
Ti II	−0.02	+0.02	+0.06	−0.09	−0.05	+0.05	+0.02	−0.03	−0.11	0.10
V I	+0.11	−0.12	+0.01	+0.01	−0.01	+0.01	0.00	+0.01	0.00	0.12
Cr I	+0.11	−0.11	0.00	+0.01	−0.05	+0.06	−0.01	+0.02	0.00	0.12
Mn I	+0.09	−0.09	+0.01	−0.01	−0.05	+0.06	0.00	+0.01	−0.02	0.11
Co I	+0.07	−0.05	+0.03	−0.02	−0.02	+0.04	+0.02	0.00	−0.03	0.07
Ni I	+0.04	−0.04	+0.03	−0.04	−0.03	+0.03	+0.01	−0.01	−0.05	0.06
Cu I	+0.06	−0.05	+0.03	−0.03	−0.06	+0.07	+0.01	−0.01	−0.04	0.09
Zn I	−0.04	+0.04	+0.04	−0.07	−0.03	+0.03	+0.02	−0.02	−0.07	0.08
Y II	−0.01	+0.01	+0.07	−0.08	−0.03	+0.05	+0.03	−0.03	−0.10	0.09
Ba II	+0.02	−0.02	+0.07	−0.09	−0.08	+0.09	+0.03	−0.03	−0.14	0.13
La II	+0.01	−0.01	+0.08	−0.08	−0.01	+0.02	+0.04	−0.03	−0.11	0.09
Ce II	0.00	0.00	+0.08	−0.08	−0.01	+0.01	+0.03	−0.03	−0.10	0.09
Pr II	+0.01	−0.02	+0.07	−0.09	−0.01	+0.01	+0.03	−0.04	−0.11	0.09
Nd II	0.00	−0.01	+0.07	−0.09	−0.03	+0.03	+0.03	−0.04	−0.11	0.10
Sm II	+0.01	−0.01	+0.08	−0.08	−0.01	+0.02	+0.04	−0.03	−0.09	0.09
Eu II	−0.02	+0.01	+0.07	−0.10	−0.01	+0.01	+0.03	−0.04	−0.12	0.10

2.4 Abundance results

In Table 2.6 we summarize the abundance results for M 75, relative to Fe I for all neutral species and to Fe II for all ionised species. We also list the mean random error, ε_{rand}, and the mean systematic error, ε_{sys}, on the abundance ratios [X/Fe]. The columns labeled σ_{obs}^{16} and σ_{obs}^{13} contain the observed spreads of the abundances within the cluster. As noted above, the discrepancy between Fe I and Fe II values are largest for the coolest stars in our sample, leading to a larger spread in the Fe II abundance. For this reason, we show the spreads calculated by using all stars (σ_{obs}^{16}) and by excluding the three coolest ones (σ_{obs}^{13}). The last two columns, σ_0^{16} and σ_0^{13}, show the cluster's intrinsic spreads for all stars and without the three coolest stars, respectively, obtained by correcting for the measurement uncertainty as:

$$\sigma_0^2 = \sigma_{obs}^2 - \varepsilon_{rand}^2. \tag{2.2}$$

Figure 2.4 shows the interquartile ranges (IQR) and the median values of the abundances we derived. The only siginificant intrinsic spreads were found for the light elements O, Na, Al, and the s-process element Ba. We also note the presence of one K-deficient star, which, however, does not present any anomalous O, Mg, Na, or Al abundances. The scatters of all other elements are compatible with the observational errors.

A table containing all chemical element abundance ratios with associated random errors for all individual stars is available online. A part of it is presented in Table 2.5 to guide the eye. The column labeled N shows the number of lines used to derive the particular element abundance and ε_{rand} shows the random error.

2.4.1 Iron

With this study we derived the first measurement of the Fe abundance of M 75 based on high-resolution spectroscopy as [Fe I/H] $= -1.16 \pm 0.03$ dex (random) ± 0.08 dex (systematic) with a marginal 1σ spread of 0.07 dex. Using Fe II lines, we obtained a higher value of [Fe II/H] $= -0.98 \pm 0.03$ dex (random) ± 0.16 dex (systematic) with a 1σ spread of 0.13 dex. There is no trend of the [Fe I/H] or [Fe II/H] values with temperature, except for the three coolest stars, which have

Table 2.5: Derived abundance ratios for the individual stars of the GC.[1]

Star ID	[FeI/H]	ε_{rand}	N	[FeII/H]	ε_{rand}	N	[O/H]	ε_{rand}	N	[Na/H]	ε_{rand}	N	[Mg/H]	ε_{rand}	N	...
239	−1.19	0.03	66	−1.17	0.06	6	−0.62	0.01	2	−1.20	0.08	3	−0.97	0.1	1	
251	−1.08	0.04	46	−0.76	0.05	5	−0.81	0.01	2	−0.87	0.11	3	−0.66	0.1	1	
442	−1.13	0.03	60	−0.94	0.08	4	−0.95	0.12	2	−0.62	0.10	3	−0.83	0.1	1	
461	−1.03	0.04	42	−0.66	0.06	3	−0.51	0.04	2	−1.22	0.04	3	−0.93	0.1	1	
483	−1.10	0.03	64	−1.02	0.09	5	−0.99	0.04	2	−0.41	0.06	3	−0.79	0.1	1	
486	−1.09	0.03	68	−1.02	0.06	5	−1.07	0.04	2	−0.70	0.02	3	−0.76	0.1	1	
503	−1.24	0.03	49	−0.86	0.04	6	−0.88	0.08	2	−0.95	0.05	3	−0.88	0.1	1	
512	−1.19	0.03	66	−1.04	0.02	5	−0.56	0.11	2	−1.23	0.11	3	−1.00	0.1	1	
583	−1.24	0.04	52	−1.11	0.06	4	−0.79	0.18	2	−1.20	0.06	3	−1.01	0.1	1	
612	−1.18	0.02	66	−0.90	0.03	5	−0.89	0.15	1	−0.90	0.06	3	−1.04	0.1	1	
655	−1.21	0.03	63	−1.08	0.05	7	−0.76	0.02	2	−0.89	0.08	3	−0.88	0.1	1	
876	−1.13	0.03	63	−1.01	0.03	5	−0.62	0.08	2	−0.91	0.09	3	−0.90	0.1	1	
901	−1.11	0.03	57	−0.96	0.04	5	−1.01	0.04	2	−0.49	0.10	3	−0.87	0.1	1	
1251	−1.23	0.04	54	−1.04	0.09	4	−1.02	0.1	1	−0.61	0.06	3	−0.73	0.1	1	
1312	−1.31	0.04	51	−1.14	0.07	6	−0.70	0.06	2	−0.95	0.07	3	−1.05	0.1	1	
1459	−1.17	0.03	61	−1.02	0.04	7	−1.02	0.1	1	−0.62	0.13	3	−1.04	0.1	1	

Notes. [1] The full table is available in electronic form at the CDS via `http://cdsarc.u-strasbg.fr/viz-bin/qcat?J/A+A/554/A81`.
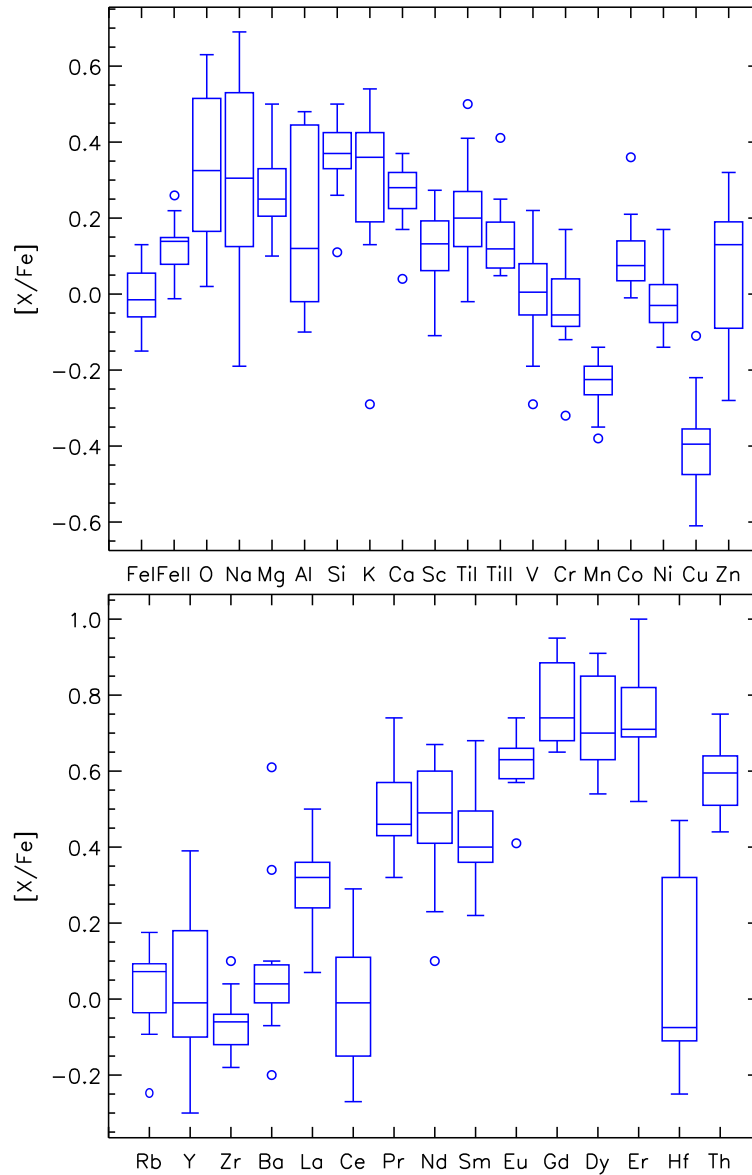
Figure 2.4: Boxplot of the derived abundances in M 75 relative to iron. Fe I and Fe II abundances are relative to the Fe I cluster mean. Neutral species are relative to Fe I and ionised species are relative to Fe II. The boxes designate the median values and IQR. The error bars show the minimum and the maximum value. Outliers are shown with circles. An outlier is defined if it deviates by more than 1.5 times the IQR.

Table 2.6: Average abundance ratios, average random and systematic errors, observational, and intrinsic spreads. See text for details.

Element	[X/Fe]	ε_{rand}	ε_{sys}	σ_{obs}^{16}	σ_{obs}^{13}	σ_0^{16}	σ_0^{13}
Fe I/H	-1.16	0.03	0.08	0.07	0.06	0.06	0.05
Fe II/H	-1.03	0.05	0.16	0.13	0.07	0.12	0.04
O I	0.34	0.08	0.10	0.20	0.21	0.18	0.19
Na I	0.30	0.08	0.06	0.25	0.24	0.24	0.22
Mg I	0.27	0.11	0.05	0.10	0.09	0.00	0.00
Al I	0.19	0.08	0.05	0.22	0.22	0.20	0.20
Si I	0.37	0.07	0.07	0.09	0.09	0.06	0.04
K I	0.30	0.09	0.13	0.20	0.11	0.18	0.06
Ca I	0.26	0.06	0.09	0.08	0.05	0.05	0.00
Sc II	0.08	0.12	0.09	0.13	0.10	0.05	0.00
Ti I	0.21	0.07	0.13	0.13	0.14	0.11	0.12
Ti II	0.09	0.10	0.09	0.15	0.10	0.11	0.00
V I	0.00	0.05	0.12	0.12	0.10	0.11	0.09
Cr I	-0.03	0.11	0.12	0.11	0.09	0.00	0.00
Mn I	-0.24	0.06	0.09	0.06	0.05	0.00	0.00
Co I	0.10	0.06	0.08	0.09	0.09	0.07	0.07
Ni I	-0.02	0.06	0.07	0.08	0.08	0.05	0.05
Cu I	-0.39	0.13	0.10	0.11	0.10	0.00	0.00
Zn I	0.05	0.15	0.08	0.17	0.16	0.08	0.06
Rb I	0.02	0.15	0.09	0.15	0.07	0.00	0.00
Y II	0.03	0.21	0.10	0.21	0.19	0.00	0.00
Zr II	-0.06	0.16	0.08	0.15	0.07	0.00	0.00
Ba II	0.08	0.07	0.13	0.22	0.19	0.21	0.18
La II	0.31	0.12	0.09	0.18	0.11	0.13	0.00
Ce II	0.00	0.16	0.08	0.22	0.18	0.15	0.08
Pr II	0.50	0.16	0.09	0.15	0.12	0.00	0.00
Nd II	0.46	0.16	0.09	0.18	0.17	0.08	0.06
Sm II	0.42	0.09	0.09	0.12	0.11	0.08	0.08
Eu II	0.62	0.07	0.09	0.14	0.08	0.12	0.04
Gd II	0.78	0.21	0.10	0.11	0.11	0.00	0.00
Dy II	0.74	0.21	0.10	0.17	0.12	0.00	0.00
Er II	0.74	0.21	0.10	0.20	0.12	0.00	0.00
Hf II	0.06	0.21	0.10	0.27	0.26	0.17	0.15
Th II	0.59	0.21	0.10	0.19	0.09	0.00	0.00

considerably higher [Fe II/H]. Excluding these three coolest stars, the mean discrepancy between the Fe I and Fe II values becomes [Fe I/Fe II] $= -0.14 \pm 0.02$ dex, which is still significant but the larger scatter of Fe II abundances is reduced to the same value as the Fe I scatter ($\sigma = 0.07$ dex).

Both values are in an excellent agreement with the metallicity derived by Catelan et al. (2002), based on UBV photometry of [Fe/H] $= -1.03 \pm 0.17$ dex and [Fe/H] $= -1.24 \pm 0.21$ dex on the metallicity scales of Carretta & Gratton (1997) and Zinn & West (1984), respectively.

The scatter of 0.07 dex may seem large compared to the bulk of GCs ($\sigma \lesssim 0.05$ dex; Carretta et al. 2009a) but it is fully consistent with the higher luminosity of M 75. With an absolute magnitude of $M_V = -8.57$ mag (Harris 1996), it is amongst the most luminous and hence most massive GCs in the Milky Way (only 18 of the ~ 150 MW GCs are brighter). Carretta et al. (2009a) reported a dependence on the scatter in [Fe/H] with various cluster parameters. In their homogenous sample of 19 GCs they showed that the 1σ dispersion correlates with the cluster luminosity (a proxy for the present mass), the maximum effective temperature reached on the HB, and anticorrelates with the level of α-enrichment. All these correlations point to a better capability of more massive clusters to self-enrich with the ejecta of massive stars. The deeper gravitational potential helps retaining the

massive stars ejecta and the hotter HB stars indicate larger He-content. Our sample of 16 stars, however, does not allow us to make any firm conclusions on the link between the observed Fe-scatter in M 75 and its self-enrichment.

2.4.2   Alpha elements

The production of α-elements such as O, Ne, Mg, Si, S, Ca, and Ti is mainly associated with the eruptions of SNe II. The different timescales of the occurrence of SNe II and SN Ia make the $[\alpha/\text{Fe}]$ abundance ratios a powerful tool for diagnosing the chemical evolution and star formation history (SFH) of any stellar population (Tinsley 1979). In the Milky Way, the relatively metal-poor halo stars form a plateau of enhanced $[\alpha/\text{Fe}] \sim +0.4$ dex, which starts to decrease when $[\text{Fe/H}] \gtrsim -1.0$ dex due to the onset of SNe Ia. A high $[\alpha/\text{Fe}]$ ratio is associated with rapid star formation episodes that ceased before the long-lived SNe Ia, the main source of iron, began to enrich the local environment through their ejecta. Dwarf galaxies, on the other hand, have slower star formation rates so that low values of $[\alpha/\text{Fe}]$ are observed already at low metallicities (e.g., Shetrone et al. 2001, 2003; Tolstoy et al. 2009). Although different α-elements are produced on similar timescales, they show element-to-element variations due to different production mechanisms, either through hydrostatic He-burning in the cores of massive stars (e.g., O and Mg), or during the SNe explosions themselves (e.g., Si, Ca, and Ti).

In M 75, we derived O-abundances by measuring the EWs and by spectral synthesis of the 6300 Å and 6364 Å lines, which are free of telluric contamination owing to the fortunate radial velocity of this GC. The 6364 Å line is, however, situated in the wing of a broad Ca autoionisation feature, so in the synthesis of this line we adopted the derived Ca-abundance. Additionally, we adopted Solar C- and N-abundances but we confirmed the results from Koch et al. (2009) that demonstrated that molecular (CNO) equilibrium does not affect the derived O-abundances at these metallicities and levels of O-enhancements. We also confirmed that there are not any extreme variations in the strength of the CH G-band around 4320 Å.

Mg-abundances were derived from the line at 5711 Å, Si from the 5684 Å, 5949 Å, and 6155 Å lines, Ca-abundances were based on 11 features between 5250 Å and 6750 Å, and Ti was measured from various Ti I and Ti II absorption lines. We found that all α-elements are enhanced with respect to the Sun to a different extent. The average $[\alpha/\text{Fe}]$ ratio is 0.3 ± 0.02 dex, based on the Mg, Si, and Ca abundances. This is consistent with the canonical value for the old stellar population of the Milky Way (halo field stars and the majority of its GCs; Pritzl et al. 2005). Oxygen is the only α-element, which shows significant variations in its abundance amongst the stars in our sample. These variations are discussed in the following section in terms of multiple populations.

2.4.3   Proton-capture elements

Elements like Na, Al, and K are produced through proton-capture reactions at high temperatures during the H-burning in the cores of massive stars. The above are the elements responsible for creating the unique chemical pattern of GCs (e.g. Denisenkov & Denisenkova 1989; Langer et al. 1993), also see the review from Gratton et al. (2004). Large variations in the abundances of Na and Al have been so far detected in all GCs studied to date (Gratton et al. 2012a). Nowadays, it is largely accepted that these variations are due to the presence of at least two stellar populations in every GC characterised by slightly different ages and abundance patterns. Whilst both populations show the same content of Fe-peak elements, the later formed stars are characterised by enhanced N, Na, and Al, along with depleted C, O, and possibly Mg. M 75 is not an exception in this respect. We measured Na-abundances from the three lines at 5682.6, 6154.2, and 6160.8 Å and Al-abundances from the four lines at 6696, 6699, 7835, and 7836 Å. Potassium abundances were derived mainly
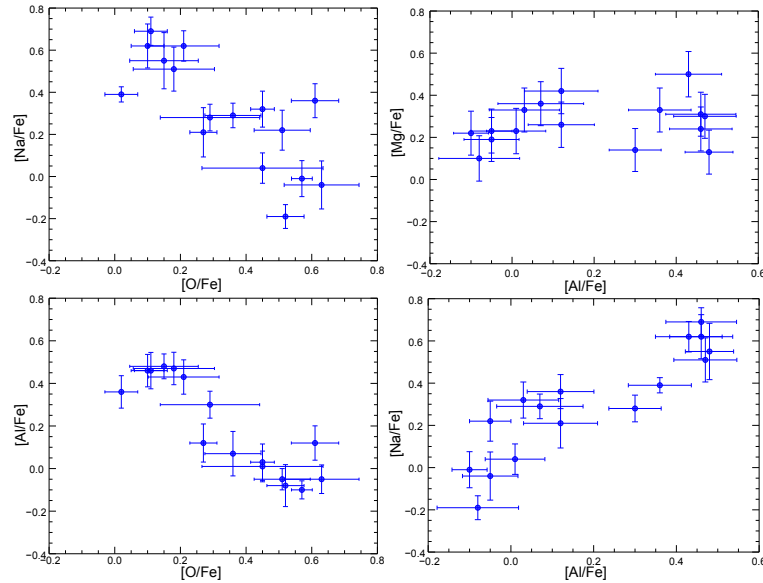
Figure 2.5: Correlations between the light elements; upper left: Na-O anticorrelation; upper right: (no) Al-Mg anticorrelation; bottom left: O-Al anticorrelation; bottom right: Al-Na correlation.

from the 7699 Å line, which was free of telluric absorption, however, saturated in the majority of our stars. We also used the weaker 7665 Å K line for reference, which was, however, strongly blended with telluric features. Lind et al. (2011) raised attention to possible large NLTE effects in the derived Na abundances from some commonly used lines. According to this study, however, in the regime of our stars (bright cool giants) the NLTE corrections are expected to be small (in the order $0.05 - 0.1$ dex for the lines that we used) and we ignored them.

Figure 2.5 shows different correlations between the light elements. The O-Na anticorrelation is clearly visible. We divided our sample into Primordial (P) population, characterised with O-rich and Na-poor stars, and Intermediate (I) population, characterised by O-poor and Na-rich stars, following the empirical separation introduced by Carretta et al. (2009c). The four stars with [Na/Fe] < 0.1 dex can be considered the remainder of the primordial population. The number ratio of P- to I-population stars is roughly $1/3$ based on the 16 stars in our sample, which is typical of most GCs but still rather low considering the cluster's high luminosity and the relatively large distance of our targets from the cluster's centre (median distance of 2.6 half-light radii). Carretta et al. (2009c) reported a correlation between the ratio of P- to I-stars with the cluster's luminosity and with the median distance of the stars from the cluster's centre in agreement with the GC formation models by D'Ercole et al. (2008), according to which, enriched by AGB stellar winds, gas is accumulated in the central regions of the cluster, where a kinematically cold second generation forms. Thus, in present-day GCs, the I-population is generally more concentrated in the central regions of a GC. Additionally, more massive clusters are better capable of retaining their stars, including the P-population. In this respect, we would expect to observe a P- to I-stars ratio of about 0.6 in M 75 or in a sample of 16 outer stars – 6 P-population and 10 I-population instead of the observed 4 P-population and 12 I-population stars. However, the lower ratio of P- to I-stars in our sample could well be due to a low number statistics. It is also worth pointing out that there is a clear gap in the Na-O and Al-O anticorrelations, which might indicate the presence of more than two populations of stars in M 75 (Figure 2.5). Assuming that the gap is real and not only owing to the small number statistics, we give a possible interpretation in the Discussion section.

M 75 has a negligible spread in Mg with respect to the observational errors and we do not see a correlation between Mg and Al, as found in other massive GCs (Gratton et al. 2001; Carretta et al.

2009b). This can be explained with the abscence of an Extreme (E) population in M 75, characterised by extremely low O, high Na, and lower Mg abundances. Although, a rough calculation shows that the Al enhancement of +0.6 dex could be obtained by reducing the Mg abundance by only 0.06 dex, thus there is no need to be a strong slope in the [Mg/Fe] vs. [Al/Fe] diagram. The large Al variation is, however, strongly correlated with Na and anticorrelated with O (Figure 2.5). Neither of these elements shows a trend with effective temperature and we can consider these correlations genuine properties of the cluster. Potassium is not correlated with any of those elements and its marginal variations could be due to significant temperature-dependent NLTE effects in the strong 7699 Å line (Zhang et al. 2006). Thus, the [K/Fe] ratios show a slight trend of decreasing abundance with decreasing temperature.

2.4.4   Iron-peak elements

All the odd-Z iron-peak elements V, Mn, Co, and Cu suffer from significant HFS corrections. These corrections vary from 0.2 to 0.6 dex for the different elements, with the largest effects for Cu. As a result, Mn and Cu are depleted with respect to iron by 0.24 ± 0.06 dex and 0.39 ± 0.13 dex, respectively. Such values are not unusual and are observed in a number of stellar systems (Cayrel et al. 2004; McWilliam et al. 2003; McWilliam & Smecker-Hane 2005) and a number of Galactic GCs (e.g. Koch et al. 2009; Koch & Côté 2010). Cobalt is slightly overabundant with respect to iron with a value of [Co/Fe] $= 0.10 \pm 0.06$ dex. All even-Z elements (Cr, Ni, Zn) plus Sc and V trace the dominant iron production in the long-lived SNe Ia in that the [X/Fe] ratios are compatible with the solar values ([X/Fe] ~ 0.0 dex).

2.4.5   Neutron-capture elements

We derived chemical element abundance ratios for a large variety of n-capture elements mainly based on EW measurements, but we employed spectral synthesis for those elements, for which only few weak or highly blended lines were available. We used the Kurucz atomic database to obtain a blending list for our synthesis. The lighter n-capture elements Rb, Y, and Zr, usually associated with the weak s-process, have [X/Fe] ratios close to the Solar values (Table 2.6). We note, however, that the associated random errors on these ratios are large, owing to difficulties in measuring them. For instance, Rb and Zr abundances are derived through a spectral synthesis of the 7800 Å and 5112 Å lines, respectively, which accounts for the severe blending of these lines. Yttrium abundances are derived based on EWs of three lines found in the blue region of the red arm of MIKE, which is generally characterised by a lower S/N ratio. We also did not account for HFS effects associated with this odd-Z element due to lack of HFS data, but the corrections are expected to be small (Prochaska et al. 2000).

Barium is the only n-capture element, which presents intrinsic variations significantly exceeding the random errors. In particular, there are two Ba-rich stars with [Ba/Fe]$= +0.34 \pm 0.10$ dex and [Ba/Fe]$= +0.61 \pm 0.06$ dex, while the mean [Ba/Fe] ratio is 0.01 ± 0.02 dex (Figure 2.8). Both stars are certainly not luminous and cool enough to have produced the s-process themselves and the high Ba abundances are most likely due to enrichment from AGB stars in the cluster's environment. The significance of these Ba-rich stars is further discussed in the Discussion section. Our Ba abundances were derived mostly based on EWs of the easily accessible 5854 Å line, while the 6142 Å and 6497 Å lines are saturated in most of our stars. For the warmer stars with higher gravity, where the latter lines are not saturated (reduced EW < -4.5 dex), the derived abundances perfectly agree with the results from the 5854 Å line alone.

Lanthanum, Ce, Pr, Nd, Sm, and Eu abundances were derived based on the EWs of one or two sufficiently strong lines, while the abundances for Gd, Dy, Er, Hf, and Th are derived based on

spectral synthesis of one or several lines of these species. We note that the associated errors of the latter elements are large owing to the weakness of the lines and/or the low S/N ratios in their vicinity. One might also be interested if the Ba-enhanced stars also show variations in the other s-process elements La and Ce. These two stars show a marginal enhancement in their La abundance by $\sim 2\sigma$ above the cluster's average [La/Fe] ratio and statistically insignificant Ce-enhancement by less than 1σ above the cluster's average [Ce/Fe] ratio. We applied HFS corrections to the odd-Z elements La and Eu but there were no available HFS data for Pr. We assumed that they are comparable in magnitude to the HFS corrections for the other n-capture elements and thus very small.

Besides Ba, Ce, and Hf, which show solar [X/Fe] ratios, all other heavy elements are enhanced with respect to the Sun; see Section 2.5.1 for discussion.

2.5 Discussion

2.5.1 r- and s-process enrichment in M 75

It is surprising that, at [Fe/H] $= -1.16$ dex, M 75 seems to be one of the rarer cases of GCs compatible with predominant r-process production of the n-capture elements (Figure 2.6, see also Sneden et al. 2000; Yong et al. 2008; Koch et al. 2009, for M 15, M 5, and the distant GC Pal 3, respectively). In Figure 2.6 we show the total r+s-process Solar curve and the pure r-process curve from Burris et al. (2000) plotted over the mean n-capture element abundances derived from our spectroscopic sample of M 75. Both curves are normalised to the mean Ba-abundance for an easier distinction. A χ^2 test shows that the best fit to the production of the elements from Ba (Z= 56) to Th (Z= 90) is found for a scaled Solar pure r-process enrichment plus an admixture of 10% of the Solar s-process yields (Figure. 2.7; upper panel). In this fit we included all stars in our sample but the two Ba-enhanced ones and we excluded the elements Rb, Y, Zr, and Hf. Hafnium lies off the general pattern in all stars and we assumed that its abundances likely suffer from a severe systematic offset. The lighter n-capture elements Rb, Y, and Zr, on the other hand, have very complicated production channels, which are not yet fully understood (Travaglio et al. 2004). For instance they are associated with the weak s- and r-processes, which appear in massive (M $\sim 20M_\odot$) stars on similar timescales as the r-process production from SNe II (Raiteri et al. 1993). We conclude that only a small number of AGB stars have contributed to the enrichment of the primordial cloud from which M 75 formed.

We note that there is not any difference in the n-capture element abundance pattern between the P- and I-populations in our sample with the exception of the two Ba-enhanced stars. Only the most massive ($\sim 5-8\,M_\odot$) AGB stars reach the necessary high ($> 8 \times 10^7$ K) temperatures at the bottom of the convective envelope to activate the ON cycle and thus to reduce the O abundance. These AGB stars experience only a few dredge-up processes, which cannot alter the s-process abundances (D'Ercole et al. 2008). It is however, possible that there exist a narrow mass limit around $4\,M_\odot$, where both p-capture and s-process elements can be simultaneously modified. The detection of two Ba-rich stars in M 75 in fact favours the AGB stars as principle polluters in M 75. We found the best χ^2-fit for both Ba-rich stars to be scaled solar r- plus an admixture of 50% and 100% of the scaled Solar s-process yields, respectively. The abundance pattern of the Ba-rich star #901 together with its best fitting model is presented in Figure 2.7, bottom panel. Since Ba-abundances are very sensitive to the stellar parameters, in particular to the microturbulence velocity, we tested whether we would get similar s-process enhancements for our stars if we exclude the Ba-abundance. We performed again the same χ^2 tests to the abundances of all Ba-normal stars, averaged together and the two Ba-rich stars - separately. The results show that the Ba-normal stars have again experienced only 10% of the solar s-process and the two Ba-rich ones 40% and 70%, respectively.
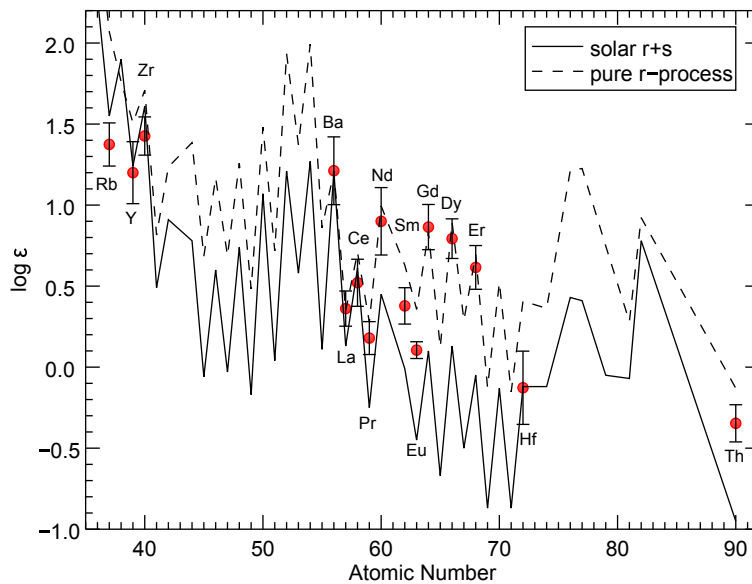
Figure 2.6: Mean neutron capture element abundances for all stars in M 75, normalized to Ba. The lines display the scaled solar pure r- and r+s-process contributions from Burris et al. (2000). The uncertainties represent the 1σ scatter of the derived element abundances in all stars.

2.5.2   Th-Eu age

Despite the large formal errors of the measured Th abundance, the star-to-star variations of Th are small, which leads to a precise, mean Th abundance for the cluster. We used the [Th/Eu] ratio to derive an approximate age estimate for M 75 based on the radioactive decay of Th. The mean $\log\varepsilon(\mathrm{Th/Eu})$ is -0.55 ± 0.02 dex, or $N_{\mathrm{Th}}/N_{\mathrm{Eu}} = 0.28$. Whilst Eu is a stable element, the half life period ($t_{1/2}$) of the isotope ^{232}Th is 1.41×10^{10} yr. Using the universal law of radioactive decay, namely $N(t) = N_0 e^{-\lambda t}$, where $\lambda = \ln(2)/t_{1/2}$, and the Solar System initial Th/Eu ratio, $N_{\mathrm{Th}}/N_{\mathrm{Eu}} = 0.46$, (Cowan et al. 1999), we obtained an age estimate of 10 Gyr. This method usually leads to a precision of ± 3 Gyr but the estimate we reached for M 75 is in perfect agreement with isochrone ages for this object (e.g. Catelan et al. 2002) and confirms that it is younger than the bulk of MW GCs. For comparison, Sneden et al. (2000) have published $N_{\mathrm{Th}}/N_{\mathrm{Eu}} = 0.25$ for M 15, which leads to an age of 12.4 Gyr, if using the same atomic parameters. Note that very small systematic errors in the Th abundance can still lead to large errors in the age estimate. For instance, a systematic error of 0.1 dex in Th leads to 5 Gyr difference in age. More accurate spectroscopic age-dating would be feasible once U-abundances can be measured (Frebel et al. 2007), but given the low S/N ratios in the relevant blue regions, this is an unlikely endeavour in the remote M 75.

2.5.3   Multiple populations in the CMD of M 75

The phenomenon of multiple populations in GCs often extends to the appearance of the CMD. High-precision photometry has revealed multiple main sequences, subgiant branches, and RGBs in the CMDs of many clusters, which do not exhibit large variations in metallicity (Piotto et al. 2007, 2012; Han et al. 2009). These effects are mostly driven by CNO variations and different He-content in stars from different generations (D'Antona et al. 2002, 2005; Piotto et al. 2005). Moreover, the presence of multiple populations has been proven to be one of the key parameters that shapes the HB, where the effect is most pronounced, because stars of the same age but different He-content have different initial masses and, thus, occupy different regions of the HB. Whilst the stars with primordial He-abundance (compatible with the Big Bang nucleosynthesis) preferably populate the
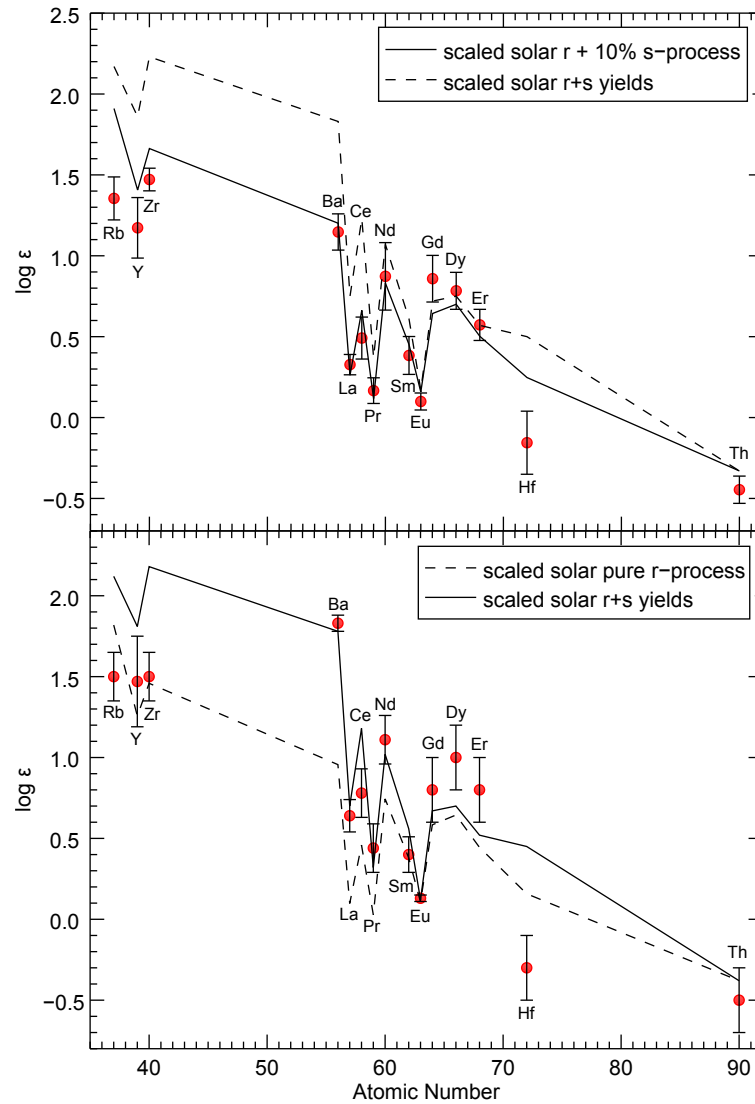
Figure 2.7: Upper panel: Mean neutron-capture element abundance pattern for all "Ba-normal" (s-process deficient) stars in M 75. The solid line represents the best fit model for a scaled solar r-process plus 10% of the scaled solar s-process yields. The dashed line shows the scaled solar total r+s-process yields for comparison. The error bars represent the 1σ scatter of the derived element abundances of all s-process deficient stars; Bottom panel: Derived n-capture elements abundances for star #901 - the most s-process rich star in our sample. The solid line represents the best fit model for a scaled solar total r+s-process yields. The dashed line shows the scaled solar pure r-process model for comparison. The error bars represent the random errors for this particular star.

red part of the HB, stars with enhanced He are responsible for the formation of extended blue tails (D'Antona et al. 2002; D'Antona & Caloi 2004). Strong correlations between the He-content and the abundances of p-capture elements with the effective temperature amongst stars from the HB have been recently found in M 4 (Marino et al. 2011), NGC 2808 (Gratton et al. 2011), and NGC 1851 (Gratton et al. 2012b). M 75 is one of the most curious cases in this respect. It has a very extended and peculiar HB with a trimodal distribution (Catelan et al. 2002). Apart from the well separated BHB and RHB, its CMD shows a distinct third extension of a very blue, faint tail (Figure 2.1, see also Figure 2 in Catelan et al. 2002). The extended blue tail of M 75's HB is at odds with our findings of only a moderate Na-O anticorrelation on the RGB (Figure 2.5), which so far lacks an extreme (E) population. Such a population is often found in GCs with extended HBs (Carretta et al. 2009c) and characterised by extremely Na-rich and O-poor stars, and accompanied by large He variations. Having in mind, however, the tiny populated extremely blue tail in M 75 and the limited number of our sample, it is possible that such E population has just been missed by our selection criteria. But curiously, we do not detect a Mg-Al anticorrelation, neither, which is commonly found in those GCs with a more complex HB morphology. Furthermore, clues for He-, CNO-, or age-variations have not been detected in the CMD of M 75 (in terms of multiple RGBs, subgiant branches, or main sequences). We note however, that there is not any narrow-band photometry available for this GC, which might reveal multiple populations amongst the main sequence, the subgiant branch and the RGB (e.g. Carretta et al. 2011a). Still, the distribution of He and p-capture elements amongst the HB of M 75 remains an open question and thus, high-resolution spectroscopic observations amongst stars on the HBs are needed to ascertain if its peculiar morphology is mostly driven by the presence of multiple populations or if there are other parameters with major influence. Possibly, the younger age and higher concentration, complemented with its remote location in the Milky Way halo hold important clues about its origin.

2.5.4   Four distinct chemical populations in M 75

A closer look to the Na-O and Al-O anticorrelations of M 75 (Figure 2.5) shows three distinct populations rather than a continuous anticorrelation, as found in most GCs (the P-population, which consists of stars with Na- and O-abundances typical of the halo field; a second group of stars mildly enriched in Na and depleted in O; and a third group of the most Na-rich, O-depleted stars, which is separated by a clear gap from the second group). But the question whether the Na-O anticorrelation in GCs is actually continuous or rather discrete has recently raised attention because the findings of discrete main sequences in some GCs (D'Antona et al. 2005; Piotto et al. 2007) and the discrete distribution of the Na and O abundances amongst the HB (Marino et al. 2011) suggest a discrete chemical distribution of the different populations also amongst the RGB. Currently, more precise, high-resolution studies of large number of GCs' RGB stars are being carried out to clear out this question (e.g. Carretta et al. 2012). Besides the three populations seen in the Na-O plane, M 75 also hosts a number of Ba-rich stars, which could represent a fourth population.

A possible explanation of the formation of four populations could be found within the pristine gas dilution scenario suggested by D'Ercole et al. (2008, 2011). On a timescale of several tens of Myr after the a first generation of stars has formed, the centre of the cluster still hosts only gas from the higher mass AGB stars' ejecta. At this point, the Na-rich, O-depleted, Ba-normal population is formed. In the next ~ 10 Myr, pristine gas falls in the central region of the cluster and mixes with the gas enriched by the AGB winds. Another population forms from the diluted gas, which is mildly Na-rich and O-depleted. After the diluted gas is fully processed, the lower mass AGB stars remain the only source of gas in the cluster. Their ejecta could also be enhanced in s-process elements. The last Ba-rich population forms, which is also strongly Na-rich and O-depleted and indistinct from the other stars formed from none-diluted gas (Figure 2.8). Hydrodynamical and N-
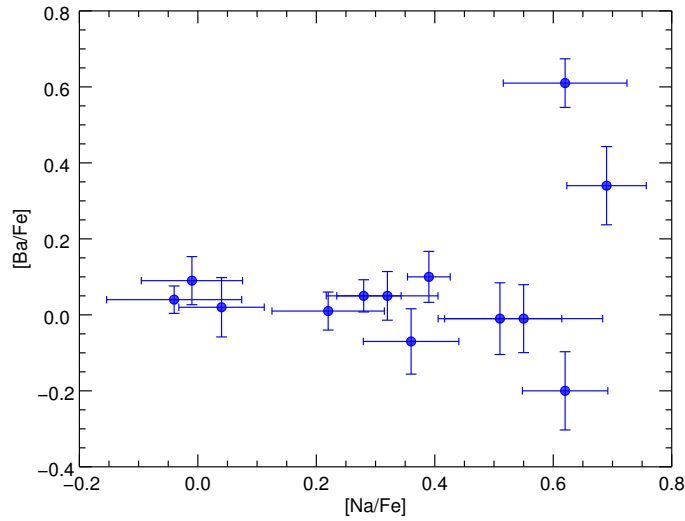
Figure 2.8: [Ba/Fe] vs. [Na/Fe] ratios in M 75's RGB stars. The two most Na-rich stars are also Ba-enhanced by 0.34 ± 0.10 dex and 0.61 ± 0.06 dex, respectively.

body simulations can test the viability of this idea and better constraint the time-scales and polluters' masses. Meanwhile, some improvements of the AGB models are also needed, since we do not yet fully understand these very late evolutionary stages in terms of mass-loss, convection, and nuclear reaction cross-sections.

2.5.5 Constraints on the mass of the polluters in M 75

Now we can place some qualitative constraints on the average mass of the polluters in M 75 provided that enrichment was dominantly from AGB stars. Despite its high luminosity, which is often considered as a reason for the presence of higher mass polluters, there are several factors prompting that *lower* mass AGB stars also contributed to the formation of the intermediate population in this GC:

i) Whilst the maximum amount of Na produced in most GCs is approximately the same, high mass AGB stars manage to process more O through the ON cycle and, hence, they are more depleted in this element. Therefore, the amount of O-depletion is a proxy for the polluters' average mass in the sense that more extended Na-O anticorrelations imply higher mass polluters (see Carretta et al. 2009c). For instance, the Na-O anticorrelation in M 75 is less extended than in other GCs of similar luminosity (e.g. NGC 1851, NGC 2808, M 5) and more similar to the less massive M 4, prompting for lower mass polluters in M 75. Another example of a massive GC that does not have an extended Na-O anticorrelation is 47 Tuc ($M_V = -9.42$ mag). This GC, however hosts significantly more O-depleted stars compared to M 75 and suggests predominantly high-mass AGB polluters, in accordance with the conclusions drawn by Carretta et al. (2012). This is best represented in Figure 2.9, where we plot the Na-O anticorrelations of M 75 and the three reference clusters – NGC 1851, M 4, and 47 Tuc. We also show simple dilution models that we computed as described in Carretta et al. (2009c), tuning by eye the input parameters (the maximum and minimum Na- and O-abundance ratios) for all of them. Figure 2.9 clearly shows that the Na-O anticorrelation of M 75 is more similar to the less massive GC M 4 compared to the extended anticorrelation of NGC 1851 and "steeper" than the Na-O anticorrelation of 47 Tuc. Thus, we suggest that the average mass of
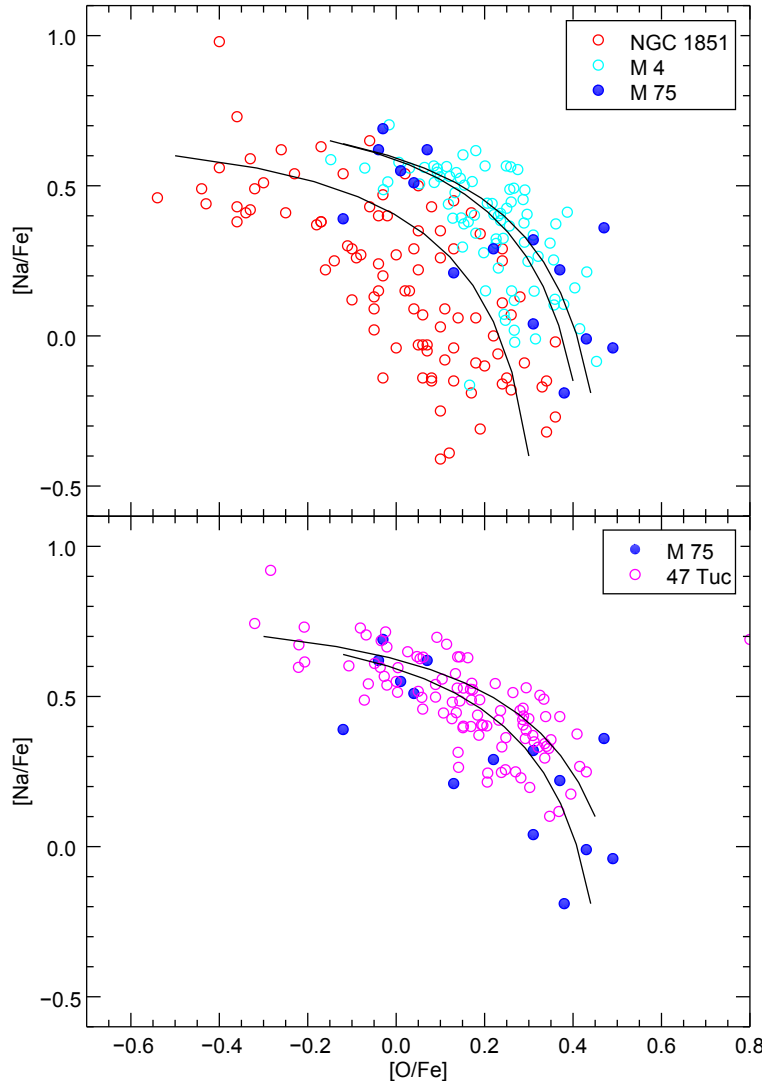
Figure 2.9: A comparison of the extent of the Na-O anticorrelations of several GCs relative to M 75; Top panel: the Na-O anticorrelations in M 75, NGC 1851 (Carretta et al. 2011b), and M 4 (Carretta et al. 2009c); Bottom panel: the Na-O anticorrelations in M 75 and 47 Tuc (Carretta et al. 2009c). Simple dilution models are overimposed. The [O/Fe] abundances of M 75 are shifted by the mean discrepancy of [Fe I/Fe II]$= -0.14$ dex to match the other studies.

the polluters differs from cluster to cluster, regardless of its luminosity. M 75 and M 4 were likely enriched by the ejecta of lower mass AGB stars, while 47 Tuc was mainly enriched by more massive AGB stars. GCs with very extended Na-O anticorrelations (e.g. M 5, M22, NGC 2808, NGC 1851) most likely experienced continuous star formation (~ 100 Myr) and were enriched by polluters of broader mass range.

ii) Furthermore, the two stars, which present anomalously high Ba abundances are also the most Na-rich ones (Figure 2.8). This is indicative of s-process enrichment from intermediate-mass AGB stars ($M < 4 - 5M_\odot$), that are able to alter the s-process pattern of the I-population stars (Gallino et al. 1998). Ba-rich stars are very rare in GCs but have also been found in NGC 1851, M 22, and ω Cen, which are all noted for their complex evolution, likely characterised by longer star formation period extending after these low mass stars manage to pollute the cluster environment with s-process enhanced ejecta.

iii) The [Rb/Zr] ratio can also be a proxy for the polluters' mass because it is sensitive to the neutron density. The main neutron source in the He shell of low mass ($1 < M < 4M_\odot$) AGB stars is the reaction $^{13}C(\alpha,n)^{16}O$, while in more massive AGB stars, neutrons are mainly released by $^{22}Ne(\alpha,n)^{25}Mg$ and since the ^{22}Ne source produces much higher neutron densities than the ^{13}C neutron source, the [Rb/Zr] ratio can discriminate between the two (García-Hernández et al. 2009). The mean [Rb/Zr] ratio of M 75 is $= -0.04 \pm 0.03$ dex and there are not any significant star-to-star variations in our sample of stars. Both Ba-rich stars have a [Rb/Zr] $= 0.06 \pm 0.2$ dex, which is a statistically insignificant difference with respect to the mean [Rb/Zr] ratio. We conclude that we cannot use the [Rb/Zr] ratio to discriminate between different AGB masses, owing to the large uncertainties of this ratio in individual stars.

2.5.6 Comparison with other GCs, Galactic halo field stars, and dwarf spheroidal galaxies

In order to investigate M 75's origin, we present in Figure 2.10 a comparison of the abundances in M 75 with the abundances of Galactic disk and halo stars at different metallicities, and with the average abundances of other GCs. A small representative sample of individual dSph stars is also plotted for comparison. The abundances of the Milky Way halo and disk stars are taken from the compilation of Venn et al. (2004, and references therein) and complemented with the recent results of Ishigaki et al. (2012a,b). The sample of dSph stars also comes from Venn et al. (2004) and includes the abundances of individual stars from Carina, Fornax, Leo, Scl, UMi, Sex, and Draco dSphs. The mean abundances of various GCs are taken from Pritzl et al. (2005) and complemented with the more recent results for NGC 1851 (Carretta et al. 2011b), M 5 (Yong et al. 2008), and the outermost halo clusters Pal 3 (Koch et al. 2009), and Pal 4 (Koch & Côté 2010).

We chose to plot in Figure 2.10 three key element ratios, important to trace the chemical evolution of M 75. The α-element abundance ratio in M 75 is fully compatible with the Galactic halo stars at the same metallicity and consistent with the α-enhanced old stellar populations of the Milky Way halo. This suggests that the primordial cloud from which the GC formed experienced the same (fast) enrichment, dominated by SNe II as most halo GCs. A connection with the current dSph galaxies and their low star formation rates (hence low [α/Fe]) can be ruled out. Some GCs with low α-abundance like Pal 12, Ruprecht 106, and possibly Ter 7 are associated with the Sgr dSph (Pritzl et al. 2005).

The [Ba/Y] ratio compares the abundance yields between the main s-process, which takes place in intermediate- to low-mass AGB stars and the weak s-process, which is associated with very massive ($M > 20\ M_\odot$) stars (Burris et al. 2000). The Galactic halo and disk stars have a roughly solar [Ba/Y] ratio over a broad range of metallicities, which starts to decrease at [Fe/H] $\lesssim -2$ dex. In dSphs, on the other hand, the [Ba/Y] ratio is rather high (Venn et al. 2004; Tolstoy et al. 2009), owing to their typically lower star formation rates. However, all GCs, including M 75, present typical of the halo field [Ba/Y] ratios around the solar value, with again, the notable exception of Pal 12, which has unusually high mean [Ba/Y] ratio, more similar to the stars from dSph galaxies.

Finally, the [Ba/Eu] ratio compares the yields from the main s- and main r- neutron capture processes. The latter operates mainly in massive stars during the eruptions of SNe II. Typically, all stars in the field and in GCs present abundances that are consistent with r-process enrichment plus some fraction of the solar s-process contribution from AGB stars. The s-process fraction varies for different stars but the general trend is that it could be entirely missing for metal-poor stars and rises until it becomes dominant for the metal rich population. As we noted above, M 75 has an unusually low, mean s-process contribution for its metallicity, but its [Ba/Eu]$= -0.55 \pm 0.05$ dex (-0.63 ± 0.01 dex if we consider only the P-generation) is still consistent with some halo stars. Only a few GCs, studied to date, have been noted to present [Ba/Eu] ratios compatible or
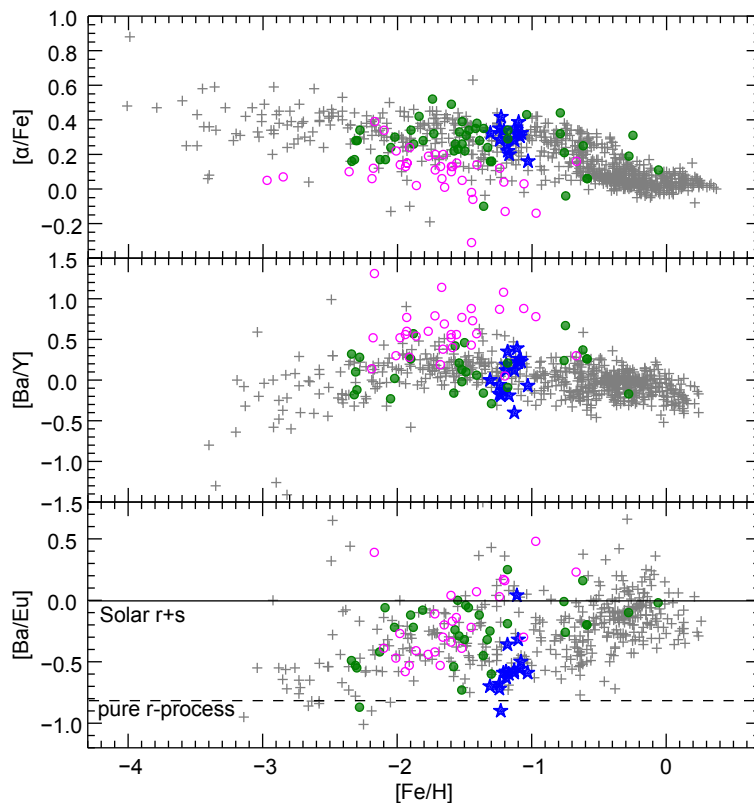
Figure 2.10: A comparison of the α and n-capture element abundances of the 16 stars of M 75 (blue asterisks) with Galactic disk and halo stars (grey crosses), average abundance values of other Galacatic GCs (filled green circles), and a representative sample of individual dSph stars (open magenta circles).

lower than M 75. The majority of them are amongst the most metal-poor GCs in our Galaxy with [Fe/H] below -2.3 dex, namely M 68, [Ba/Eu]$= -0.50$ (Lee et al. 2005), M 92, [Ba/Eu]$= -0.55$ (Shetrone et al. 2001), M 15, [Ba/Eu]$= -0.87$ (Sneden et al. 2000), and M 30, [Ba/Eu]$= -0.53$ (Shetrone et al. 2003). On the more metal-rich end, we note the GCs NGC 3201 with [Fe/H]$=$ -1.58 dex and [Ba/Eu]$= -0.54$ dex (Gonzalez & Wallerstein 1998), Pal 3 with [Fe/H]$=-1.52$ dex and [Ba/Eu]$= -0.73$ dex (Koch et al. 2009), and M 5 with [Fe/H]$= -1.30$ dex (most similar to M 75) and [Ba/Eu]$= -0.60$ dex (Ramírez & Cohen 2003; Yong et al. 2008).

NGC 1851 is probably the GC that shares most common properties with M 75 and is often thought as its twin (Catelan et al. 2002). Here, we investigate the similarities and differences between the two objects in deeper detail. Both GCs are coeval, share the same metallicity, and show similar HB morphology. Both are luminous, massive and very concentrated clusters located in the transition region between the inner and outer Milky Way halo. A notable difference between the two objects is the presence of double subgiant and red giant branches in NGC 1851 (see Milone et al. 2008; Han et al. 2009), which are not observed in M 75, despite the same photometric quality. Ventura et al. (2009) have suggested that large CNO variations and a small age spread could explain the subgiant branch in NGC 1851. This scenario is supported by Yong et al. (2009) from observations of 4 RGB stars. However, it has been dismissed by more recent studies by Villanova et al. (2010) of 15 RGB stars and by Gratton et al. (2012b), who derived abundances for a large sample of HB stars. Both studies found no evidence for significant CNO variations. Gratton et al. (2012b) concluded that the only explanation of the splitting of the SGB and RGB of NGC 1851 is a considerable age difference of about 1.5 Gyr. Furthermore, Carretta et al. (2010) detected two independent Na-O anticorrelations on the two RGBs of NGC 1851, which led to the suggestion that

Table 2.7: Comparison with GCs that share some common properties with M 75

	M 75	NGC 1851	M 4	M 5	47 Tuc	Pal 3
R_{GC} (kpc)[1]	14.7	16.6	5.9	6.2	7.4	95.7
r_h (arcmin)[1]	0.46	0.51	4.33	1.77	3.17	0.65
$c = \log(r_t/r_c)$[1]	1.80	1.86	1.65	1.73	2.07	0.99
rel. age (Gyr)[2]	~ 10	9.8	12.7	10.8	13.7	?
M_V[1]	-8.57	-8.33	-7.19	-8.81	-9.42	-5.6
[Fe/H][1]	-1.16	-1.18	-1.16	-1.29	-0.72	-1.63
$[\alpha/Fe]$[3]	0.30	0.34	0.29	0.16	0.25	0.39
[Ba/Eu][3]	-0.63	-0.19	0.25	-0.60	0.16	-0.73
[Ba/Y][3]	0.04	0.21	-0.09	-0.29	0.37	-0.02

Notes. [1] Data taken from Harris (1996, 2010 version) [2] Relative ages from Marín-Franch et al. (2009). We adopted a reference age of 13 Gyr. [3] Various sources cited throughout the text.

this cluster could have formed from the merger of two GCs with different ages. In any case, the clearly more complex formation history of NGC 1851 is responsible for the very extended HB in this system. In the case of M 75, it is not yet clear what physical processes drive the formation of such an extended HB.

The most comprehensive chemical study of NGC 1851, in terms of derived abundances for many different elements, is presented in Carretta et al. (2011b). We used it to compare the chemical abundances in both clusters. They share the same metallicity (with similar marginal iron spreads in both of them) and similar α-enhancement. The p-capture elements Na and Al have similar variations in both clusters but O shows a larger spread in NGC 1851, leading to a more extended Na-O anticorrelation in the latter GC (See Figure 2.9). The iron-peak element abundances are identical in both GCs. The largest difference between the two lies in the n-capture elements. This is best illustrated in Figure 2.11, where we present the total s- to r-process ratio in both GCs. We chose the average abundance of Ba, La, and Ce as representatives of typical s-process elements, where about 80% of their production comes from the s-process, and the average abundance of Eu and Dy as representatives of elements produced mainly by the r-process (Burris et al. 2000). The stars of NGC 1851 clearly lie above those from M 75 in this parameter space, indicating different primordial s-process contribution. We note, however, that both M 75 and NGC 1851 host s-process rich stars, which were enhanced in s-process elements most probably by intermediate-mass AGB stars during the early evolution of these stellar systems via self-enrichment mechanisms, but the s-process rich stars in M 75 reach [s/r] ratios similar to the primordial s-process enhancement of NGC 1851.

Finally, we note that M 75 is both a unique and a normal GC of the Milky Way's GCs system. Unique, in the sense that there is not a GC, which resembles all the same properties of M 75, and normal in the sense that its properties fit well in the general picture of the Milky Way's GCs. So far there are not two clusters found to be exactly alike and each one of them deserves special attention. In Table 2.7 we present some important characteristics of M 75 compared to other GCs, which were discussed in this section and that share some important similarities and differences with M 75.
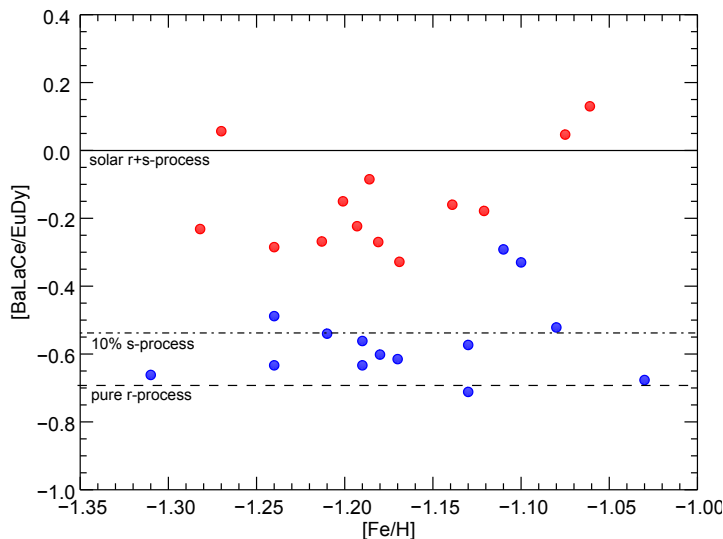
Figure 2.11: A comparison between the r- and s-process enrichment in M 75 (blue dots) and NGC 1851 (red dots). The figure clearly reveals the different enrichment history between the two GCs.

2.6 Summary

In this chapter, we presented the first chemical abundance study of the outer halo GC M 75. Our data sample consists of high resolution spectra of 16 giant stars, obtained with the MIKE spectrograph at the Magellan Observatory. We derived abundances through EW measurements and spectral synthesis in LTE for a total of 32 different elements covering a broad range of p-capture, α, iron-peak, and n-capture elements. M 75 is moderately metal rich cluster with [Fe/H]$= -1.16 \pm 0.02$ dex with a marginal spread of 0.07 dex, typical for GCs with similar luminosity. We measured an enhanced average α abundance [α/Fe]$= 0.30 \pm 0.02$ dex, based on Mg, Si, and Ca, typical for the Galactic halo at this metallicity. We found significant variations in the abundances of the p-capture elements O, Na, and Al, which provide evidence for the presence of at least two populations, formed on a short time-scale. Sodium is anticorrelated with O and correlated with Al, consistent with simple dilution models. The Na-O anticorrelation appears discrete, suggesting three chemically distinct populations. Additionally, the two most Na-rich stars form a fourth, Ba-enhanced population. Based on the extent of the Na-O anticorrelation, we conclude that the I-population stars were enriched by the ejecta of relatively less massive AGB stars in several episodes of star formation, which ended before the SNe Ia began to contribute iron to the cluster's environment. We note that the least massive polluters were able to alter the s-process abundances of the cluster's ISM.

The moderate O-Na anticorrelation (our sample of 16 stars lacks an extreme population of stars with very low O abundances) and the lack of significant Mg variation are at odd with the very extended trimodal HB of M 75. We conclude that the parameters that shape the peculiar HB morphology of this GC are still unclear and more observations are required, in particular a spectroscopic sample of stars, which represents the full span of the HB.

The n-capture element pattern is consistent with predominant r-process enrichment with a marginal contribution (about 10% of the scaled solar production) of s-process. This, coupled with its high metallicity and younger age, suggests that M 75 was born in an environment that was able to build metals very quickly and supports a scenario where the GC was accreted into the Milky Way halo on a later stage of the halo formation. The overall chemical and evolutionary status of M 75 is consistent with other halo GCs and field stars and is in line with a possible accretion origin of a large fraction of the Milky Way GCs.

3

Structural and kinematic properties the old, metal-poor globular cluster NGC 4372 [1]

3.1 Introduction

NGC 4372 is a relatively nearby ($R_\odot = 5.8$ kpc) and yet neglected GC in the inner halo. Photometric studies have established it as an archetypical old (> 12 Gyr) and metal-poor object, [Fe/H] $\simeq$ -2.1 dex (Alcaino et al. 1991; Geisler et al. 1995; Rutledge et al. 1997; Rosenberg et al. 2000; Piotto et al. 2002). It is of particular interest from a dynamical point of view, since it is known to harbour close stellar binaries and luminous X-ray sources (Servillat et al. 2008). Curiously, these are mainly found outside the central regions. This is in contrast to the expected segregation based on the larger dynamical mass of such binary systems and suggests that NGC 4372 has still not established a significant degree of kinetic energy equipartition or that other dynamical processes have stirred up the cluster and expelled these sources from the centre. In this context, we also note its short orbital period (0.1 Gyr) and moderate vertical space velocity component ($W = +100$ km s^{-1}), so that the resulting orbit (Casetti-Dinescu et al. 2007) implies many slow disk crossings. With a core relaxation time $\log t_c = 8.88$ dex (Harris 1996), NGC 4372 is an intermediately relaxed system, according to the classification of Zocchi et al. (2012). Considering its relatively low concentration and old age, it might be an example of a re-bounced, post-core-collapse GC (see Cohn & Hut 1984). The similarities of the orbit of NGC 4372 to the orbit of the massive GC NGC 2808 has suggested that both clusters are dynamically paired.

Internal rotation is one of the main reasons for the flattening of GCs, but external tides and pressure anisotropy can also play a significant role (van den Bergh 2008). In this work we build a dynamical, rotating model of the old, metal-poor, halo GC NGC 4372 using the Varri & Bertin (2012) family of models (see also Bianchini et al. 2013). From this, we derive and use the maximum rotation amplitude to central velocity dispersion ratio (A_{rot}/σ_0) to assess the importance of internal rotation in this GC. While it has been shown by means of N-body simulations that internal rotation

---

and tidal interactions significantly accelerate the dynamical evolution of GCs (Boily 2000; Ernst et al. 2007; Kim et al. 2008), it is not yet clear how they affect the formation and the earliest stages of GC evolution. In an attempt to shed some light on this question, we investigate the impact of internal rotation on various cluster parameters like horizontal branch morphology, age, metallicity, and chemical variations. We present evidence that tidal interactions with the Galaxy and two-body relaxation processes might play a crucial role. For the first time we show a relation between the internal rotation to velocity dispersion ratio (A_{rot}/σ_0) with the half-light to Jacobian radius ratio (r_h/r_J) in the sense that GCs, which better fill their Roche lobes are faster rotators. We also see that the relation is better represented by the Young Halo (YH) and bulge GCs, while the Old Halo (OH) clusters generally have little or no angular momentum.

3.2   Observations and data reduction

3.2.1   Spectroscopy

The targets were selected from archival FORS2 pre-imaging in the B and V filters (ESO-programme 71.D-02191B, P.I.: L. Rizzi) and the 2MASS catalogue (Cutri et al. 2003) to cover the entire span of NGC 4372's RGB and includes a number of AGB stars (Figure 3.1). The spectroscopic observations were carried out in service mode on the nights of Feb. 11, Mar. 08, and Mar. 10, 2012 using the Fibre Large Array Multi Element Spectrograph (FLAMES) mounted at the UT2 (Kueyen) of the Very Large Telescope (VLT) on Paranal (Pasquini et al. 2002). Five observing blocks (OB) were executed in total (exposure time 2775 s per OB) using two different Medusa plates. On each mask 133 fibres were fed to the GIRAFFE spectrograph (using the HR13 grating, which covers the wavelength range $6100 - 6400$ Å with spectral resolution R ~ 22000) and eight fibres were fed to the UVES spectrograph. Nineteen of the GIRAFFE fibres were dedicated to the sky and 112 to the RGB/AGB targets. Both plate settings include different targets with a large overlap between them.

We reduced the FLAMES observations with the standard GIRAFFE pipeline, version 2.9.2 (Blecha et al. 2000). This pipeline provides bias subtraction, flat fielding, and accurate wavelength calibration from a Th-Ar lamp. The 19 sky spectra were combined and subtracted from the object spectra with the IRAF task *skysub*. We computed radial velocities of our targets by cross-correlating the spectra with a synthetic RGB spectrum with similar stellar parameters, as expected for our targets, using the IRAF *fxcor* task. All spectra were Doppler-shifted to the heliocentric rest frame and the individual spectra of the same stars (ranging from 2 to 5) were median combined using the IRAF *scombine* task. Finally, we normalised the spectra to the continuum level with the help of the IRAF *continuum* task. The final reduced, one-dimensional spectra have average signal-to-noise ratios (SNR) ranging from 20 to 200 per pixel, depending on the brightness of the stars and the number of the combined individual exposures. The data set consists of 108 different stars with successfully measured radial velocities, of which 64 were confirmed cluster members and the rest were identified as foreground stars.

In the following analysis, we also use a second GIRAFFE data set (ESO-programme 088.D-0026(D), P.I.: I. McDonald) of 123 stars observed in service mode on the nights of Jan. 15, Mar. 04, and Mar. 06, 2012 with the HR13 and HR14 GIRAFFE gratings, and thus, covering a total wavelength range from 6100 Å to 6700 Å. This data-set was reduced with the girBLDRS[2] software in a similar manner. The spectra predominantly cover the brighter RGB/AGB of NGC 4372 (Figure 3.1) and are of high quality (median SNR of ~ 100 per pixel). A radial velocity check and a metallicity estimate confirms 74 of the stars as cluster members, while the rest are classified as foreground contaminants. There is very little overlap between the two samples and we found only

---

[2]`http://girbldrs.sourceforge.net/`
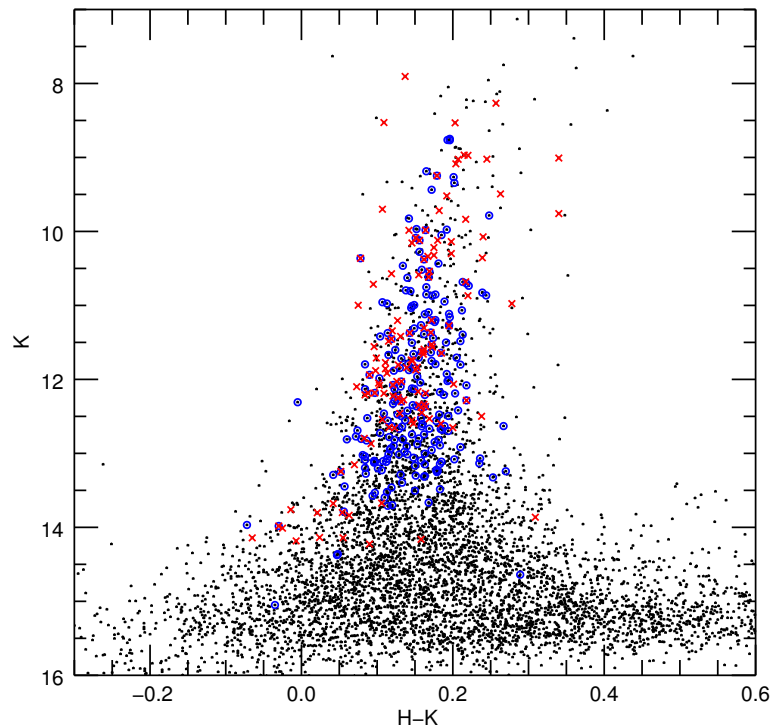
Figure 3.1: 2MASS CMD of NGC 4372. The blue circles indicate all stars (both cluster members and foreground) in the first (088.B-0492) and red crosses indicate all stars in the second (088.D-0026) spectroscopic samples.

eight stars in common, five of which are cluster members. The radial velocities of the common stars agree to within 1 km s^{-1} (mean difference 0.11 km s^{-1} with 1 km s^{-1} standard deviations).

For all stars in both data sets we also have metallicity estimates, which are presented in Chapter 4. The membership of each cluster star is established based on simultaneous radial velocity and metallicity cuts.

Both data sets have essentially the same mean velocity and velocity dispersion, so we decided that it is safe to combine them. Our final NGC 4372 spectroscopic sample consists of 131 unique cluster member stars with K-band magnitude $\lesssim 15$ mag, confirmed from metallicity estimates ($[\text{Fe/H}] < -2.0$) of all the stars in the sample that have radial velocities between 50 and 100 km s^{-1}. The median accuracy of the velocity measurements is 1 km s^{-1}. In Figure 3.2, we compare the radial velocities distribution of our full spectroscopic sample (cluster members plus foreground contamination) with the velocity distribution in this direction of the sky according to the Besançon model of the Galaxy (Robin et al. 2003). The Besançon model predicts about 2100 stars in an area of 0.2 deg^2 within our colour-magnitude selection limits. The mean radial velocity of NGC 4372 of 76 km s^{-1} is, however, quite distinct from the radial velocities of the majority of foreground stars, although a small contamination by such foreground stars is not excluded. But considering the very low metallicity of this GC ($[\text{Fe/H}] \simeq -2.2$ dex) and the clearly metal-rich foreground stellar population, we are confident that we have selected a clean sample of NGC 4372 member stars. About 100 stars from the adopted Galactic model have radial velocities between 50 and 100 km s^{-1} and none of them is more metal-poor than -1.8 dex. We come back to the detailed kinematics of these GC stars in Section 3.4.
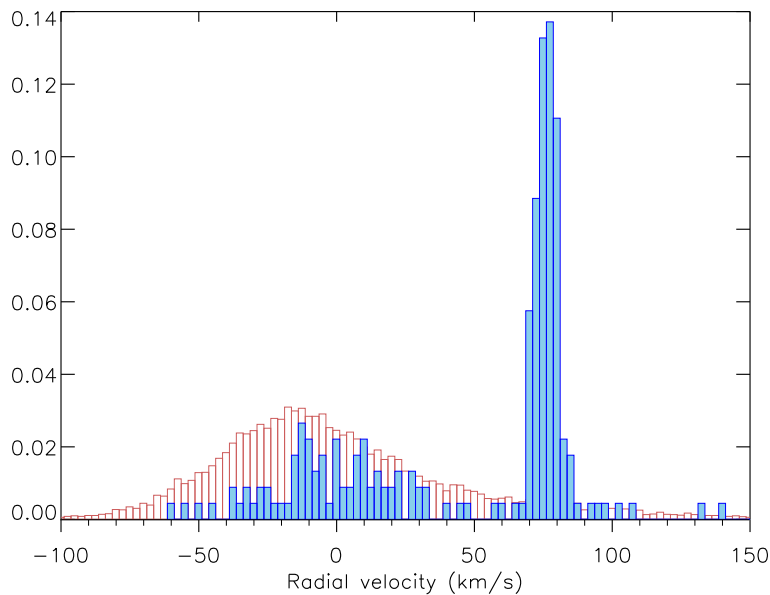
Figure 3.2: Radial velocities' relative frequency of both spectroscopic samples (filled, blue boxes) overplotted over a Besançon model of the field stars in the direction of NGC 4372 (blank, red boxes).

3.2.2   Photometry

We used archival imaging obtained with the Wide Field Imager (WFI) at the 2.2m MPG/ESO telescope at La Silla (Baade et al. 1999). We chose *V*- and *I*-band observations of the cluster taken as part of the 'pre-FLAMES' programme of the ESO Imaging Survey (programme 164.O-0561, PI: Krautter; cf. Momany et al. 2001). These observations cover a field of view (FOV) $30' \times 30'$ centred on the cluster. The basic data reduction, astrometric solution, and combining of mosaics were carried out using the THELI pipeline (Erben et al. 2005; Schirmer 2013). We used the Two Micron All Sky Survey (2MASS) point source catalogue (Skrutskie et al. 2006) as astrometric reference and combined the observations to one stacked, undistorted image per filter. We then obtained instrumental magnitudes for unresolved objects using the DAOPHOT software package (Stetson 1987, 1993) from these images. We fixed photometric zero points to standard stars in the same field taken from the standard star database of Stetson (2000, 2005)[3]. Since we are primarily interested in relative photometry rather than absolute photometry in a given standard system, no colour term was included.

Since NGC 4372 resides behind a strip of Galactic gas and dust, it suffers from severe differential reddening (Hartwick & Hesser 1973; Alcaino et al. 1991; Gerashchenko et al. 1999). In an attempt to correct for this effect, we followed the procedures described in Hendricks et al. (2012) and Milone et al. (2012). The main idea is to estimate the interstellar extinction for each star individually based on the median distance of its nearest neighbours to a fiducial line along the reddening vector. In our case, we used an adaptive number of the nearest neighbours depending on the density of the region, starting from 40 in the innermost $15''$ and using ten stars in the outermost regions. We used only main-sequence stars that have uncertainties on the V- and I-band photometry less than 0.1 mag. A BASTI isochrone (Pietrinferni et al. 2004, 2006) of old age (15 Gyr) and low metallicity ($Z = 0.0003$), shifted to a distance modulus $(m - M)_V = 15.0$ mag (Harris 1996), was used as a fiducial line, representative for this GC. Despite its relatively old age with respect to the age of the Universe, the chosen isochrone represents well the MS, the turn-off point, the RGB,

---

[3]Available at `http://www3.cadc-ccda.hia-iha.nrc-cnrc.gc.ca/community/STETSON/standards/`
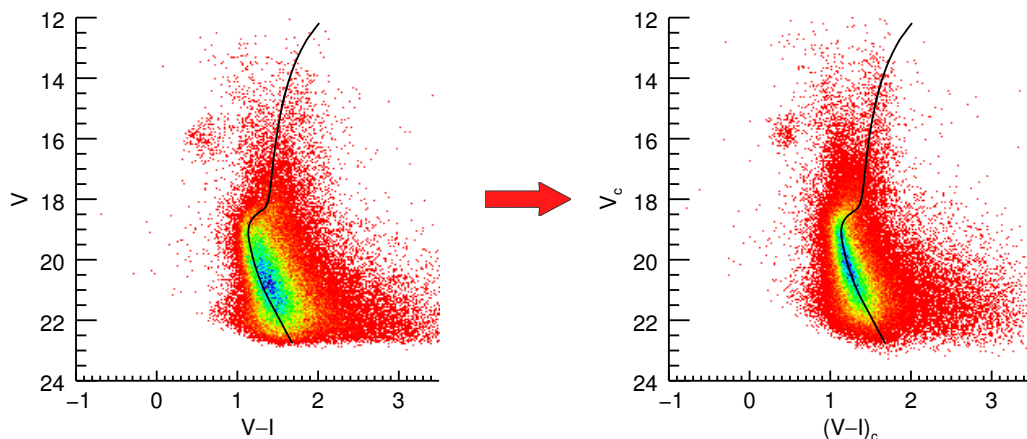
Figure 3.3: Hess diagrams of NGC 4372's CMD before (*left panel*) and after (*right panel*) the differential reddening correction. The BASTI isochrone used as a fiducial line is super-imposed.
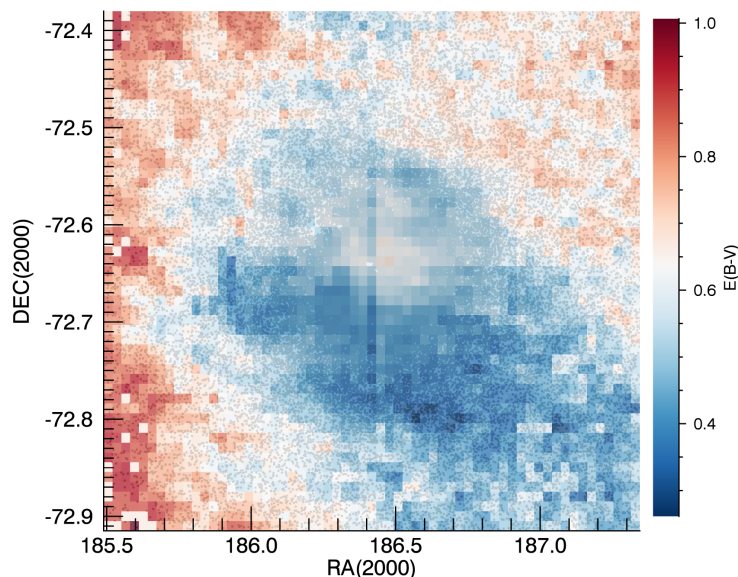
Figure 3.4: A reddening map across the field of NGC 4372.

and the magnitude of the HB. We used the standard interstellar extinction law for the Milky Way where $A_V = 3.1 \times E(B-V) = 2.2 \times E(V-I)$ (Cardelli et al. 1989; Mathis 1990). The results of the de-reddening procedure are presented in Figure 3.3, where we show a Hess diagram of the original raw CMD and the resulting CMD after applying the described algorithm. The de-reddening procedure also corrects for residual variations in the photometry that result from the variation of the point spread function or illumination (e.g. Koch et al. 2004) across the combined mosaics. We find a mean $E(B-V) \sim 0.5$ mag towards NGC 4372 in a good agreement with the Schlafly & Finkbeiner (2011) re-calibration of the Schlegel et al. (1998) extinction map, with a significant variation between 0.3 and 0.8 mag across the field of the GC. A reddening map is presented in Figure 3.4.

To assess the completeness of the photometry, the final WFI photometric catalogue was compared to Hubble Space Telescope (HST) imaging of the central regions of the cluster (Piotto et al. 2002), which covers an area with a radius of about 1.5′ and can be safely assumed to be complete down to $V = 21$ mag. The HST F555W band magnitudes were calibrated to the WFI V-band extinction corrected magnitudes of matching targets. We assumed uniform extinction across the HST
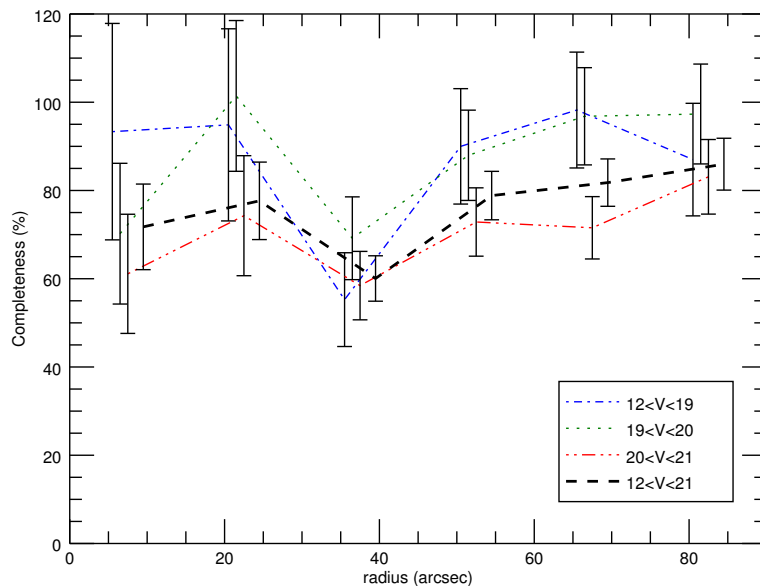
Figure 3.5: Completeness of the WFI photometry compared to Hubble imaging of the innermost $1.5'$ of NGC 4372 in different magnitude and spatial bins. The radial bins are shuffled by $1''$ for clarity.

field, which is justified by its small size. We considered different magnitude ranges and counted the stars in both catalogues in six concentric rings each $15''$ thick assuming Poisson uncertainties. The results are presented in Figure 3.5. Considering all of the stars, the comparison shows a completeness level of $(70 \pm 10)\%$ in the innermost $15''$ that rises to about $(85 \pm 5)\%$ at $90''$ from the cluster centre. This incompleteness is mostly due to the faintest stars in the sample with $V > 20$ mag, where the central $15''$ region has a completeness level of $(60 \pm 15)\%$ that rises to $(80 \pm 10)\%$ in the outer radii. The stars brighter than $V = 20$ mag have a completeness level of about $(90 \pm 15)\%$ across the whole field. An exception is the region at $\sim 30''$, where we observe a sudden drop of completeness in the whole magnitude range.

3.3   Structural parameters

According to the Harris catalogue of GCs (Harris 1996, 2010 version[4]), NGC 4372 has a half-light radius $r_h = 3.91'$, a tidal radius $r_t = 34.9'$, and a concentration parameter $c = \log(r_t/r_c) = 1.3$, where $r_c = 1.75'$ is its core radius. These estimates come from a poorly constrained surface brightness profile presented in Trager et al. (1995). Furthermore, there is discrepant information for the ellipticity of NGC 4372 in the literature (White & Shawl 1987; Chen & Chen 2010). Therefore, we decided to re-derive these parameters independently. It is interesting to check the direction of the flattening to assess the importance of internal rotation (see Section 3.4.2), or to give some insight on its tidal interaction with the Galaxy.

Using the WFI photometric catalogue, corrected for differential reddening and incompleteness in the central regions, we construct a number density, instead of a surface brightness profile, since the former is less sensitive to the presence of individual bright stars and foreground contaminants. It also allows us to work with the full catalogue, instead with a limited number of surface bins. We only considered stars brighter than $V = 20$ mag, where we can safely assume that the sample is 100% complete beyond $90''$.

---

[4]`http://physwww.mcmaster.ca/~harris/mwgc.dat`

3.3.1 The method

We followed a modified version of the maximum likelihood method outlined in Martin et al. (2008) to fit the GC star number density profile. This approach consists of maximizing the log-likelihood function (Eq. 3.1) by iterating a set of free parameters, for which the observations become most probable:

$$\log \mathscr{L}(p_1, p_2, ..., p_j) = \sum_i \log \ell_i(p_1, p_2, ..., p_j) \tag{3.1}$$

where $\ell_i(p_1, p_2, ..., p_j)$ is the probability of finding the measurement i given the set of parameters $p_1, p_2, ..., p_j$. We used a set of six free parameters for our fit: the centroid of the cluster (x_0, y_0), a model-dependent characteristic radius, the global ellipticity[5] (ε), the orientation angle from north to east (θ) of the ellipse major axis, and the contaminating foreground density (n_f) in stars per square arcmin. The centroid is defined as in van de Ven et al. (2006):

$$x_i - x_0 = \sin(\alpha_i - \alpha_0) \cos \delta_i \tag{3.2}$$

$$y_i - y_0 = \sin \delta_i \cos \delta_0 - \cos \delta_i \sin \delta_0 \cos(\alpha_i - \alpha_0) \tag{3.3}$$

where α_i and δ_i are the equatorial coordinates of the stars from the WFI catalogue and $\alpha_0 = 12^h25^m45.40^s$ and $\delta_0 = -72°39'32.4''$ are the central cluster coordinates listed in the Harris catalogue. We chose to work with the projected Plummer family of models (Plummer 1911) of the following type:

$$n(r) = n_0 \left(1 + \frac{r^2}{a^2}\right)^{-2} + n_f. \tag{3.4}$$

In the Plummer profile, the characteristic radius a corresponds to the half-light radius[6] of the cluster. In the above equations, the independent variable r is an elliptical radius (the semi-major axis of the adopted ellipse), which is related to the spatial position (x, y) of the stars in the following way:

$$r = \left\{ \left[\frac{1}{1-\varepsilon} (x\cos\theta - y\sin\theta) \right]^2 + (x\sin\theta + y\cos\theta)^2 \right\}^{1/2} \tag{3.5}$$

and n_0 is the central number density of the cluster. The central number density is not a free parameter but constrained from the total number of stars in the FOV within the selection criteria (N_{tot}) by the equation

$$N_{tot} = \int_{FOV} n(r)dxdy = n_0 \int_{FOV} \left(1 + \frac{r^2}{a^2}\right)^{-2} dxdy + An_f \tag{3.6}$$

where A is the total area of the FOV. From the last expression we can write that

$$n_0 = \frac{N_{tot} - An_f}{\int_{FOV} \left(1 + \frac{r^2}{a^2}\right)^{-2} dxdy}. \tag{3.7}$$

The integration from the above equation is done numerically over the entire FOV by dividing it into small segments with sizes $\Delta x, \Delta y$ much smaller than the expected half-light radius of the cluster (few arcmin).

---

[5]The ellipticity is defined as $\varepsilon = 1 - \frac{b}{a}$, where a and b correspond to the semi-major and semi-minor axis of the ellipse, respectively.

[6]Technically, this is the radius that contains half of the stars. In order to relate this value to the half-light radius, one has to assume an initial mass function, binarity fraction, and segregation distribution. In this work, we use this quantity as a reasonable approximation to the half-light radius.

We iterated the parameters in a Markov Chain Monte Carlo (MCMC) manner following the Metropolis-Hastings algorithm (Hastings 1970), where each new set of parameters is derived randomly from the previous set, from a Gaussian distribution function with a defined standard deviation. The standard deviation for each parameter is chosen such as to optimise the acceptance rate of the Markov chain. A probability based on the likelihood is assigned to the new set of parameters and the chain is continued until we achieve a good sampling of the parameter space. The code was extensively tested with Monte Carlo drawn Plummer clusters with various half-light radii, ellipticities, and uniform background densities to confirm the correctness of the results. Muñoz et al. (2012) explored the conditions under which the outlined approach gives reliable results, namely the size of the FOV, the total number of stars, and the n_0/n_f ratio, which in the case of NGC 4372 are all fulfilled.

3.3.2   Profile fitting

In order to obtain the global structural parameters of NGC 4372, we performed two fits, using all stars brighter than $V = 20$ mag and $V = 19$ mag. In both cases, we assumed that the photometry is complete at radial distances greater than $1.5'$, but we applied completeness corrections according to Figure 3.5 in the central regions.

The results from the MCMC fits are summarised in Table 3.1. The uncertainty intervals in Table 3.1 are defined as the 1σ deviation from the mean of a Gaussian representing the distribution function of each parameter from the Markov chain after excluding the "burn-in" iterations.

Figures 3.6 and 3.7 present the number density profiles of NGC 4372 obtained by using all stars brighter than $V = 20$ mag and $V = 19$ mag, respectively, built in confocal elliptical annuli with $0.1'$ size that have ellipticities and position angles in accordance with the results reported in Table 3.1 for both fits. The best fitting Plummer profiles and rotating models (see Section 3.5.1) are also shown. We note here that the two curves drawn in the figures are not fit to the binned profiles; rather they are a result of the MCMC discrete fitting procedure in the case of the Plummer profile and the simultaneous modelling of the kinematics and number-density profiles in the case of the dynamical, rotating model.

When using stars within different magnitude ranges the derived half-light radii vary significantly (see Table 3.1), while all other parameters used in the fit are consistent within the uncertainties. According to the BASTI isochrones, the stellar mass in the considered magnitude range varies between 0.70 and 0.75 $M_\odot$. Because of this small contrast of masses, together with the overall uncertainties associated with the dereddening procedure and completeness estimation across the large WFI field, it seems difficult to draw conclusions about the mass segregation of the cluster. Instead, we attribute the more extended distribution profile of the fainter stars to still unaccounted incompleteness in the photometry. The very small HST field in which we have assessed incompleteness, however, does not allow us to properly account for incompleteness over the entire field of the WFI photometry. Another possible source of uncertainty comes from the dereddening procedure in which we are using a particular isochrone to correct for differential extinction the GC stellar population. This isochrone is not representative of the field population, which might be partly over-corrected, thereby increasing the relative fraction of contaminating field stars in the fainter samples, making number density fits artificially broader.

In the following analysis we apply the derived centroid corrections (x_0, y_0) to the published coordinates of NGC 4372 in the Harris catalogue. The estimated coordinates of the centre are $\alpha_0 = 12^h25^m51^s$ and $\delta_0 = -72°38'57''$ for epoch 2000.
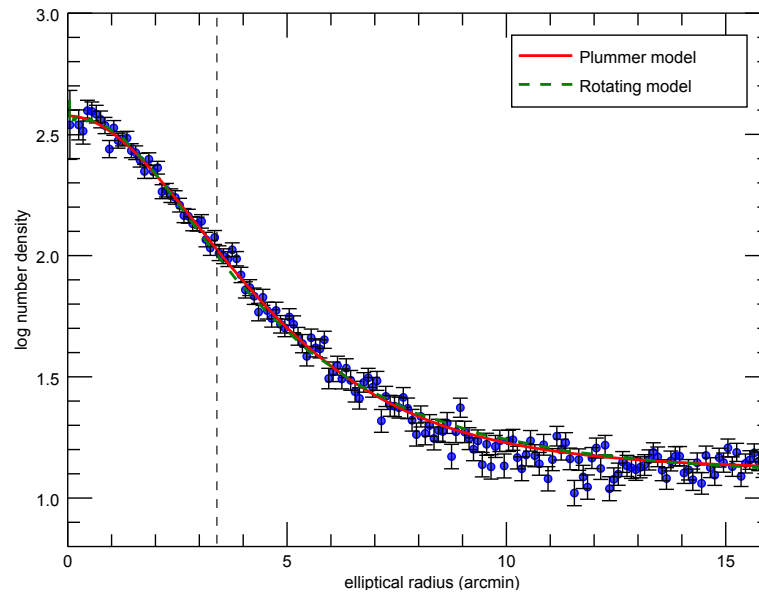
Figure 3.6: Incompleteness corrected number density profile of NGC 4372 built in elliptical annuli of size 0.1′ (blue symbols) using stars brighter than $V = 20$ mag. The best fitting Plummer model (red line), as well as the obtained rotating model (green line, see Section 5.1) are super-imposed The fitted half-light radius is indicated with a vertical, dashed line.
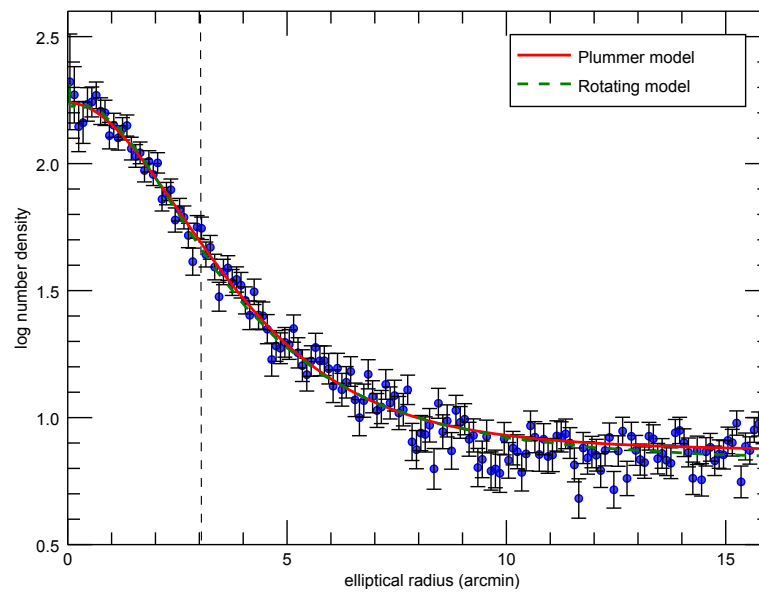
Figure 3.7: The same as Figure 3.6 but using only stars brighter than $V = 19$ mag (the turn-off and RGB/AGB regions).

Table 3.1: Plummer model projected structural parameters from the MCMC fit.

	$V < 20$ mag	$V < 19$ mag
r_h (arcmin)	3.44 ± 0.04	3.03 ± 0.06
x_0 (arcmin)	-0.33 ± 0.03	-0.33 ± 0.05
y_0 (arcmin)	-0.64 ± 0.03	-0.62 ± 0.04
ε	0.08 ± 0.01	0.09 ± 0.02
θ	$48° \pm 6°$	$52° \pm 6°$
N_0[1]	12000 ± 100	4200 ± 70
n_f ($\star/\square'$)	12.82 ± 0.16	7.34 ± 0.11

Notes. [1] $N_0 = N_{tot} - A n_f$ is the estimated number of stars belonging to the cluster, given our magnitude cuts.

3.4 Kinematics

As mentioned in Section 3.2.1, we measured radial velocities from individual exposures using the *fxcor* task in IRAF. This method applies a Fourier cross-correlation between the spectra of interest and a given template and provides velocity error estimates based on the fitted peak height and the antisymmetric noise (Tonry & Davis 1979). The adopted final velocities and their uncertainties are calculated as the error-weighted mean of the different velocity estimates for the same star from different exposures, ranging from 2 to 5 in our sample. For the second sample we averaged the radial velocities measured in the HR13 and HR14 gratings for each star. The radial velocities derived from different exposures of the same star agree well with each other, showing that stellar binaries do not play a significant role.

We used a maximum likelihood approach (Walker et al. 2006; van de Ven et al. 2006, outlined in Section 3.4.1) to calculate the mean radial velocity of NGC 4372 ($v_r = 75.91 \pm 0.38$ km s^{-1}) and its global intrinsic velocity dispersion ($\sigma = 3.76 \pm 0.25$ km s^{-1}) from the discrete velocity measurements. These values are in reasonable agreement with the radial velocity of 72.3 ± 1.4 km s^{-1} and velocity dispersion of 4.3 ± 0.9 km s^{-1}, estimated by Geisler et al. (1995), based on 11 stars.

3.4.1 Maximum likelihood estimation of the mean velocity and velocity dispersion

Our kinematic analysis is based on the radial velocity measurements of all stars in the sample. Each measurement is associated with some uncertainty, which can vary with respect to the quality of the observed spectrum. The observed velocity distribution will then be broader than the intrinsic dispersion of the sample due to the measurement uncertainties. We followed a maximum likelihood approach to derive the mean velocity and velocity dispersion of the selected stellar samples that takes into account the individual errors of each measurement. If v_i and σ_i are the measured radial velocities and their uncertainties, respectively, and u_i are the true radial velocities, we can write that $v_i = u_i + \sigma_i \varepsilon_i$, where ε_i follow standard normal probability distribution. Assuming that the values v_i follow a Gaussian distribution centred on the true mean velocity $\langle u \rangle$, then their joint probability function is simply the product of their individual Gaussian probabilities:

$$\mathcal{L}(\{v_1, ..., v_N\}) = \prod_{i=1}^{N} \frac{1}{\sqrt{2\pi(\sigma_i^2 + \sigma_p^2)}} \exp\left[-\frac{1}{2} \frac{(v_i - \langle u \rangle)^2}{(\sigma_i^2 + \sigma_p^2)} \right], \tag{3.8}$$

where σ_p is the intrinsic velocity dispersion of the sample. The estimates for $\langle u \rangle$ and σ_p are determined numerically by maximising the natural logarithm of the above equation in an iterative

process:

$$\ln \mathscr{L} = -\frac{1}{2} \sum_{i=1}^{N} \ln(\sigma_i^2 + \sigma_p^2) - \frac{1}{2} \sum_{i=1}^{N} \frac{(v_i - \langle u \rangle)^2}{\sigma_i^2 + \sigma_p^2} - \frac{N}{2} \ln(2\pi). \tag{3.9}$$

The confidence intervals for $\langle u \rangle$ and σ_p can be obtained from their covariance matrix.

3.4.2 Central velocity dispersion

In order to estimate the central velocity dispersion σ_0 of NGC 4372, we divide the cluster into five radial bins and used the same maximum likelihood approach to estimate the velocity dispersion in each bin (Figure 3.8), which we approximate with Plummer models. Plummer models describe isotropic stellar systems with constant density cores. We do not claim that this family of models is the best representation for this particular GC, rather we use it as a reasonable approximation. Our velocity dispersion does not allow us to distinguish between different types of models, such as the more physical King models for example. In principle, if mass follows light, as is expected to be the case for Galactic GCs (Lane et al. 2010), the characteristic radius a should be equal to the half-light radius r_h of the cluster.

We fit the resulting velocity dispersion profile in a least-squares sense with a projected Plummer (1911) model (Eq. 3.10) using a characteristic Plummer radius $a = 3.03'$ estimated from the number-density profile for the brighter stars (RGB/AGB and turn-off stars; see Section 3.3.2) and setting the central velocity dispersion σ_0 as a free parameter:

$$\sigma(r)^2 = \frac{\sigma_0^2}{\sqrt{1 + \frac{r^2}{a^2}}}. \tag{3.10}$$

Although we have radial velocity measurements only for RGB/AGB stars in NGC 4372, using an estimate for the half-light radius value derived from the RGB/AGB and turn-off stars together is a compromise between having a statistically large sample of stars for constraining the number-density profile (see Figure 3.7) and using stars with a similar spatial distribution.

Our data suggests a best-fit $\sigma_0 = 4.56 \pm 0.3$ km s^{-1}. The uncertainty is the formal 1σ error computed from the co-variance matrix.

Having estimated the central velocity dispersion, it is straightforward to derive a dynamical mass for NGC 4372. According to an isotropic Plummer model the mass is obtained by the following expression (see e.g. Dejonghe 1987; Mackey et al. 2013):

$$M = \frac{64a\sigma_0^2}{3\pi G}. \tag{3.11}$$

Adopting a heliocentric distance of 5.8 kpc (from the Harris catalogue), our radius translates to $a = 5.1 \pm 0.05$ pc and we obtain $M = 1.7 \pm 0.3 \times 10^5$ M$_\odot$. This value is in agreement with the mass listed in Mandushev et al. (1991), $M = 1.3^{(+1.9)}_{(-0.8)} \times 10^5$ M$_\odot$ based on a mass-luminosity relation. The absolute magnitude of NGC 4372 is $M_V = -7.79$ mag according to the Harris catalogue (2010 version). This corresponds to a luminosity of $L_V/L_\odot = 1.1 \times 10^5$ from which we can estimate the mass-to-light ratio for this GC to be $M/L_V \sim 1.5$ M$_\odot$/L$_\odot$, typical of most GCs (Mandushev et al. 1991; Pryor & Meylan 1993). Thus, NGC 4372 is a typical representative of the old, purely stellar populations without detectable amounts of dark matter.

3.4.3 Rotation

We checked for systemic rotation in NGC 4372, following a well-established method (see e.g. Mackey et al. 2013; Bellazzini et al. 2012; Lane et al. 2009; Lane et al. 2010, and references
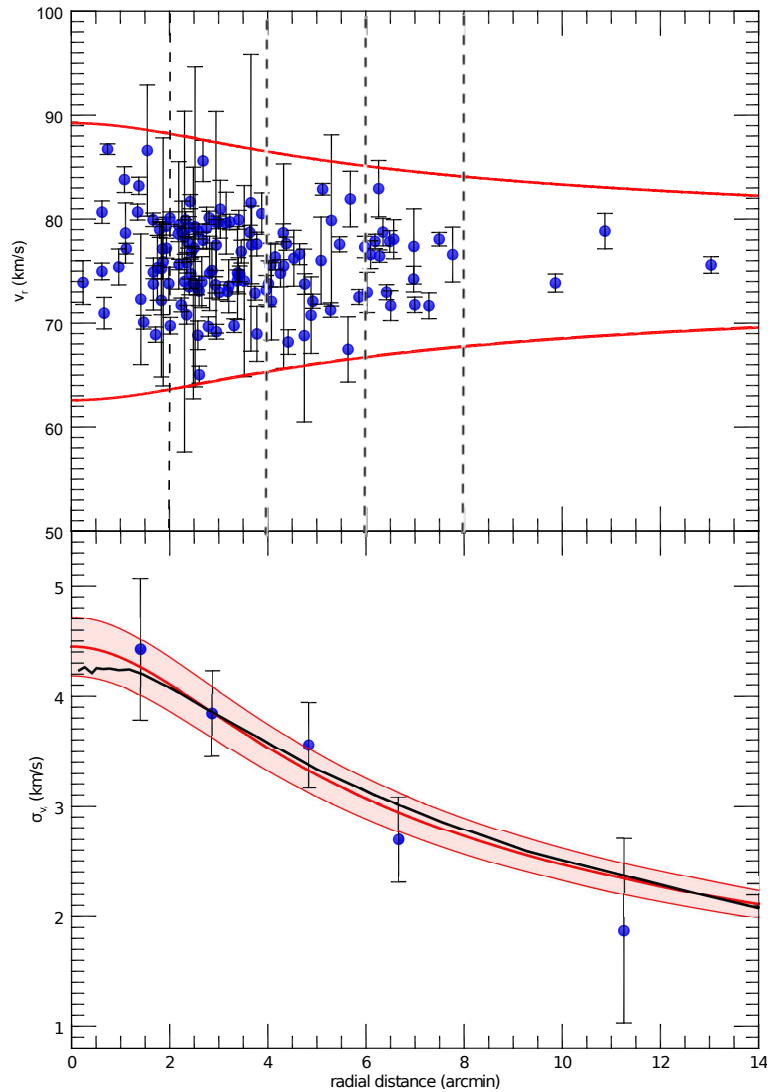
Figure 3.8: *Upper panel:* Radial velocities of the confirmed GC member stars versus radial distance from the centre of NGC 4372. The red curves indicate ±3 times the velocity dispersion as function of the radial distance. The vertical dashed lines indicate the borders of the bins used to compute the velocity dispersion at a given radius. *Bottom panel:* Velocity dispersion profile of NGC 4372 together with the best fitting Plummer profile (thick red line) and the rotating model (thick black line). The shaded area between the two thin red lines indicates the 1σ uncertainty of the Plummer profile.
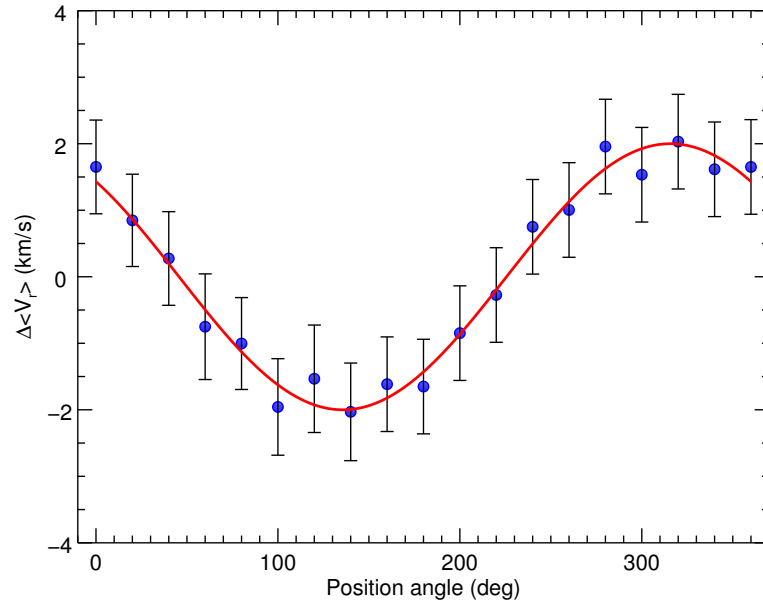
Figure 3.9: Rotation in NGC 4372. The plot displays the difference between the mean velocities on each side of the cluster with respect to a line passing through its centre at a given position angle (measured from north to east, north $= 0°$, east $= 90°$). The red line is the sine function that best fits the data.

therein): To this end, we measured the difference between the maximum likelihood mean velocity on either side of a line passing through the cluster's centre and rotated at different position angles (Figure 3.9). The resulting curve is well described by a sine law of the type $\Delta v_r = A_0 \sin(\theta' + \theta'_0)$, where θ'_0 is the position angle of the rotation axis and A_0 corresponds to two times the amplitude of rotation modified by a factor of $\sin i$. The angle i is the unknown inclination of the GC with respect to the line of sight. Since stellar proper motions for this object are rather unreliable, there is no way to estimate $\sin i$ (see for example Bianchini et al. 2013) and the amplitude of rotation is just a lower limit of the true intrinsic rotation velocity for NGC 4372. The results of the χ^2-fit are $A_0 = 2.0 \pm 0.2$ km s^{-1} ($v_{rot} \sin i = 1.0 \pm 0.1$ km s^{-1}) and the projected rotation axis lies at a position angle of $136° \pm 7°$, measured from north through east. The results remain the same if we fit the sine law to the discrete velocities of the sample at the position angle of each star, rather than to the binned picture presented in Figure 3.9.

The amplitude of rotation, however, varies with the radius as naturally expected with the presence of differential rotation (e.g. Bellazzini et al. 2012; Mackey et al. 2013). The simplest way to show this for NGC 4372 is to construct a rotation profile (Figure 3.10). The figure shows the mean difference between the velocity measured in different overlapping bins along an axis perpendicular to the rotation axis and the systemic radial velocity of the cluster. The resulting curve was then fitted by a simple rotation profile of the form (as in Mackey et al. 2013):

$$v_{rot} = \frac{2A_{rot}}{r_{peak}} \times \frac{X_{\theta'_0}}{1 + (X_{\theta'_0}/r_{peak})^2} \tag{3.12}$$

where r_{peak} is the projected radius at which the maximum amplitude of rotation A_{rot} is measured and $X_{\theta'_0}$ is the distance in arcmin from the cluster's centre along an axis perpendicular to the axis of rotation. For NGC 4372, we found $A_{rot} = 1.2 \pm 0.25$ km s^{-1} at $r_{peak} = 1.3 \pm 0.5'$ from the cluster centre. The estimated A_{rot}/σ_0 ratio is 0.26 ± 0.07. Its meaning is further discussed in Section 5.

The estimated angle of the major axis of the ellipsoid that best fits the number-density profile $\theta \sim 40°$ is perpendicular to the estimated position angle of the rotation axis of NGC 4372 ($\theta' =$
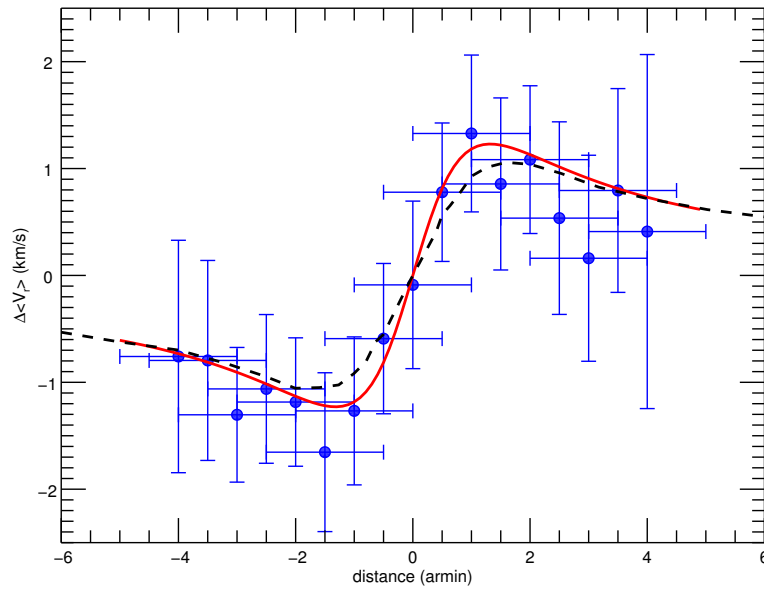
Figure 3.10: Rotation profile of NGC 4372, where the abscissa shows the distance from the centre of the GC along the axis perpendicular to the rotation axis and the ordinate shows the mean offset from the GC's systemic velocity in different overlapping bins. The horizontal error bars indicate the size of the selected bins, while the vertical error bars indicate the formal uncertainty of the mean velocity offset. The best fit, according to Eq. (10), is overplotted with a red line and the rotating model is shown with a black, dashed line.

$136°$). Since our MCMC fitting algorithm is most sensitive to the ellipticity in the inner parts of the cluster and the maximum of rotation is found well within the half-light radius of NGC 4372, we can already conclude that systemic rotation is likely the main driver of the flattening of NGC 4372. Figure 3.11 shows the spatial extent of the RGB/AGB and turn-off stars from our photometric catalogue as well as the stars for which we have radial velocity measurements. The figure illustrates the good alignment between the estimated rotation axis and the direction of flattening of NGC 4372.
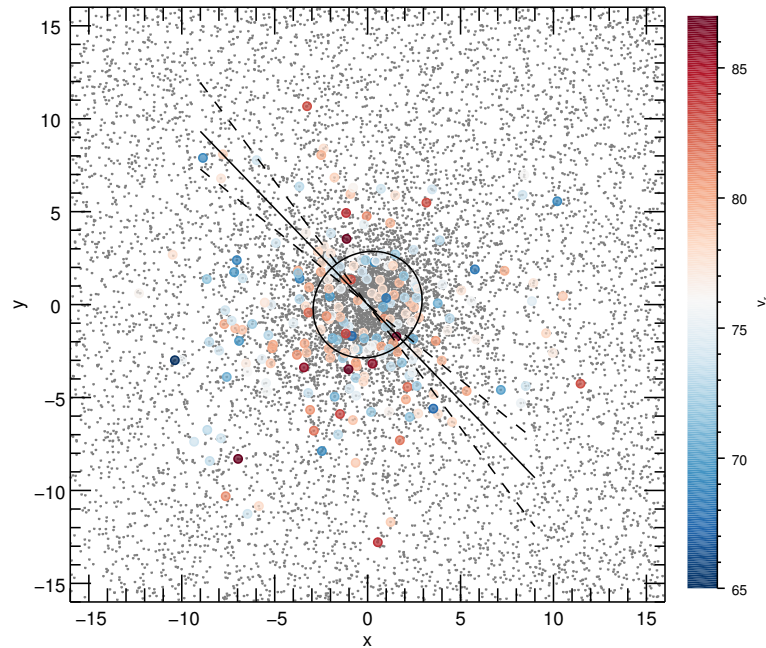
Figure 3.11: Spatial extent of the RGB/AGB and turn-off stars of NGC 4372. Stars for which we have radial velocity measurements are highlighted with colourful symbols, denoting their line-of-sight velocity. The best fitting ellipse for this set of stars (see the last column of Table 3.1) and the rotation axis with its uncertainty are super-imposed.

3.5 Discussion

3.5.1 A dynamical model for NGC 4372

The present section is motivated by the need to provide a global and realistic dynamical interpretation of NGC 4372, taking into consideration all the morphological and kinematic properties we have collected and discussed in the previous sections. In order to carry out a complete dynamical description of NGC 4372 we compare our full set of observations with a family of physically motivated models based on distribution functions, recently applied to a selected sample of GCs (Varri & Bertin 2012; Bianchini et al. 2013). These self-consistent models have been specifically constructed to describe quasi-relaxed stellar systems and to take realistic differential rotation, axisymmetry, and pressure anisotropy into account. The models are defined by four dimensionless parameters (concentration parameter Ψ, rotation strength parameter χ, and the parameters μ and ξ determining the shape of the rotation profile). A full description of the distribution function and of the parameter space is provided in Varri & Bertin (2012).

The comparison between the differentially rotating models and observations requires us to specify the four dimensionless parameters and five additional quantities: three physical scales (i.e. the radial scale r_0, the central surface density n_0, and the velocity scale v_0), the inclination angle i between the rotation axis and the line-of-sight direction, and a foreground contamination term n_f (to be added to the surface density profile). For simplicity, we adopted two fixed inclination angles at $i = 45°$ and $i = 90°$.[7] The fit procedure is conducted in two steps. First, we determine the dimensionless parameters such to reproduce the observed value of A_{rot}/σ_0 and the observed position

---

[7]The inclination angle of the rotating axis is generally not known for globular clusters; given the fact we observe small but yet significant flattening and rotation, we are led to conclude that the angle is likely to be different from $i = 0$. Strictly statistically, $< \sin i >= \frac{\pi}{4}$, therefore the average inclination angle is $< i >= 52°$. A detailed exploration of this additional parameter is beyond the goal of our study.

Table 3.2: Parameters derived from the rotating model.

	$V < 20$ mag $i = 45°$	$V < 19$ mag $i = 45°$	$V < 19$ mag $i = 90°$
	best fit physical scales		
r_0 (arcmin)	2.49 ± 0.05	2.19 ± 0.06	2.23 ± 0.07
v_0 (km s^{-1})	4.81 ± 0.25	4.98 ± 0.26	5.14 ± 0.28
n_0	358 ± 8	165.2 ± 6.9	168.2 ± 10.8
n_f	12.0 ± 0.3	6.7 ± 0.23	6.7 ± 0.15
	derived quantities		
r_h (arcmin)	3.64 ± 0.07	3.20 ± 0.09	3.12 ± 0.10
r_t (arcmin)	37.3 ± 0.75	32.8 ± 0.9	33.4 ± 1.0
r_c (arcmin)	2.25 ± 0.05	1.98 ± 0.05	1.94 ± 0.06
$c = \log(r_t/r_c)$	1.22 ± 0.01	1.23 ± 0.02	1.24 ± 0.03
M_{dyn} (10^5 M$_\odot$)	1.88 ± 0.38	1.97 ± 0.54	1.94 ± 0.61
M/L_V (M$_\odot$/L$_\odot$)	1.7 ± 0.4	1.8 ± 0.5	1.8 ± 0.6

of the rotation peak (for further details see Sect. 3.1 and 3.5 of Bianchini et al. 2013). Second, we calculate the physical scales by minimizing χ^2 simultaneously for the combined photometry (surface density profile) and kinematics (dispersion profile and rotation profile). This provides at once all the constraints needed to determine the best-fit dynamical model.

In the subsequent dynamical analysis, stars will be used as kinematic tracers and we will assume that the stars in our kinematic data sets trace the true stellar mass population of the system. We recall that our dynamical models are one mass component models, and therefore can be applied when the stellar population of the system is homogeneous. In the case of the presence of mass segregation and energy equipartition, however, we expect stars of different masses to have different spatial distribution and different kinematics (Trenti & van der Marel 2013).

Some additional attention is required when using simultaneously photometry and kinematics that refer to stars of different magnitude ranges. Therefore, we compute two models, where the first takes as an input the number density distribution of all stars brighter than $V = 20$ mag (Figure 3.6), and the second one uses only stars brighter than $V = 19$ mag (Figure 3.7). A better χ^2 is obtained when only the number density profile of the brighter stars is used. The computed dimensionless parameters are as follows: $\Psi = 5$, $\chi = 0.16$, $\mu = 0.5$, $\xi = 3$. The derived physical scales and structural parameters (core radius, half-light radius, concentration, total mass, M/L_V) are reported in Table 3.2.

The best-fit model, constrained using the brighter RGB/AGB and turn-off stars, is able to reproduce satisfactorily both the photometric and the kinematic radial profiles. In particular, the model well reproduces the central region and the outer part of the number density profile (see Figure 3.7). For the line-of-sight kinematic profiles, the model is able to reproduce simultaneously the shape of the velocity dispersion profile and of the rotation profile, matching the characteristic rigid rotation behaviour in the central regions, the velocity peak, and the subsequent decline (see Figures 3.8 and 3.10). We ran a two-dimensional realization of the rotating model through the MCMC fitting routine to estimate its flattening due to rotation. Interestingly, the model does not allow significant deviations from spherical symmetry.[8]

The derived estimates of the total dynamical mass from both models of $M_{dyn} = 1.9 \pm 0.4 \times 10^5$ $M_\odot$ and $2.0 \pm 0.5 \times 10^5$ $M_\odot$ are in agreement with the virial estimate reported in Section 4.1, and suggests a mass-to-light ratio M/L_V between 1.4 and 2.3 M$_\odot$/L$_\odot$.

---

[8]Complex interplay between rotation and velocity anisotropy can contribute to the final, morphological properties of the modelled stellar system.

To assess the impact of the unknown inclination angle, we also computed a model assuming the extreme case that we see the cluster edge on ($i = 90°$). The derived parameters from this model are also reported in Table 3.2. Although this assumption provides slightly better χ^2-fit, the derived structural quantities are essentially unchanged and we can conclude that a reasonable choice of the inclination angle (between $45°$ and $90°$) does not have a real impact in our final results. Inclination angles below $30°$ make the rotation signal practically undetectable.

3.5.2   On rotation and ellipticity

While GCs are to a high degree spherically symmetric systems, mild deviations from the perfect sphere (ellipticities up to 0.20) are observed in most of them. Different reasons for what could cause the flattening are discussed in the literature. Amongst other reasons, internal rotation, pressure anisotropy, and external tides have been suggested to have a significant impact (see Goodwin 1997; Gnedin et al. 1999; van den Bergh 2008; Bianchini et al. 2013). Mackey & van den Bergh (2005) also suggested that the observed shape of GCs could be governed by a tri-axial, dark matter, mini halo, in which GCs hypothetically could reside. Although the main paradigm is that there is little or no dark matter around GCs (Baumgardt et al. 2005, 2009; Lane et al. 2009; Lane et al. 2010; Sollima et al. 2012; Ibata et al. 2013), this subject is not yet fully examined because of the lack of radially extended kinematic data sets suitable for dynamical studies in the majority of GCs (Zocchi et al. 2012), unless tidal streams are observed (Mashchenko & Sills 2005a,b).

Plots of the A_{rot}/σ_0 ratio vs. ellipticity (Figure 3.12) are a common tool used to assess the importance of rotation in shaping stellar systems (Davies et al. 1983; Emsellem et al. 2011, in the context of elliptical galaxies). Both the rotational velocity estimates and the observed ellipticities depend on the unknown inclination angles to the line-of-sight and thus constitute lower limits. Taking that into account and the limited radial extent of the available radial velocity data, most of the GCs plotted in Figure 3.12 have ellipticities consistent with the flattening caused by rotation according to a model of a self-gravitating, rotating sphere (Binney 2005). Although the plot shows that in most cases the flattening indeed seems to be caused by significant internal rotation, this is difficult to be proven conclusively with the existing data sets. Both rotation and ellipticity vary with the radial distance from the cluster centre (Geyer et al. 1983; Bianchini et al. 2013), and different factors (including anisotropy) may have different impact at different projected radii. There is, for example, a large systematic discrepancy between White & Shawl (1987) and Chen & Chen (2010), the two most extensive studies on GCs' ellipticities. They are based on different types of data and methods, which are sensitive to different radial distances.

NGC 4372 lies firmly on the sequence described by other GCs in the A_{rot}/σ_0 vs. ε diagram (Figure 3.12) and in good agreement with the dynamical model. This implies that its flattening is mostly caused by its significant internal rotation. This conclusion is additionally supported by the excellent alignment of the rotational axis and the orientation of the best fitting ellipse and is somewhat surprising given its proximity to the Galactic disk, where external tides are expected to play a significant role. The lack of proper motions prevents us from directly assessing the role of anisotropy in velocity space.

3.5.3   How does rotation affect other GC parameters?

Bellazzini et al. (2012) explored the dependence of various cluster parameters on the A_{rot} and A_{rot}/σ_0 ratio using the kinematic results for a sample of 25 Galactic GCs. They found a very strong correlation between the amount of rotation in a GC and its HB morphology, namely that GCs with blue HBs are slower rotators than those with red or extended HBs (Figure 3.13). NGC 4372 is not
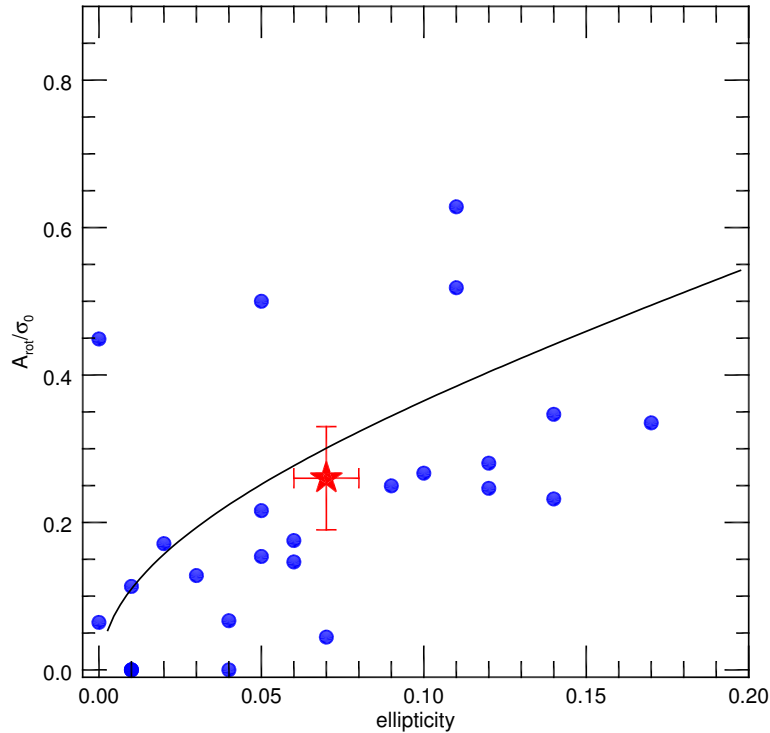
Figure 3.12: The rotation to velocity dispersion ratio plotted as a function of GC ellipticity. The sample of GCs with known A_{rot}/σ_0 values comes from Bellazzini et al. (2012); Bianchini et al. (2013) and the ellipticity information is taken from Harris (1996, 2010 version), except for NGC 4372 (red star), for which we use our own estimates. A model of an isotropic, rotating spheroid is super-imposed for comparison (Binney 2005).

an exception and firmly takes its place as a relatively slow rotator with a very blue HB on this diagram. The HB morphology, however, is one of the most complex parameters that characterise GCs (see Catelan 2009, for a detailed review) and although not completely unexpected, such a strong correlation of the rotation with the HB morphology is difficult to explain since it has to be due to the superposition of multiple effects. Metallicity is the first parameter that shapes the HB morphology (Lee et al. 1990; Fusi Pecci et al. 1993; Gratton et al. 2010) and thus, it is not surprising that Bellazzini et al. (2012) also found a significant correlation between the [Fe/H] abundance and the A_{rot}/σ_0 ratio. They noted, however, that the correlation with metallicity is not as strong as the dependence on the HB morphology and it is unlikely to be the sole parameter. The Spearman rank correlation coefficient determined by (Bellazzini et al. 2012) for each of the discussed relations is shown in Figure 3.13 to give a feeling for their significance. NGC 4372 is one of the most metal-poor GCs in the Galaxy and Figure 3.13 shows that it has a somewhat larger amount of ordered motion for its metallicity. That brings it in line with other outliers on this diagram like NGC 7078 (M 15) and NGC 4590.

Age is widely accepted as being the second most important parameter that shapes the HB (e.g. Searle & Zinn 1978; Lee et al. 1994; Mackey & Gilmore 2004; Mackey & van den Bergh 2005) and is likely to have a significant impact on the rotation of GCs in the sense that older clusters are expected to have dissipated their angular momentum through dynamical relaxation, or could be slowed down by tidal interactions with the Galaxy (Goodwin 1997). In this respect, one could see the left panel of Figure 3.13 as an ensemble of slowly rotating old halo GCs with blue HBs and their rapidly rotating counterparts of young halo clusters with extended or red HBs.

Additionally, Bellazzini et al. (2012) suggested a weak inverse relation between A_{rot}/σ_0 and
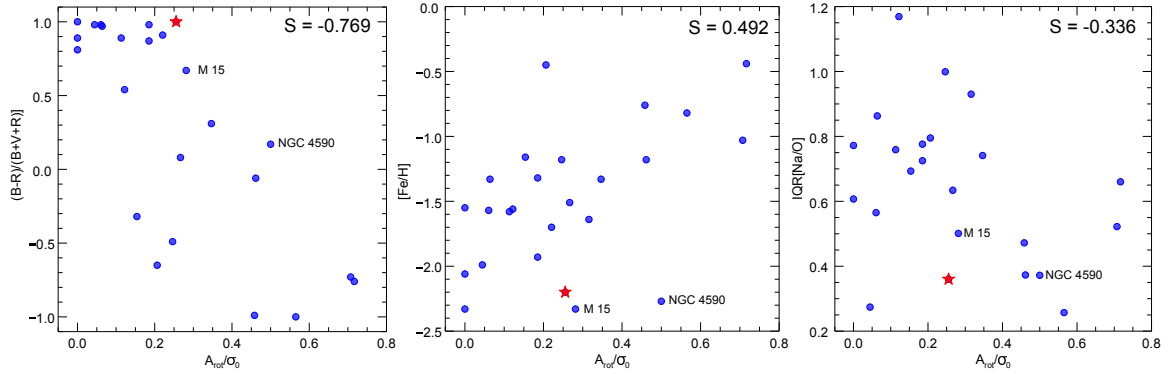
Figure 3.13: The A_{rot}/σ_0 ratio in a number of GCs as a function of different cluster parameters: horizontal branch morphology (*left panel*), [Fe/H] (*mid panel*), and IQR(Na/O) (*right panel*). The Spearman rank correlation coefficient is shown at the upper right corner of each panel. Rotation data are taken from Bellazzini et al. (2012). NGC 4372 has a red star symbol.

the inter-quartile range of the [Na/O] abundance ratio. The latter is a proxy for the extent of the Na and O variations and thus is an indicator of the occurrence of multiple populations in GCs (see Carretta et al. 2009c; Gratton et al. 2012a). While this dependence is not very significant (Spearman rank -0.34), it is likely to be a secondary effect of the HB morphology dependence, since the extended spreads of Na and O abundances in GCs are linked to the extent of He abundances in GCs stars (D'Antona et al. 2002). Helium is important for shaping the HB, as He-enriched stars reach hotter temperatures at the HB stage and GCs with pronounced multiple populations have generally more extended HBs. If we assumed that the relation between the extent of the [Na/O] abundance ratio in a GC and its amount of internal rotation represent a genuine formation process, we would expect to observe a direct dependence instead of a reversed dependence. Indeed, according to the most popular scenarios of GCs formation (D'Ercole et al. 2008; Decressin et al. 2007; Bekki 2010), GCs form a second, dynamically cold, and rapidly rotating stellar population. If this were the case, we would still see the clusters with more numerous, chemically-enhanced population to be faster rotators. NGC 4372 shows the typical of GCs Na-O anticorrelation as our chemical abundance analysis shows. The value for the IQR[Na/O] shown in Figure 3.13 is estimated from abundance measurements of the same GIRAFFE spectroscopic sample presented in this work. The full abundance analysis is presented in Chapter 4.

The amplitude of internal rotation in GCs is also connected to their absolute magnitudes and central velocity dispersions (see Bellazzini et al. 2012). Both quantities are tightly linked to the clusters total mass. NGC 4372 is not an exception in this respect.

In the end, we explore the age-metallicity relation of GCs with respect to their rotation properties (Figure 3.14). Normalised ages are taken from the work of Marín-Franch et al. (2009) based on the Zinn & West (1984) metallicity scale. We have divided the GCs from Bellazzini et al. (2012) and NGC 4372 into slow and fast rotators according to their A_{rot}/σ_0 ratio with respect to the prediction of the isotropic, rotating model shown in Figure 3.12. GCs lying significantly above the predictions of the model are considered as fast rotators. The two well-known branches of GCs in the age-metallicity relation are often interpreted as clusters born *in situ* and accreted on a later stage in the Milky Way halo as indicated in the figure (Marín-Franch et al. 2009; Leaman et al. 2013). Figure 3.14 shows that the majority of fast-rotating clusters are the ones supposedly born *in situ*, while the slow rotators occupy the more metal-poor branch associated with the accreted GCs. The fastest rotating GCs are also the most metal-rich globulars, associated with the Galactic bulge, which are most sensitive to the underlying tidal field of the Milky Way (see the next Section).
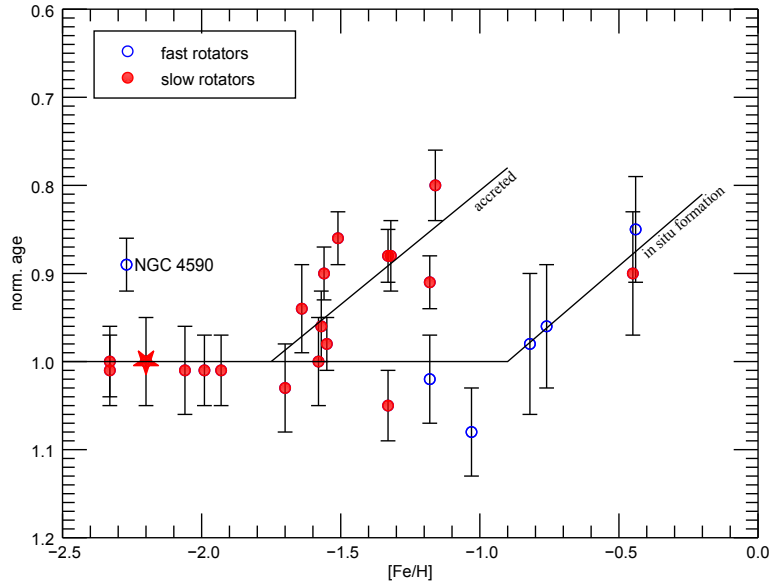
Figure 3.14: Age-metallicity relation for GCs with known rotation properties. The normalised ages are taken from Marín-Franch et al. (2009) based on the Zinn & West (1984) scale. The points are colour-coded based on the A_{rot}/σ_0 ratio. Slow rotators are marked with red and fast rotators with blue. NGC 4372 is marked with a red star. The two sequences of GCs supposedly accreted into the Milky Way halo and born *in situ* are marked with black lines.

Table 3.3: Spearman rank coefficients.

	YH		OH	
	ρ	P	ρ	P
current distr.	0.78	0.008	0.57	0.07
apogalacticon	0.90	0.0003	0.44	0.17
perigalacticon	0.75	0.01	0.71	0.01
	Monte Carlo			
current distr.	0.62	0.004	0.51	0.01
apogalacticon	0.83	0.0005	0.40	0.07
perigalacticon	0.61	0.005	0.72	0.004

3.5.4 The influence of the Galactic tidal field on the internal rotation of globular clusters

The Jacobian radius is the distance from the centre of a cluster to the Lagrangian points L_1 and L_2 (see Figure 1.3). It changes with the Galactocentric distance R as GCs orbit around the Galaxy. Ernst & Just (2013) analytically showed that, within an isothermal halo, r_J scales the same way as the empiric relation of the r_h with the Galactocentric distance ($r_h \propto R^{2/3}$ van den Bergh 1994). Thus, the r_h/r_J ratio, which is an estimate of to what extent a cluster fills its Roche lobe, is considered to be insensitive to the Galactocentric distance (Baumgardt et al. 2010; Ernst & Just 2013).

We followed the method for elliptical orbits described in Ernst & Just (2013) to calculate the Jacobian radius and the r_h/r_J ratio for NGC 4372 and the GCs in the Bellazzini et al. (2012) sample, for which orbital parameters from Dinescu et al. (1999, 2003); Casetti-Dinescu et al. (2007, 2010, 2013) are available.

In Figure 3.15 we show for the first time a relation between the amount of rotation in a GC (A_{rot}/σ_0) and its half-light radius r_h to Jacobian radius r_J ratio. It shows that GCs, which better fill
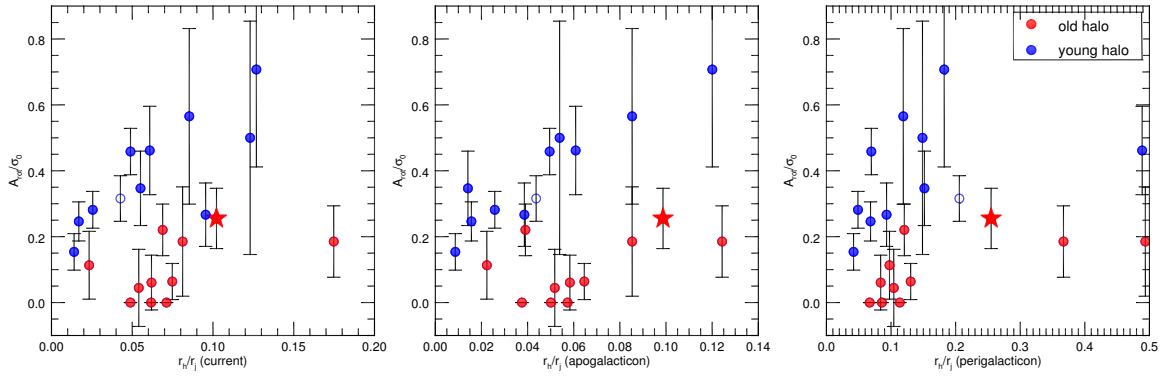
Figure 3.15: The rotation to velocity dispersion ratio as a function of the half-mass vs. Jacobian radius ratio in a sample of GCs from (Bellazzini et al. 2012) and NGC 4372. Since the Jacobian radius is a function of time, we show the current distribution (*left panel*), as if all clusters were in their apogalacticon (*mid panel*), and in their perigalacticon (*right panel*). The GCs are divided into old and young halo groups according to their HB morphology. There is no HB morphology index for NGC 5139 (ω Cen; open blue circle) but it is considered a YH cluster (Marín-Franch et al. 2009). NGC 4372 is indicated with a red star symbol.

their Roche lobes have higher degree of internal rotation. We colour-coded the GCs according to their HB morphology. We show with red GCs that have typical blue HBs and are generally associated with the OH cluster population. On the other hand GCs marked with blue in the figure have extended or red HBs, typically associated with the YH group and the Galactic bulge, respectively (see Mackey & van den Bergh 2005). If we assume that the half-light radius of a particular GC does not significantly vary as it orbits around the Galaxy, we can plot the relation as if all GCs were in their apogalacticon (furthest away from the Galactic centre) or perigalacticon (closest point of the orbit to the Galactic centre). The relation is in any case conserved and thus independent of the current position of the GCs along their orbits.

We quantified the significance of the observed relation using a Spearman rank test. The results are summarized in Table 3.3. The value ρ is the Spearman rank relation coefficient and the value $P \in (0, 1)$ denotes the two-sided significance of its deviation from the null hypothesis that the considered quantities are not related. In order to take into account the uncertainties of the A_{rot}/σ_0 ratio, we performed a Monte Carlo test by drawing 10000 possible distributions of the available GCs in the A_{rot}/σ_0 - r_h/r_J plane and evaluated the Spearman rank for each of them. The modes of the Spearman rank distribution and the significance are also presented in Table 3.3. We conclude that it is highly unlikely to observe such correlation coincidentally.

The physical explanation behind this relation can be that clusters with higher r_h/r_J ratios are more sensitive to the Galactic tidal field and thus are more likely to lose stars. The preferential loss of stars on prograde orbits (see e.g. Oh & Lin 1992; Gnedin et al. 1999; van de Ven et al. 2006) would enhance the cluster's internal rotation. Additionally, dynamically younger and not fully relaxed systems might be more prone to gain angular momentum through the dynamical interaction with an external tidal field. This determines the stronger trend observed in the young halo and bulge GC population.

Finally, N-body simulations of GCs in a tidal field offer an intriguing alternative to the interpretation of the observed velocity gradients in GCs as an evidence of rotation. It is possible that we actually see the effect of tidal, stellar streams escaping the cluster in opposite directions instead of actual rotation (Lützgendorf, Küpper, private communication).

3.6 Summary

We presented the first in-depth study of the structure and kinematics of the old, metal-poor GC NGC 4372. We used archival deep *V*- and *I*-band images from the WFI camera mounted at the MPG/ESO 2.2 m telescope to obtain a CMD of the cluster. NGC 4372 is known to suffer from a severe differential reddening. We used a well-established method to correct for it and showed that the mean $E(B-V)$ is 0.5 mag but varies between 0.3 and 0.8 mag across the observed field. We made a cut at $V = 20$ mag in the extinction corrected CMD and used the resulting catalogue to obtain a number density profile of this GC. Using a MCMC maximum likelihood fitting procedure we derived the centroid of the cluster, its half-light radius ($r_h = 3.44 \pm 0.04'$), ellipticity ($\varepsilon = 0.08 \pm 0.01$), and foreground stellar density, by considering a Plummer distribution.

In order to derive the kinematic properties of NGC 4372, we used high resolution spectroscopic observations from the FLAMES spectrograph at the VLT. Based on precise radial velocity measurements and metallicity estimates, we selected a clean sample of 131 NGC 4372 RGB/AGB stars. With this radial velocity sample we derived a rotation profile extending to the cluster half-light radius. These observations show that the cluster has a significant internal rotation with a maximum amplitude of $A_{rot} = 1.2 \pm 0.25$ km s^{-1}. On the other hand, the best-fit velocity dispersion profile indicates a central velocity dispersion of $\sigma_0 = 4.56 \pm 0.3$ km s^{-1}. The resulting A_{rot}/σ_0 ratio of 0.26 ± 0.07 is relatively large for NGC 4372's low metallicity and old age. Our results show that NGC 4372 is flattened in the direction of its internal rotation (i.e. perpendicular to its rotation axis), which is the most likely reason for deviations from sphericity.

Our observational results allow us to construct a realistic dynamical model of NGC 4372. We compared our full set of observations with a family of physically motivated models, based on distribution functions, specifically constructed to describe quasi-relaxed, differentially rotating stellar systems. The best fitting model is a good representation of the number density and velocity dispersion profile of this GC, as well as its differential rotation, however, being highly spherical, the model fails to reproduce the observed flattening of the cluster. Based on this model, the total dynamical mass of NGC 4372 is $\sim 2 \times 10^5$ M$_\odot$ with a mass-to-light ratio M/L_V between 1.4 and 2.3 M$_\odot$/L$_\odot$. We found that the modelled quantities depend very weakly on the adopted inclination angle.

Finally, we discuss the importance of internal rotation (and particularly the A_{rot}/σ_0 ratio) of NGC 4372 to its morphology and chemical composition by comparing it to similar studies of other GCs (see Bellazzini et al. 2012). We argue that the presumably less relaxed young halo and bulge GCs have generally higher A_{rot}/σ_0 ratios. We also show that NGC 4372 (an archetypical old halo GC) has unusually high A_{rot}/σ_0 ratio for its low metallicity, but it could still be considered a slow rotator when compared to the young halo GC population. When we consider the two distinct branches of GCs in the age-metallicity relation, we notice that the fast rotating GCs are those presumably born *in situ*, while the slow rotators occupy predominantly the branch of the presumably accreted GCs. This is not surprising because the more metal-rich (*in situ*) population is generally more centrally concentrated and therefore, more responsive to the tidal interactions with the Milky Way. We discovered a significant correlation between the A_{rot}/σ_0 ratio and the r_h/r_J ratio for the young halo and bulge GCs, suggesting that tidal interactions with the Galaxy are crucial for gaining angular momentum at younger age, which is gradually lost when relaxation processes take over with time.

4

Chemical abundance analysis of the old metal poor globular cluster NGC 4372 [1]

4.1 Introduction

In this chapter, we present the first chemical abundance measurements of the GC NGC 4372 - a relatively nearby ($R_\odot = 5.8$ kpc) and yet neglected GC in the inner Galactic halo. We presented the GC in the previous chapter, where we described our comprehensive kinematic analysis of NGC 4372, which showed that the cluster has a significant degree of internal rotation for its low metallicity and old age. Although it is well described by an isotropic Plummer profile, it is flattened in the direction of its rotation axis. In the current chapter we continue with the chemical analysis based on abundance measurements derived from the same data set.

4.2 Observations and data reduction

We used two independent spectroscopic samples observed in service mode using the multi-object instrument Fibre Large Array Multi Element Spectrograph (FLAMES) mounted at the UT2 (Kueyen) of the Very Large Telescope (VLT) on Paranal (Pasquini et al. 2002). The first sample (ESO programme 088.B-0492(A), P.I.: A. Koch, 108 targets) was observed with the HR13 grating of the GIRAFFE spectrograph and covers a wavelength range $6100 - 6400$ Å, while the second one (ESO-programme 088.D-0026(D), P.I.: I. McDonald, 123 targets) was observed in the HR13 and HR14 gratings and thus covers a longer wavelength range $6100 - 6700$ Å. Both samples have a spectral resolution R $\sim$ 22000. They both include targets from the entire span of the NGC 4372 RGB but the first sample includes predominantly fainter RGB stars with a median SNR of 55 per pixel and we refer to it in this chapter as the "fainter spectroscopic sample", while the second one includes brighter RGB and AGB stars (median SNR 100 per pixel) and we refer to it as the "brighter spectroscopic sample (Figure 3.1).

We refer the reader to Chapter 3 for a detailed description of the data reduction and cluster member selection. Based on precise radial velocity measurements and preliminary metallicity estimates, we identified 64 stars as cluster members from the fainter spectroscopic sample and 72

---

[1] The work presented in this chapter was done in collaboration with A. Koch, G. Ruchti, and C. I. Johnson.

from the brighter one. There is a very little overlap between the two samples, as we found only 8 stars in common (five of which were identified as cluster members).

4.3   Stellar parameters and iron abundances

We derived the stellar parameters and metallicities of our spectroscopic sample of NGC 4372 stars automatically, using the spectral synthesis code *"Spectroscopy Made Easy"* (SME) (Valenti & Piskunov 1996), iterating simultaneously their effective temperatures, metallicities, micro- and macro-turbulence velocities, and rotational velocities ($v \sin i$). We used photometric temperatures based on the 2MASS colours (Cutri et al. 2003) and the calibrations of González Hernández & Bonifacio (2009) as initial guess for the effective temperatures of the stars. Gravities were kept constant during the fit and were estimated from the canonical Eq. (4.1), using the 2MASS magnitudes, adopting distance modulus of 13.81 mag, uniform reddening of $E(B-V) = 0.39$ mag, and stellar masses $\mu = 0.78$ M$_\odot$.

$$\log g = \log(\mu/\mu_\odot) + 4\log(T/T_\odot) - 0.4(M_\odot - M) + \log g_\odot \tag{4.1}$$

In the above equation, M denotes the absolute bolometric magnitude of the stars. Although, NGC 4372 suffers from a substantial differential reddening that varies by $\Delta E(B-V) = 0.5$ mag across the cluster's field (Kacharov et al. 2014), this variation has a negligible effect on the $\log g$ estimates. The effective temperature, on the other hand, is more sensitive to reddening variations but the adopted photometric temperatures are only used as initial guess parameters, which are optimised during the spectral fitting procedure. The spectroscopic temperatures are fully independent on extinction variations. After the spectral fitting, we modified our adopted gravities using the spectroscopically derived effective temperatures. Finally, the initial input for the microturbulence velocities was estimated using an empirical formula that takes into account the gravities, effective temperatures, and the metallicities of the stars (Ruchti, private communication).

For the spectral synthesis, we used one-dimensional, spherical, α-enhanced, LTE Marcs 2012 stellar atmosphere models (Gustafsson et al. 2008) and a line-list extracted from the VALD database (Kupka et al. 1999, 2000) over the whole wavelength span of our spectra. We used 22 Fe I and Fe II lines to fit the stellar parameters in the fainter spectroscopic sample ($6000 - 6400$ Å) and 34 Fe I and Fe II lines for the brighter sample ($6000 - 6700$ Å). The continuum was fit simultaneously using continuum masks, automatically generated by applying a sigma-clipping algorithm. The goodness of the fit, expressed as the mean line RMS was generally better than 2%. We managed to successfully derive the stellar parameters and iron abundances for 57 stars in each of the two samples. Despite the unfortunate location of NGC 4372, covered by interstellar gas and dust clouds and suffering from severe differential reddening, the spectral synthesis lead to reasonably well constrained spectroscopic stellar parameters that result in a relatively narrow Hertzsprung-Russell diagram well described by theoretical isochrones, where the RGB and AGB are clearly separated (Figure 4.1).

The SME code provides formal uncertainties to the derived stellar parameters, based on the goodness of the fit. These are, however, strongly underestimated as the real uncertainties of the stellar parameters are dominated by systematics and degeneracies between them (see e.g. McWilliam et al. 1995). To account for that, we selected 4 stars covering a wide range of effective temperatures, gravities, and SNR and injected an appropriate level of random noise to their best fit synthetic spectra to match the original SNR of the observed spectrum. Then we re-analysed these noise-injected synthetic spectra the same way we analysed the real data. We repeated this procedure 30 times for each star. The results show that the 1σ uncertainties for the stars that have SNR > 100 per px are as follows: $\Delta T_{eff} \sim 15$ K, $\Delta[\text{Fe/H}] \sim 0.02$ dex, and $\Delta v_{mic} \sim 0.04$ km s^{-1}. For stars that have SNR < 100 per px, respectively, the 1σ uncertainties of the derived parameters are $\Delta T_{eff} \sim 40$ K,
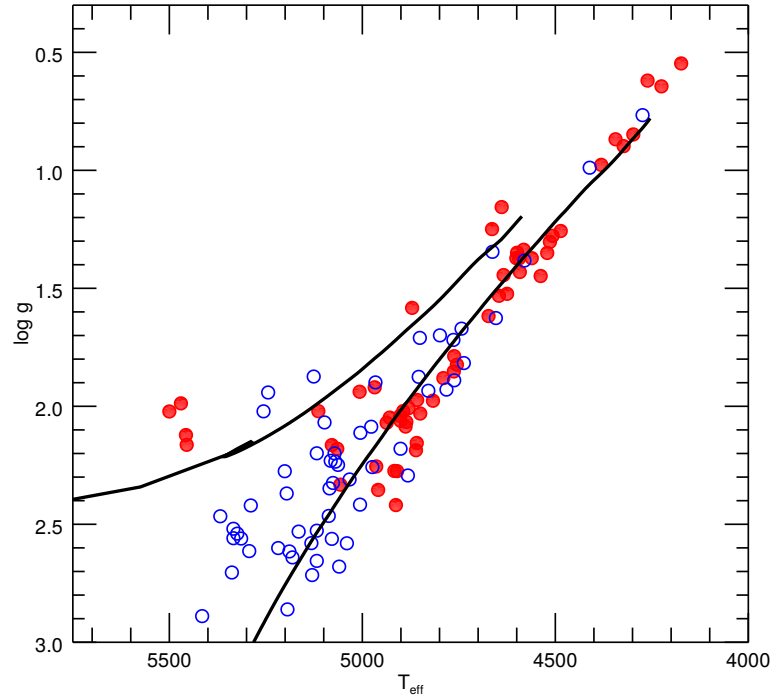
Figure 4.1: Hertzsprung-Russell diagram of NGC 4372 based on the derived stellar parameters. Only confirmed cluster member stars are shown. A BASTI isochrone (Pietrinferni et al. 2004, 2006) representative for the cluster with Z= 0.0003 and age 15 Gyr is overimposed for comparison. The brighter stars spectroscopic sample is marked with red, solid circles and the fainter stars sample with blue, open circles.

$\Delta[\text{Fe/H}] \sim 0.03$ dex, and $\Delta v_{mic} \sim 0.15$ km s^{-1}. We note, however, that the stated uncertainties are still a lower limit since in this case we are fitting a spectrum derived from the same atmospheric model and line list as used by the fitting procedure. Uncertainties in the atomic data, the limited applicability of the adopted stellar atmospheres, and departures from LTE will also influence the obtained parameters.

The mean metallicity that we derive for NGC 4372 from the brighter stars sample is $[\text{Fe/H}] = -2.25 \pm 0.01$ dex with an intrinsic spread of $\sigma_0 = 0.06 \pm 0.005$ dex, while for the fainter sample, we obtain slightly higher metallicity $[\text{Fe/H}] = -2.22 \pm 0.01$ dex with the same intrinsic spread of $\sigma_0 = 0.06 \pm 0.01$ dex. To estimate the mean [Fe/H] and its intrinsic spread we used a maximum likelihood approach that takes into account the discrete measurements with their corresponding uncertainties. The slightly higher metallicity of the fainter sample is mostly driven by a trend of the estimated metallicities with the effective temperature (Figure 4.2). The correlated metallicities and temperatures in the fainter sample undoubtedly introduce larger systematic uncertainties in the derived parameters of these stars. We looked for different reasons where this trend could arise from, including keeping fixed some of the fitting parameters like the microturbulence velocity or assuming departure from local thermodynamic equilibrium (NLTE effects). The NLTE corrections in the regime of these stars are, however, expected to be positive and larger for hotter stars (Lind et al. 2012; Ruchti et al. 2013) and thus, cannot account for the observed trend. We conclude that the degeneracy between [Fe/H] and effective temperature becomes unsolvable by the spectral fitting algorithm for the faintest stars with lowest SNR in our sample.

We estimated the systematic uncertainties of [Fe/H] caused by uncertainties in the stellar, atmospheric parameters by varying the effective temperature by $\Delta T_{eff} = \pm 100$ K, the gravity by $\Delta \log g = \pm 0.2$ dex, and the microturbulence by $\Delta v_{mic} = \pm 0.2$ km s^{-1} (these are rather conservative
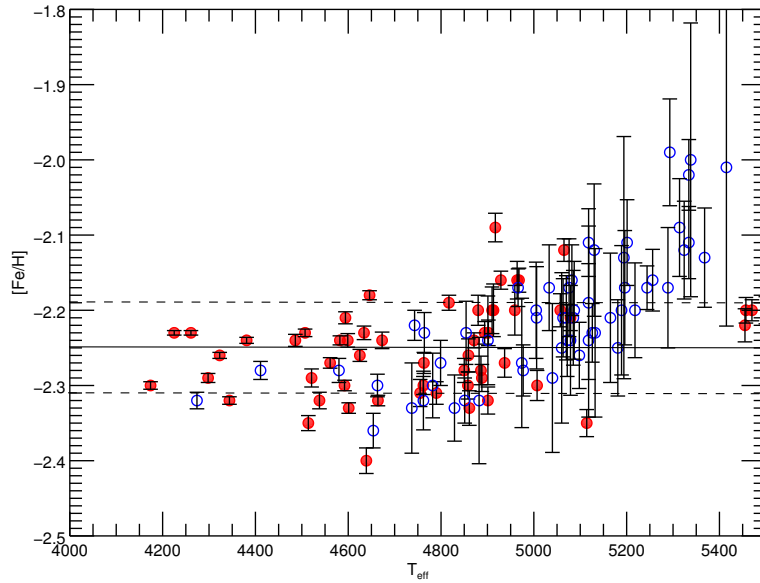
Figure 4.2: Trends of metallicity with temperature for both spectroscopic samples. The mean metallicity of the brighter spectroscopic sample, as well as the $\pm 1\sigma$ spread are indicated with a solid and dashed lines, respectively. Symbols are as in Figure 4.1.

Table 4.1: Systematic uncertainties of [Fe/H].

ID	T_{eff}	$\log g$	v_{mic}	[Fe/H]	ΔT_{eff}		$\Delta \log g$		Δv_{mic}	
	[K]	[dex]	[km s^{-1}]	[dex]	+100 K	−100 K	+0.2 dex	−0.2 dex	+0.2 km s^{-1}	−0.2 km s^{-1}
S2553[1]	4323	0.94	1.62	−2.26	+0.13	−0.15	0.00	−0.01	−0.05	+0.05
S1856[1]	4594	1.38	1.75	−2.21	+0.10	−0.15	−0.01	0.00	−0.04	+0.04
S0985[1]	4901	2.24	1.73	−2.32	+0.08	−0.11	−0.01	−0.01	−0.03	+0.03
S2096[1]	5500	2.02	0.31	−2.20	+0.06	−0.09	0.00	−0.01	−0.01	+0.01
F1755[2]	4274	0.80	1.87	−2.32	+0.15	−0.14	+0.01	0.00	−0.04	+0.05
M9783[2]	4799	1.76	1.63	−2.27	+0.11	−0.11	0.00	0.00	−0.03	+0.04
M10482[2]	5244	1.95	1.68	−2.17	+0.08	−0.08	0.00	0.00	−0.01	+0.02

Notes. [1] The star belongs to the brighter spectroscopic sample. [2] The star belongs to the fainter spectroscopic sample.

values) in seven selected stars that cover the full observed range of temperatures and gravities - four stars belonging to the brighter and three to the fainter spectroscopic samples. The results for [Fe/H] are presented in Table 4.1. One can see that the iron abundance is most sensitive to changes in the effective temperature, which dominates the systematic uncertainty. We also note that the systematic errors are smaller for hotter stars. We used these stars to also estimate the systematic uncertainties of all other chemical abundances considered in this work in a similar manner by additionally adding an uncertainty in the metallicity of [Fe/H]= ± 0.1 dex. The systematic uncertainties, averaged for all stars in each sample and combined in quadrature, are presented in Table 4.2. The systematic errors of the different species are dominated by the uncertainties of different stellar parameters. Barium is the only element, which is sensitive to changes in [Fe/H].

4.4   Abundances of other elements

We also used SME to derive the abundances of various chemical elements (O, Na, Si, Ca, Ti, Sc, Ti, Ni, Ba, Eu) that had detectable lines in the available spectral range. The line-list was assembled

Table 4.2: Mean abundances of NGC 4372

	n^1	$[X/Fe]^1$	$\sigma_0^{\ 1}$	$\varepsilon_{sys}^{\ 1}$	n^2	$[X/Fe]^2$	$\sigma_0^{\ 2}$	$\varepsilon_{sys}^{\ 2}$
[O/Fe]	18	0.72 ± 0.04	0.30 ± 0.11	0.12	...	...	...	...
[Na/Fe]	53	0.76 ± 0.04	0.22 ± 0.02	0.10	46	0.69 ± 0.06	0.35 ± 0.05	0.09
[Si/Fe]	51	0.42 ± 0.02	0.14 ± 0.02	0.11	42	0.24 ± 0.04	0.23 ± 0.03	0.09
[Ca/Fe]	52	0.44 ± 0.01	0.00 ± 0.00	0.14	57	0.37 ± 0.01	0.07 ± 0.03	0.10
[Sc/Fe]	55	0.03 ± 0.01	0.00 ± 0.00	0.11	44	-0.08 ± 0.02	0.08 ± 0.02	0.16
[Ti/Fe]	55	0.18 ± 0.02	0.14 ± 0.01	0.14	54	0.12 ± 0.03	0.12 ± 0.02	0.10
[Ni/Fe]	56	-0.05 ± 0.01	0.00 ± 0.00	0.16	...	...	...	...
[Ba/Fe]	57	-0.06 ± 0.03	0.17 ± 0.03	0.19	56	-0.10 ± 0.04	0.30 ± 0.05	0.14
[Eu/Fe]	44	0.40 ± 0.04	0.23 ± 0.02	0.10	...	...	...	0.21

Notes. [1] The column refers to the brighter stars spectroscopic sample. [2] The column refers to the fainter stars spectroscopic sample.

from the VALD database (Kupka et al. 1999, 2000) and complemented with hyperfine structure (HFS) data for the elements Sc, Ba, and Eu from McWilliam et al. (1995). The derived abundances were placed on the Solar scale of Asplund et al. (2009). We present the error weighted mean abundances ([X/Fe]) for NGC 4372 in Table 4.2. The column σ_0 shows the intrinsic standard deviation of the abundances within the measured stars. Since, we see some small systematic offsets in the measured average abundances between the two analysed samples, we decided to present them separately. The offsets are likely due to the mentioned in the previous section trend of the iron abundance with temperature in the fainter stars sample and to some extent due to the different quality of the spectra, which could lead to larger systematic offsets.

4.4.1   Light element variations - Na & O

We know that the elements processed through the CNO, NeNa, MgAl nuclear cycles show significant spreads in all Galactic GCs studied to date (see Gratton et al. 2012a). It is still under debate what causes such variations within a single GC but the answer to this problem holds important clues to the origin and formation mechanisms of GCs with consequential implications to galaxy formation theories.

Sodium and oxygen are the only available p-capture elements with detectable lines in our spectra. We relied on a single Na line (the one at 6160 Å) to derive Na-abundances for a large fraction of the stars. On the other hand, the two available O lines at 6300 Å and 6363 Å are very weak and disappear at higher temperatures. Therefore, we could derive O abundances only for 18 bright stars with high SNR. NGC 4372 shows the typical for all Galactic GCs Na-O anticorrelation (Figure 4.3). The anticorrelation in NGC 4372 is not very extended but with interquartile range of the [Na/O] ratio $IQR_{[Na/O]} = 0.37$ dex, it is typical for less massive GCs with narrow horizontal branches. The derived Na and O abundance in this GC are somewhat higher than typically expected (Carretta et al. 2009c). Considering the relatively low radial velocity of NGC 4372 of 76 $km\,s^{-1}$(Kacharov et al. 2014), this might be because of unaccounted blends with interstellar or telluric lines. Sodium is sensitive to NLTE effects but in the regime of our stars, the corrections are small ranging between -0.05 dex for the cooler stars, up to -0.10 dex for the warmer ones (Lind et al. 2011).

4.4.2   Alpha-elements - Si, Ca & Ti

The α-elements like O, Ne, Si, S, Ar, Ca, and Ti are produced in the cores of massive stars and during the explosions of core collapse supernovae (SNe type II) and distributed to the ISM pre-
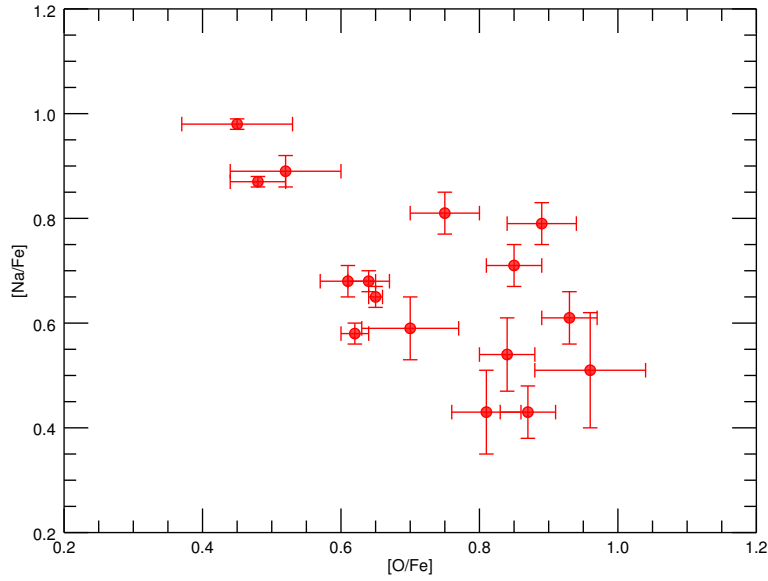
Figure 4.3: Na - O anticorrelation in NGC 4372.

dominantly through their ejecta. Iron, on the other hand, is mainly distributed through the ejecta of SNe type Ia that dominate the ISM on a much later time scale. Therefore, the [α/Fe] ratio is a powerful tool for diagnosing the star formation rate of any stellar population (Tinsley 1979). In the Milky Way, the [α/Fe] ratio forms a plateau at low metallicity and then starts to gradually drop as metallicity is increasing above [Fe/H] ~ -1 dex. The mean [α/Fe] of metal poor Galactic GCs fall on the plateau, while the metal rich (bulge) GCs have low [α/Fe] ratios. This shows that GCs' mean [α/Fe] ratios are representative of the environment they live in. There are some notable exceptions, usually associated with disrupting dwarf galaxies (Pritzl et al. 2005). The dwarf galaxies have generally lower [α/Fe] ratios in accordance with their lower star formation rates (Shetrone et al. 2001, 2003; Venn et al. 2004; Tolstoy et al. 2009; Hendricks et al. 2014, and references therein).

We measured one Si I line at 6155 Å, one Ti I line at 6261 Å, and multiple Ca I lines (at 6122 Å, 6161 Å, 6162 Å, 6166 Å, 6169 Å, and 6455 Å for the brighter stars sample and the lines at 6122 Å, 6162 Å, and 6169 Å for the fainter sample). The results show that the cluster is clearly α-enhanced (see Table 4.2 and Figure 4.4). In Figure 4.4, we have plotted the derived α-element abundances as a function of the effective temperature of the stars. This helps to inspect for any possible trends of the derived abundances with stellar parameters, hinting to eventual systematic errors of the derived quantities. The figure also shows that cooler stars have better estimated abundances because they are brighter (and thus, have better SNR) and additionally, the lines in their spectra are more pronounced than in warmer stars.

4.4.3   Iron-peak elements - Sc & Ni

The iron-peak elements are predominantly produced in SNe Ia explosions and are expected to trace the [Fe/H] abundance. So is the case with NGC 4372 where we measured [Ni/Fe]$= -0.05 \pm 0.01$ dex from the Ni I line at 6644 Å and [Sc/Fe]$= 0.03 \pm 0.01$ dex from the Sc II lines at 6245 Å and 6604 Å (Figure 4.5). Only the first Sc II line was used for the fainter stars spectroscopic sample.
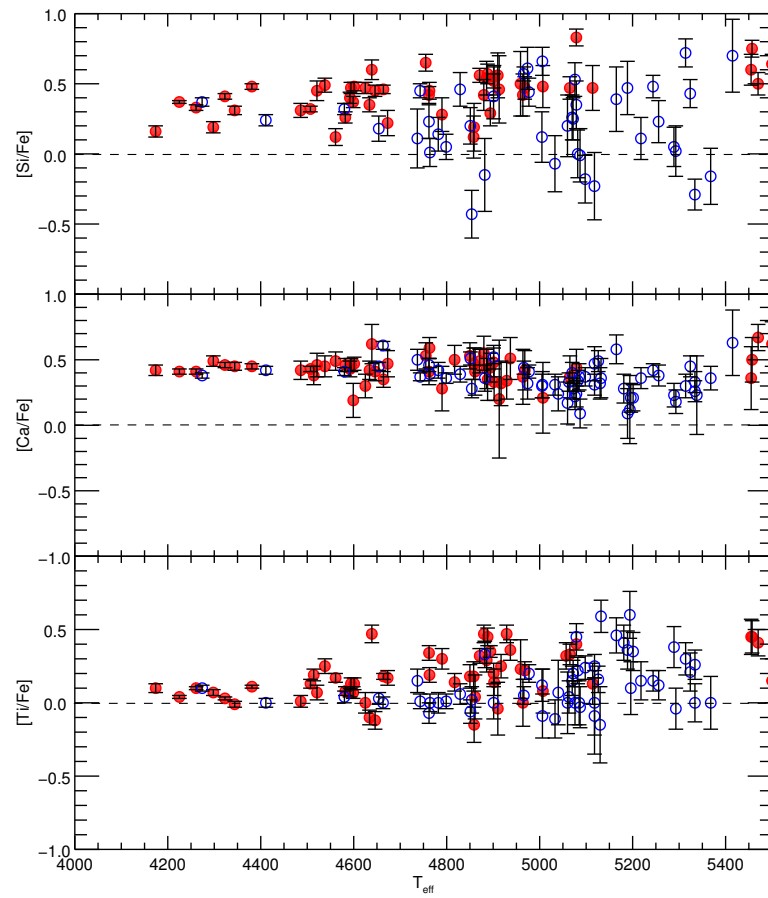
Figure 4.4: α-elements in NGC 4372 as a function of effective temperature. Symbols are as in Figure 4.1.
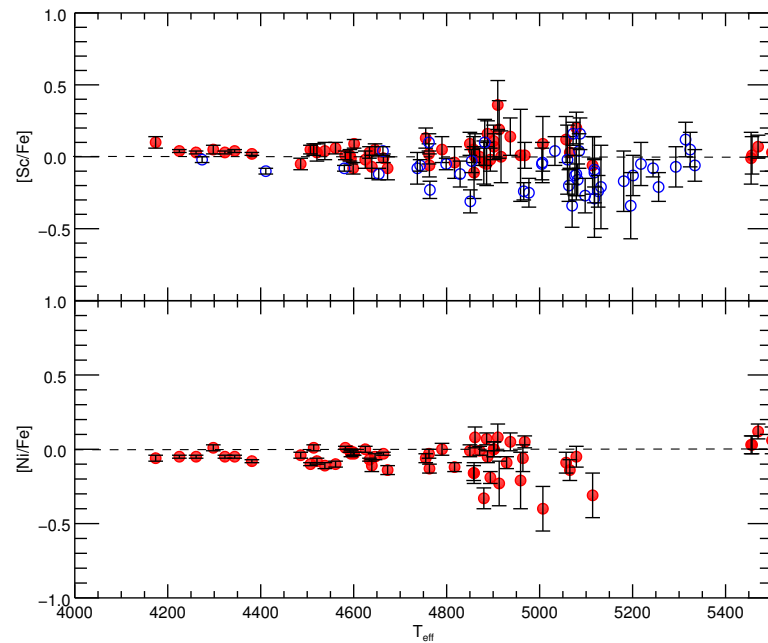
Figure 4.5: Scandium and Ni abundances in NGC 4372 as a function of effective temperature. Symbols are as in Figure 4.1.
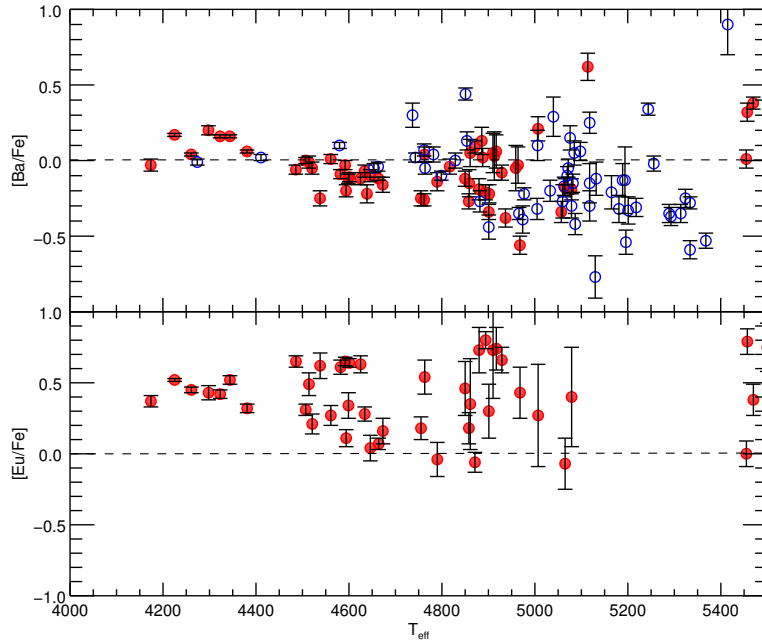
Figure 4.6: Barium and Eu abundances in NGC 4372 as a function of effective temperature. Symbols are as in Figure 4.1.

4.4.4 Neutron-capture elements - Ba & Eu

Barium and Eu are representative for the two main branches of the n-capture processes - slow neutron capturing (s-process) and rapid neutron capturing (r-process) with respect to the β-decay rate. The s-process elements are produced in hot bottom burning in low mass $(2-4\,\mathrm{M_\odot})$ AGB stars and are distributed into the ISM during their final stages of evolution. The r-process, on the other hand occurs during the explosions of SNe type II or neutron star - neutron star mergers. According to Burris et al. (2000) 85% of the Ba in metal poor stars is produced through the s-process and 97% of the Eu comes from the r-process. The [Ba/Eu] ratio is a probe for the weight of each of the two process to the chemical enrichment of any stellar population and thus also the time line of the enrichment due to the different masses of the contributors.

We used the Ba II lines at 6142 Å and 6496 Å to derive Ba abundances in NGC 4372 and the Eu II line at 6645 Å to derive Eu abundances (Figure 4.6). While the mean Ba abundance is slightly sub solar ([Ba/Fe]$= -0.06\pm0.03$ dex), the Eu abundance is clearly enhanced by [Eu/Fe]$= 0.4\pm0.04$ dex, suggesting that NGC 4372 is predominantly r-process enriched. At a metallicity of -2.2 dex, this is to be expected (see Truran 1981; Sneden et al. 2000; Simmerer et al. 2004; Koch et al. 2009).

In Figure 4.7, we show the [Ba/Eu] ratio for the stars with superior quality spectra as a function of the [Na/O] and [Eu/Fe] ratios. We see that there is a bimodality in the [Ba/Eu] ratio as three stars are showing extremely low [Ba/Eu], compatible with enrichment from pure r-process. Interestingly, the anomalous [Ba/Eu] stars do not correlate with the [Na/O] measurements, as we showed in Kacharov et al. (2013) for the GC M 75. It seems that the observed [Ba/Eu] bimodality is not caused by s-process variations but is due to variations in the Eu abundance. Figure 4.8 shows the spectra of two stars with similar atmospheric parameters but different Eu abundances. Although, the available Eu II line is very weak, the difference in its strength in both spectra is clearly visible.

R-process abundance variations have been previously reported in metal poor GCs (see Roederer 2011; Roederer & Sneden 2011). While s-process element variations are found in massive GCs like
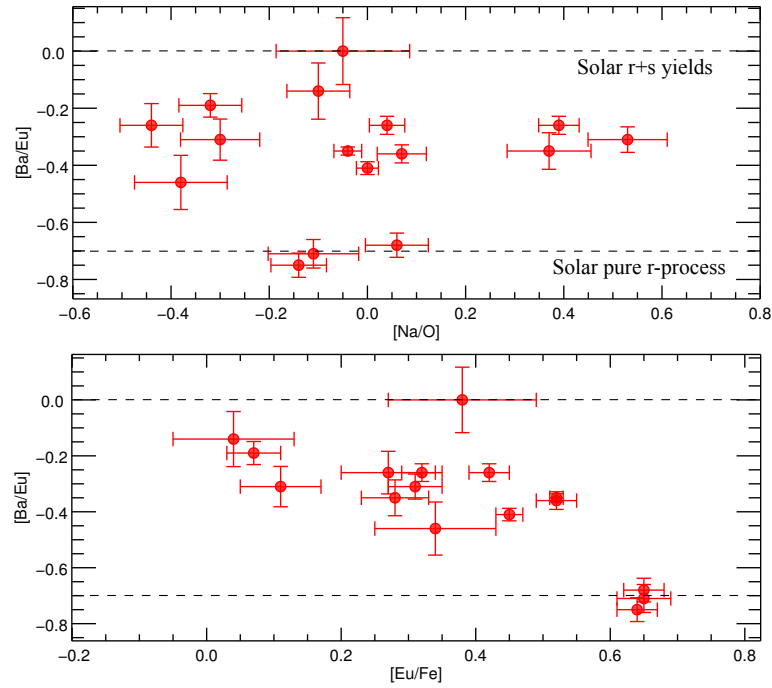
Figure 4.7: The [Ba/Eu] ratio vs. the [Na/O] ratio (*top panel*) and the [Eu/Fe] ratio (*bottom panel*) for the best quality spectra of stars in NGC 4372. The Solar pure r-process and r+s process yields are superimposed for reference.
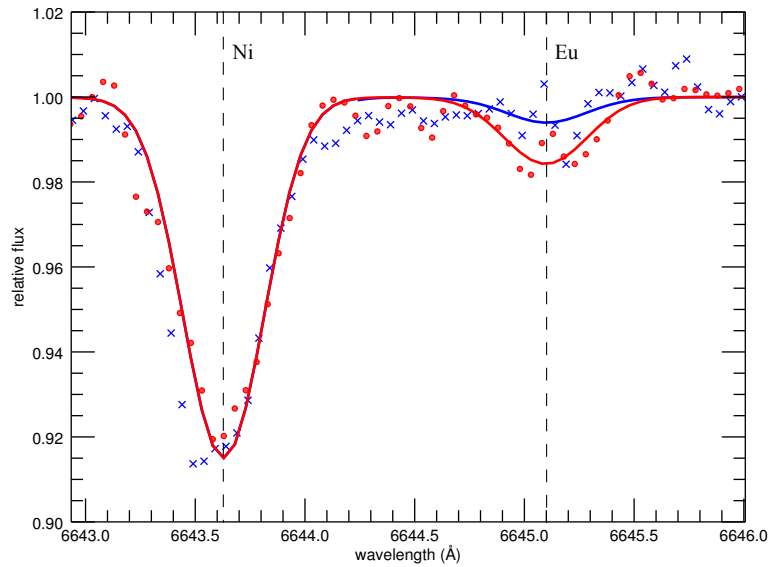
Figure 4.8: The spectra of stars S1856 ([Ba/Eu]$= -0.31 \pm 0.07$ dex, blue asterisks) and I1154 ([Ba/Eu]$= -0.68 \pm 0.04$ dex, red dots) with very similar atmospheric parameters are superimposed for comparison of the Eu line strength. The best fit synthetic spectra are overplotted with blue and red lines, respectively.

M 22 (Marino et al. 2009), NGC 1851 (Carretta et al. 2011b), M 75 (Kacharov et al. 2013) and could be explained in the framework of the various self-enrichment scenarios, the r-process variations are difficult to comprehend within our current understanding of GC formation (see Cohen 2011). The latter are generally attributed to inhomogeneous mixing of the proto-cluster environment.

4.5 Summary

We derived chemical abundances in the GC NGC 4372 by analysing two different spectroscopic samples observed with the FLAMES/GIRAFFE instrument. One of the samples contains predominantly brighter RGB and AGB stars and covers a wavelength range of 6000 - 6700 Å. The other sample consists of fainter RGB stars and covers a wavelength range of 6000 - 6400 Å. We selected cluster member stars based on radial velocity and metallicity constraints.

We used the spectral synthesis tool "Spectroscopy Made Easy" (SME) and the Marcs 2012 spherical, atmospheric models to derive the atmospheric parameters of our stars by fitting various Fe I and Fe II lines. We showed that NGC 4372 has [Fe/H]$= -2.25 \pm 0.01 \pm 0.10$ dex (random and systematic error) with a small spread of 0.06 dex, typical for most GCs. We also used spectral synthesis to derive the abundances of the elements O, Na, Si, Ca, Sc, Ti, Ni, Ba, and Eu.

We demonstrated that, as expected for all Galactic GCs, NGC 4372 exhibits a Na-O anticorrelation - a sign for the existence of at least two chemically distinct stellar populations. The extent of the Na-O anticorrelation in NGC 4372 is relatively small (IQR$_{[Na/O]} = 0.37$ dex) compared to other Galactic GCs but it is consistent with its lower mass ($2.0 \pm 0.5 \times 10^5$ M$_\odot$ Kacharov et al. 2014) and narrow horizontal branch.

NGC 4372 is α-enhanced by $0.43 \pm 0.01 \pm 0.12$ dex and has experienced predominantly r-process enrichment with [Eu/Fe]$= 0.40 \pm 0.04 \pm 0.10$ dex. It is interesting that we detect some star-to-star variation in the Eu abundance of the cluster in accordance with earlier abundance studies of metal poor GCs, but still difficult to explain. Following Roederer (2011), we devote the r-process variations in NGC 4372 to chemical inhomogeneities in the gas cloud from which the cluster formed.

5

The Galactic evolution of sulphur as traced by globular clusters [1]

5.1 Introduction

Sulphur is one of the less studied α-elements (produced by sequential capturing of He nuclei) in stars. In general, the production site of the α-elements such as O, Ne, Mg, Si, S, Ar, Ca, and Ti is mainly associated with the eruptions of type II supernovae (SNe II). In contrast, the major fraction of the iron-peak elements abundance comes from SNe Ia, which contribute little or no α-elements. The different timescales of the occurrence of SNe Ia or II makes the [α/Fe] ratio a powerful tool for diagnosing the chemical evolution and star formation history (SFH) of any stellar population (Tinsley 1979; Matteucci & Brocato 1990; McWilliam et al. 2013). In the Milky Way, the metal-poor stars ([Fe/H] < -1.0 dex) form a plateau at [α/Fe] ~ 0.4 dex. With the onset of SNe Ia, at metallicities above [Fe/H] ~ -1.0 dex, the [α/Fe] ratio starts to gradually drop reaching solar values (McWilliam 1997). In dwarf galaxies that experienced slower star formation, lower values of [α/Fe] are observed even at low metallicities, owing to the lower enrichment rate of the interstellar medium from SNe II (see Shetrone et al. 2001, 2003; Venn et al. 2004; Tolstoy et al. 2009; Hendricks et al. 2014, and references therein). Although different α elements are produced on similar timescales, they show element-to-element scatter due to different production mechanisms, either through hydrostatic burning in the cores of massive stars, or during the SNe explosions themselves. In particular, sulphur (along with Si, Ar, and Ca) is produced during both the O-shell burning and explosive oxygen burning phases (Limongi & Chieffi 2003).

Sulphur is an especially interesting α-element because it is not depleted onto dust (Ueda et al. 2005) and is thus a genuine tracer of the "true" S abundance of the ISM and the stellar photospheres. In fact, sulphur is a preferred tracer of the α abundance in interstellar gas (Garnett 1989; Savage & Sembach 1996) and in high redshift star forming environments such as damped Ly-α systems (Centurión et al. 2000; Nissen et al. 2004; Bowen et al. 2005). The existing sulphur measurements in halo field stars show that the [S/Fe] ratio is increasing with decreasing [Fe/H] at higher metallicities, reaching an average value of about 0.4 dex but its behaviour at lower metallicities is still rather

---

[1]The work presented in this chapter was done in collaboration with Andreas Koch, Elisabetta Caffau, and Luca Sbordone.

controversial. Different studies report either a bimodality of the [S/Fe] ratio with a flat plateau and a branch of increasing abundance, reaching [S/Fe] ~ 0.8 dex, or a plateau with a large scatter (see e.g. Nissen et al. 2004; Caffau et al. 2005a; Nissen et al. 2007; Spite et al. 2011; Jönsson et al. 2011; Matrozis et al. 2013, and references therein).

Globular clusters (GCs) represent the oldest stellar populations in the Milky Way and are examples of very dense environments. Long time considered as simple stellar populations, nowadays we recognize their complex SFH through precise abundance analysis of a variety of chemical elements in individual cluster member stars. All GCs, studied to date, present significant spreads and certain unique correlations in their light and α element abundances – generally taken as a clue for multiple enrichment phases (see the review by Gratton et al. 2012a). Still, sulphur abundances have been derived in very few GCs due to the difficulties that such measurements entail. Sulphur lines in the optical spectral range are generally very weak in giant stars. At the same time, these brighter stars are often the only accessible tracers in remote and faint GCs. To date, the strong multiplet 1 (920 nm) has been used to obtain sulphur abundances in GCs (Caffau et al. 2005b; Sbordone et al. 2009; Koch & Caffau 2011; Caffau et al. 2014) but these lines are often blended with telluric absorption lines and one of them is positioned in the blue wing of the Paschen ζ line and thus cannot always be reliably measured. This makes the Mult. 3 at 1045 nm particularly suited to measure the sulphur abundance. Even if the lines are not as strong as the components of Mult. 1, a big advantage is that there are no telluric features in this wavelength range. Observing the 1045 nm sulphur lines leads to reliable results even at lower metallicities and will give independent and possibly more accurate sulphur abundances in GCs than using Mult. 1 (Caffau et al. 2007, 2010; Jönsson et al. 2011).

The metal-rich GC Ter 7 ([Fe/H] $= -0.32$ dex) is the first GC, for which S abundances were ever derived. The three stars measured by Caffau et al. (2005b) are also the only extragalactic stars with known [S/Fe] ratio, since Ter 7 is associated with the disrupted Sagittarius dSph. Caffau et al. (2005b) determined mean S abundance in Ter 7 slightly lower (by ~ 0.1 dex) than in Galactic stars at similar metallicity. Sbordone et al. (2009) analysed 9 stars in the GC 47 Tuc ([Fe/H] $= -0.72$ dex) and 4 stars in NGC 6752 ([Fe/H] $= -1.54$ dex), deriving [S/Fe] $= 0.18 \pm 0.14$ and [S/Fe] $= 0.49 \pm 0.15$ dex for both GCs, respectively, consistent with the results of field stars. Curiously, Sbordone et al. (2009) reported a star-to-star variation in the observed [S/Fe] ratio in 47 Tuc, which although not significant with respect to the large measurement uncertainties, showed a strikingly clear correlation with the Na abundance. The authors considered different possibilities for the occurrence of such correlation including that S may be involved in the self-enrichment processes of GCs through the $^{31}\mathrm{P}(\mathrm{p}, \gamma)^{32}\mathrm{S}$ proton capture reaction. Koch & Caffau (2011) analysed a single star in the metal-poor GC NGC 6397 ([Fe/H] $= -2.0$ dex), determining [S/Fe] $= 0.52 \pm 0.2$ dex, consistent with the halo filed population.

Here, we present the homogeneous analysis of 15 bright RGB stars in three different GCs that cover together a wide range of metallicities ($-2.3 <$ [Fe/H] < -1.2 dex). Such strategy can provide answers to several basic questions. It is interesting to find out whether a dichotomy or a large spread of the [S/Fe] ratio, as observed in the halo field stars, could also be found in GCs. The generally large uncertainties of the [S/Fe] measurements in the halo field stars are mostly driven by uncertainties of the atmospheric parameters (Matrozis et al. 2013) and thus, tracing the [S/Fe] ratio with GCs will lead to more accurate results due to the much better constrained distances, gravities, and effective temperatures of GC stars from colour-magnitude diagrams (CMD). Additionally, our data will help to check if there are star-to-star variations of the S abundance in the different GCs and whether they correlate with the other α and light element abundances, such as O, Na, Si, Mg, and Al.

The three selected clusters are amongst the closest to the Sun that cover an optimally broad

metallicity range and are all well studied objects. The proximity and simple CMDs of M 4 and M 30 make them desirable candidates for many observational and theoretical studies testing the current stellar evolutionary models. M 30 is also notable for its very low metallicity [Fe/H]$= -2.3$ dex. M 22, on the other hand, is amongst the most massive GCs. It has a very complex CMD with prominent multiple populations and a large metallicity spread ($-1.9 <$ [Fe/H] < -1.6 dex Da Costa et al. 2009; Marino et al. 2009). It is often considered as a remainder of a disrupted dwarf galaxy, similar to ω Cen and M 54, and will thus add another, important comparison object to our study.

Finally, we note the recent work by Caffau et al. (2014), which provides [S/Fe] measurements for several metal-rich open clusters and also includes the GC M 4. Combined with the previous works, the present study provides the largest study of S abundances in star clusters that cover the full range of metallicities of the Milky Way star cluster system.

5.2 Target selection and observations

We chose our targets from existing high-resolution surveys of these GCs in the visible band; M 4 stars were chosen from Marino et al. (2008); M 22 stars from Marino et al. (2009, 2011); M 30 stars from Carretta et al. (2009b,c). Our intentions were to select bright RGB stars that belong to different populations in the selected GCs. To this end, we targeted stars with different Na and O abundances in M 4 and M 30. M 22, on the other hand, is known to harbour stars with a wide metallicity spread, so we selected stars with different [Fe/H]. The adopted stellar parameters of the observed stars from the literature are presented in Table 5.1. Choosing stars for which high-resolution spectroscopy was already available is also important for constraining their atmospheric parameters, such as effective temperature, gravity, microturbulence velocity, and metallicity, necessary for abundance determination. This is only possible if a large set of Fe I and Fe II lines are available, which is not the case with the narrow wavelength coverage of our spectra. Note, however, that the effective temperatures and gravities of the three stars in M 30 were determined photometrically by Carretta et al. (2009b) and likely have larger uncertainties. We still opted to rely on them since these parameters were used to derive abundances of other chemical elements in these stars, with which we aim to compare our S abundance estimates.

The spectra were taken in service mode under Programme ID 091.B-0171(A) with the VLT cryogenic high-resolution infrared echelle spectrograph (CRIRES Kaeufl et al. 2004) mounted at the Nasmyth focus A of the UT1 telescope (Antu). We used the 0.4″ slit, which provides a resolving power $R \sim 50000$ and a dispersion scale on the four parallel, 512 px CCD chips of 0.05 Å px^{-1}. The S I multiplet 3 was centred on chip 3. We used relatively short exposure times (between 30 and 300 s) with a nodding cycle between each exposure. The total integration time was chosen as to achieve a SNR ~ 200 per px in the region of the sulphur lines. In the nodding technique, each star is moved along the slit and exposed at two different positions. This allows for proper sky subtraction and removal of systematic effects, such as amplifier glow. The final, combined spectra are the mean of all short exposures. The science targets were also used as guide stars for the adaptive optics system. The observing log is presented in Table 5.2.

For the data reduction, we used the standard CRIRES pipeline (version 2.3.1) provided by ESO. The pipeline allows dark current subtraction, bad pixel correction, sky subtraction, flat-field correction, non-linearity correction, wavelength calibration from a Th-Ar lamp, and an extraction and combination of the final 1D spectrum from the science images. We noticed that the wavelength calibration was suboptimal due to the very few Th-Ar lamp lines with sufficient brightness available in the observed region, so we additionally refined the wavelength solution using the available stellar lines in the spectra. Finally, the spectra were continuum normalised by fitting the continuum regions with a high order polynomial.

Table 5.1: Atmospheric parameters and [S/Fe] ratios of the targeted stars.

ID	T_{eff}	log g	v_{mic}	[Fe/H]	v_{mac}[4]	[S/Fe]$_{LTE}$
	[K]	[dex]	km s^{-1}	[dex]	km s^{-1}	[dex]
			M 4[1]			
19925	4050	1.20	1.67	−1.02	7.4±0.1	0.41±0.02
21191	4270	1.60	1.60	−1.06	5.5±0.1	0.45±0.02
27448	4310	1.57	1.58	−1.12	6.5±0.1	0.45±0.01
28103	3860	0.50	1.62	−1.08	7.2±0.1	0.50±0.02
34006	4320	1.67	1.61	−1.06	6.3±0.1	0.36±0.02
36215	4300	1.59	1.53	−1.11	6.2±0.2	0.47±0.02
			M 22[2]			
200005	4000	0.05	2.02	−1.94	12.1±0.2	0.65±0.01
200025	4100	0.67	1.80	−1.62	8.9±0.2	0.48±0.02
200031	4300	0.77	1.55	−1.85	8.8±0.2	0.48±0.02
200051	4260	0.90	1.60	−1.63	7.0±0.2	0.52±0.02
200061	4430	1.05	1.70	−1.78	10.9±0.6	0.57±0.03
200068	4500	1.30	1.52	−1.84	8.4±0.3	0.54±0.02
			M 30[3]			
5783	4463	1.17	2.32	−2.33	6.5±0.7	0.60±0.03
10849	4365	0.96	2.34	−2.40	9.1±0.9	0.83±0.04
11294	4258	0.41	2.14	−2.37	9.9±0.4	0.55±0.02

Notes. [1] IDs and atmospheric parameters from Marino et al. (2008).
[2] IDs and atmospheric parameters from Marino et al. (2009).
[3] IDs and atmospheric parameters from Carretta et al. (2009c).
[4] The macroturbulence velocity (v_{mac}) is a free parameter in the fitting procedure.

Table 5.2: Observing log.

ID	V	Date	Exp. time	SNR
	[mag]		[s]	[px^{-1}]
		M 4		
19925	11.04	Jun. 23/24 2013	8 × 60	220
21191	11.70	Sep. 13/14 2013	8 × 120	230
27448	11.73	Sep. 13/14 2013	8 × 120	230
28103	10.71	Apr. 5/6 2013	6 × 60	240
34006	11.87	Sep. 6/7 2013	8 × 120	160
36215	11.80	Sep. 6/7 2013	8 × 120	140
		M 22		
200005	10.92	Jun. 19/20 2013	8 × 60	230
200025	11.52	Jun. 19/20 2013	12 × 60	190
200031	11.64	Jun. 19/20 2013	8 × 120	180
200051	12.04	Jun. 20/21 2013	10 × 120	140
200061	12.21	Aug. 9/10 2013	14 × 180	100
200068	12.30	Aug. 10/11 2013	16 × 120	170
		M 30		
5783[1]	12.71	Jul. 27/28 2013	8 × 300	140
5783[1]	12.71	Aug. 22/23 2013	8 × 300	140
10849	12.55	Jul. 27/28 2013	12 × 300	100
11294	12.09	Aug. 22/23 2013	6 × 300	220

Notes. [1] This star was observed in two nights. The stated SNR is for the combined spectrum of all 16 × 300 s exposures.

5.3   Results and discussion

5.3.1   Spectral synthesis

We derived the S abundance for each of the observed stars through a full spectral synthesis using the LTE code *"Spectroscopy Made Easy"* (SME Valenti & Piskunov 1996). This method is most appropriate when deriving abundances from only a handful of lines because it properly accounts for possible blends. We derived our line list from the VALD database (Kupka et al. 1999, 2000). The transition parameters of the lines in multiplet 3 and the Fe I line at 10470 Å are presented in Table 5.3. Known blends are not an issue in this case. The S I line at 10453 Å is blended with a Fe I line but the latter practically disappears at metallicities below -1 dex. All other transitions on top of the S triplet are of a negligible strength. The region is also free of telluric absorption lines. We used 1D, plane-parallel, atmospheric models interpolated from the Kurucz (1992) grid, readily incorporated within SME. The same models have been used for the derivation of the stellar parameters (Table 5.1). We also tested the Marcs 2012 spherically symmetric models (Gustafsson et al. 2008) but this did not lead to any noticeable changes in the final results.

SME performs a χ^2 minimisation algorithm iterating a defined set of free parameters. In our case, we used the [S/Fe] ratio and the macroturbulence velocity of the stars as free parameters to simultaneously fit the three S lines from multiplet 3 and the only prominent Fe line in the region (see Figures 5.1, 5.2, 5.3). The stellar parameters, as presented in Table 5.1, were kept constant. The goodness of fit of the Fe I line shows the suitability of the input atmospheric parameters, since it is only affected by changes in the broadening parameter – the macroturbulence velocity in this case.

The estimated [S/Fe] ratio in LTE and the best-fit values for the macroturbulence velocity for each star together with the statistical uncertainties are presented in the last two columns of Table 5.1. We used the value of $A(S) = 7.16$ dex as in Caffau et al. (2011) for the Solar abundance of sulphur.

We find very homogeneous [S/Fe] ratios for all 6 stars in M 4 with a mean $[S/Fe]_{LTE} = 0.44 \pm 0.02$ dex with an intrinsic spread $\sigma_0 = 0.04$ dex. The intrinsic spread is calculated as $\sigma_0^2 = \sigma_{[S/Fe]}^2 - < \varepsilon_{rand}^2 >$, where $\sigma_{[S/Fe]}$ is the standard deviation of the [S/Fe] ratio from the mean of all stars and $< \varepsilon_{rand} >$ is the average random error of the individual measurements. The random errors (ε_{rand}) are the formal uncertainties based on the goodness of the χ^2 fit. Five of the observed stars in M 22, regardless of their metallicity, have consistent abundances with a mean $[S/Fe]_{LTE} = 0.52 \pm 0.02$ dex with an intrinsic spread $\sigma_0 = 0.03$ dex. There is only one star (ID 200005) that shows slightly higher $[S/Fe]_{LTE} = 0.65 \pm 0.01$ dex. The situation is similar with M 30. Two stars show consistent [S/Fe] ratios with a mean $[S/Fe]_{LTE} = 0.58 \pm 0.02$ dex and the third one (ID 10849) has an abnormally high $[S/Fe]_{LTE} = 0.83 \pm 0.04$ dex. Note, however, that the derived [S/Fe] ratios are strongly dependent on the effective temperatures and moderately on the gravities, and metallicities of the stars (see Section 3.2). Thus, reasonable changes in the effective temperatures of the stars with abnormal S abundances can bring them in line with the other stars in the sample, e.g. an increase of T_{eff} by 100 K for star 200005 in M 22 and by 200 K for star 10849 in

Table 5.3: Line parameters from VALD.

Element	λ [Å]	χ [eV]	$\log gf$	Damping parameters			Landé factor
				Radiative	Stark	Waals	
S I	10455.449	6.8600	+0.250	8.950	−5.370	−7.333	1.250
S I	10456.757	6.8600	−0.447	8.950	−5.370	−7.333	2.000
S I	10459.406	6.8600	+0.030	8.950	−5.370	−7.333	1.750
Fe I	10469.653	3.8840	−1.187	6.830	−6.150	−7.820	1.170
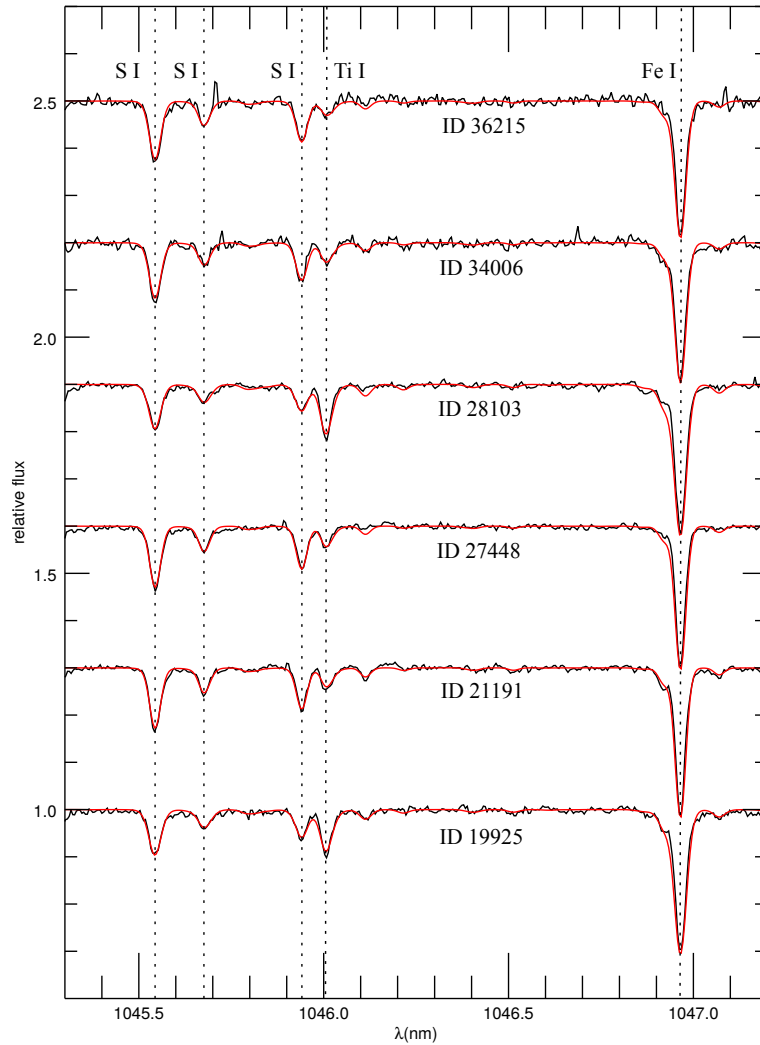
Figure 5.1: Observed (black) and synthetic (red) spectra for the stars in M 4. The most prominent spectral lines are marked with vertical dotted lines. The spectra are shifted vertically by an arbitrary value.

M 30. Star 200005 also has a somewhat lower [Fe/H] estimate – ~ 0.1 dex lower than the mean of the metal-poor population of M 22 (Marino et al. 2009). As it is indicated in Table 5.4, increasing the metallicity of the star by 0.1 dex will bring the [S/Fe] ratio down by 0.06 dex, already in a reasonable agreement with the rest of the stars in M 22. The situation with star 10849 in M 30, which also has the lowest SNR spectrum in our sample is more critical. We do not have solid reasons to believe that the relative estimate of the effective temperature of a star in a homogeneous study could be off by as much as 200 K and it does not present odd abundance of any other element (Carretta et al. 2009c). Therefore, we conclude that, while it is unlikely that these stars show real S abundance peculiarities, further studies of the S abundance in GCs are necessary and should preferably include larger stellar samples.

5.3.2 Systematic uncertainties, NLTE, and 3D effects

In order to estimate the systematic errors of the [S/Fe] ratio caused by uncertainties in the atmospheric parameters of the stars, we chose one star from each GC and varied its T_{eff} by ± 100 K,
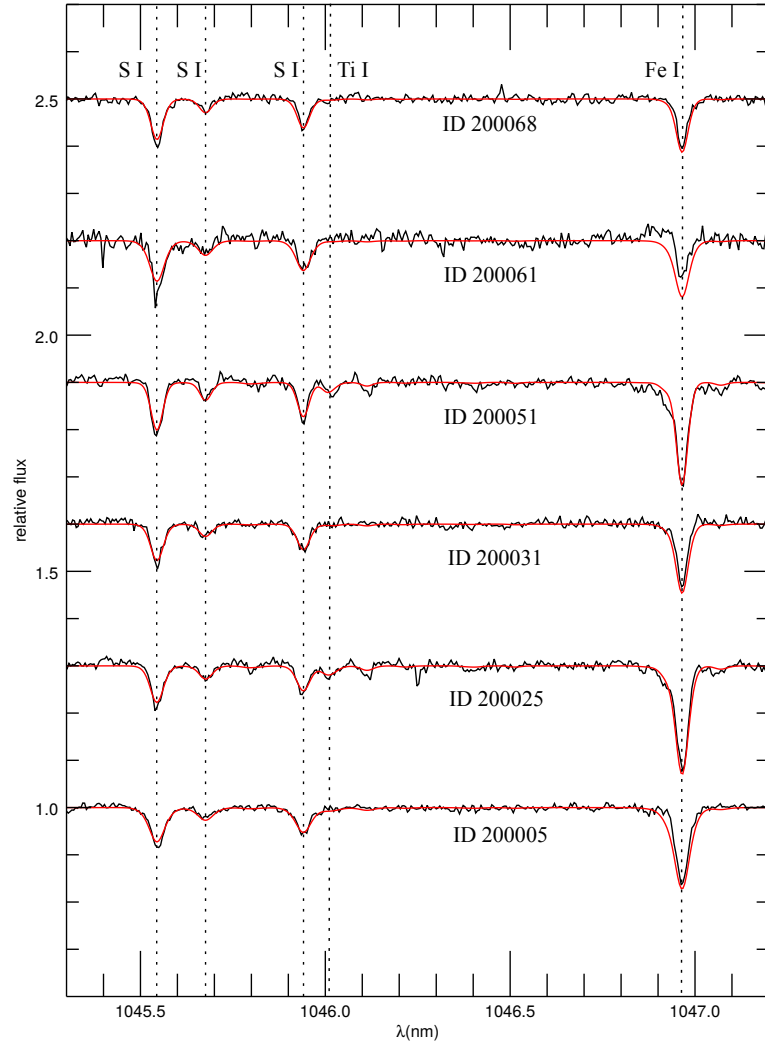
Figure 5.2: Same as Figure 5.1 but for the stars in M 22.

Table 5.4: Systematic uncertainties of [S/Fe].

ID	ΔT_{eff}		$\Delta \log g$		Δv_{mic}		Δ[Fe/H]		total
	+100 K	−100 K	+0.1 dex	−0.1 dex	+0.1 km s^{-1}	−0.1 km s^{-1}	+0.05 dex	−0.05 dex	
27448	−0.16	+0.18	+0.04	−0.04	0.00	0.00	−0.03	+0.03	±0.18
200051	−0.15	+0.16	+0.05	−0.03	−0.01	0.00	−0.02	+0.03	±0.16
11294	−0.13	+0.14	+0.04	−0.05	−0.01	0.00	−0.04	+0.02	±0.14

$\log g$ by ± 0.1 dex, v_{mic} by ± 0.1 km s^{-1}, and [Fe/H] by ± 0.05 dex. These values are very similar to the uncertainties of the atmospheric parameters given in the literature. The results are presented in Table 5.4. In the last column, we list the total systematic error, which is calculated by combining in quadrature the uncertainties caused by different parameters. We note, however, that this is an upper limit of the systematic uncertainties due to covariances of the different parameters (see McWilliam et al. 1995).

The S lines at 1045 nm are affected by relatively large NLTE effects. By extrapolating the NLTE results from the grid of Takeda et al. (2005) to the stellar parameters of our stars, we found $\Delta_{NLTE} = -0.20$ dex, $\Delta_{NLTE} = -0.15$ dex, and $\Delta_{NLTE} = -0.10$ dex for the GCs M 4, M 22, and M 30, respectively. The corrections become smaller for lower metallicities. This increases the small
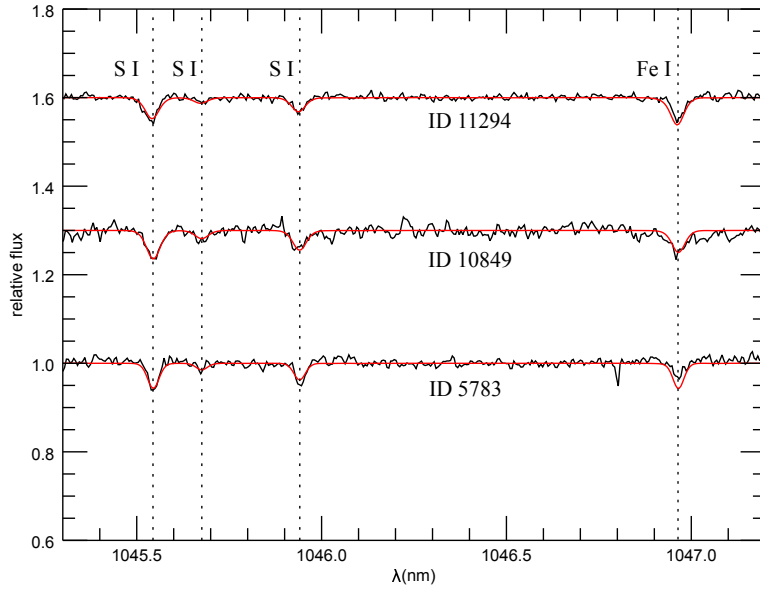
Figure 5.3: Same as Figure 5.1 but for the stars in M 30.

trend observed in LTE that the [S/Fe] slightly rises with decreasing metallicity (see Table 5.1 and Figure 5.5). Considering the large systematic uncertainties, however, the gradual increase of our [S/Fe] ratio with decreasing metallicity is probably insignificant.

According to calculations by Jönsson et al. (2011), based on the 3D model atmospheres of Collet et al. (2007, 2009), the 3D corrections for S abundances derived from multiplet 3 are constant and positive at all metallicities for stars with similar parameters to ours and are in the order of $\Delta_{3D} = +0.20$ dex. Caffau et al. (2007, 2010) explored the 3D effects of multiplet 3 in dwarf stars and also found positive corrections based on the CO^5BOLD 3D model atmospheres. Although it is inconsistent to apply their results to giant stars, there is an agreement that the 3D corrections for the lines at 1045 nm are always positive. In general, the NLTE and 3D corrections for our stars roughly compensate each other and are in the order of the systematic uncertainties.

Finally, the [S/Fe] ratio is relative to the Solar abundance of sulphur and therefore the latter is vital for the proper analysis. We decided to apply the same spectral synthesis technique to the same region of the Kurucz Solar atlas (Kurucz et al. 1984) and derive the LTE Solar abundance of sulphur estimated from multiplet 3 (Figure 5.4). We found $A(S) = 7.26 \pm 0.01$ dex, which is by 0.10 dex higher than the nominal value of $A(S) = 7.16$ dex (Caffau et al. 2011). Our result is, however, consistent with the Solar value estimated by Caffau et al. (2007) using the same lines of multiplet 3 ($A(S) = 7.30$ dex). This finding will systematically decrease our derived abundances in LTE in the three GCs by this amount. However, although the 1D-NLTE and 3D corrections for the Solar abundance derived from multiplet 3 are small and compensating each other – $\Delta_{NLTE} = -0.07$ dex (Takeda et al. 2005) and $\Delta_{3D} = +0.07$ dex (Caffau et al. 2007), it is possible that a NLTE analysis performed in a full 3D synthesis will bring the abundance down to the nominal value. The nominal Solar value is estimated from the S triplet at 675.7 nm and the [S I] line at 1082 nm, which are virtually unaffected by NLTE effects (Caffau et al. 2007; Caffau & Ludwig 2007).

5.3.3   Implications on the Galactic chemical evolution of sulphur

We should be careful when directly comparing the stellar [S/Fe] abundance ratios from different studies because they are based on different methods, different S lines, and different assumptions in their final results. It has been shown that even after proper NLTE treatment, the various S features
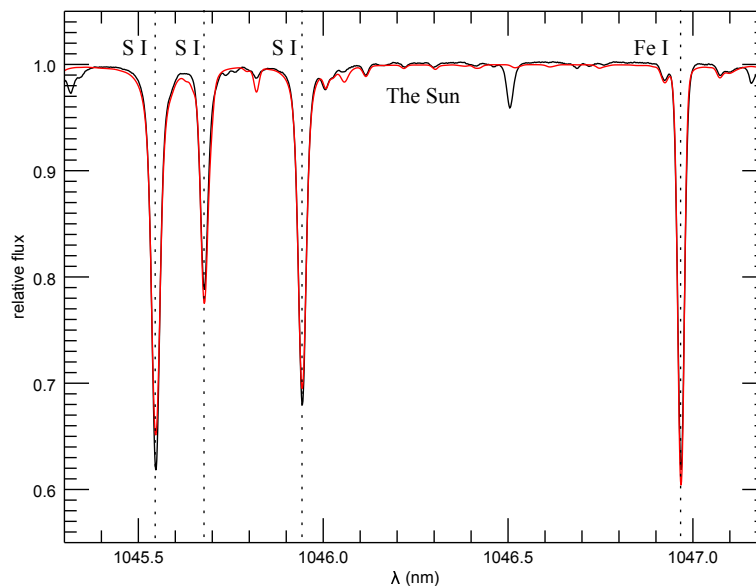
Figure 5.4: The S multiplet 3 region in the Sun fitted using the same technique as for the other stars. We estimate $A(S)_{\mathrm{LTE}} = 7.26$ dex opposed to the adopted value of $A(S) = 7.16$ dex. Symbols are as in Figure 5.1.

could result in offsets in the derived abundances (see Jönsson et al. 2011). Having said that, in Figure 5.5 we have compiled a large collection of known [S/Fe] ratios (references are provided in the figure caption) for Galactic and cluster stars in order to roughly track the evolution of sulphur. All measurements have been shifted to the Solar value of sulphur ($A(S) = 7.16$ dex) adopted in this work and NLTE corrections are applied where applicable. Most of the NLTE corrections come from the calculations of Takeda et al. (2005), except for the extremely metal-poor stars of Spite et al. (2011) who compute their own NLTE corrections. We note that, although the NLTE results by both teams are computed for different types of stars, there are some differences in the overlapping regime. We did not apply 3D corrections in the results plotted in Figure 5.5 in order to be consistent with most of the literature discussions.

There are S abundances derived within the entire span of metallicities covered by stars in Galactic clusters, although the sample is still limited and further studies are desirable. In all analysed clusters, sulphur seems to behave as a typical α element, meaning that the stars in metal-poor Galactic GCs ([Fe/H] < -1.0 dex) have enhanced [S/Fe] abundance ratios and open clusters of solar metallicity have solar [S/Fe] ratios, consistent with the results for Galactic stars and chemical evolutionary models. The only exceptions are Tr 5 discussed in Caffau et al. (2014) and Ter 7 (Caffau et al. 2005b) with anomalously low [S/Fe] ratios. The latter is associated with the Sagittarius dSph galaxy. There are no stars with extremely high S abundances in the GCs as observed in some metal-poor Galactic stars (but note the single exception in M 30) and generally, the spread of sulphur on the metal-poor plateau as traced by cluster stars is smaller than the spread traced by Galactic stars. We already mentioned that our results for the [S/Fe] abundance ratio in M 4, M 22, and M 30 suggest a small trend of increasing [S/Fe] with decreasing metallicity but this is mostly driven by the uncertain NLTE effects for each cluster. It is important to note that we do not find any star-to-star variations in the GCs analysed here (cf. Sbordone et al. 2009).

Messier 4 is the only GC analysed by two teams independently (Caffau et al. 2014, and this work) and a more careful comparison between the results is possible. (Caffau et al. 2014) derive S abundances for 10 stars using line profile fitting of multiplet 1 at 920 nm taking also into account the telluric absorption lines. Although, both studies seem to agree on consistent [S/Fe] abundance ratios
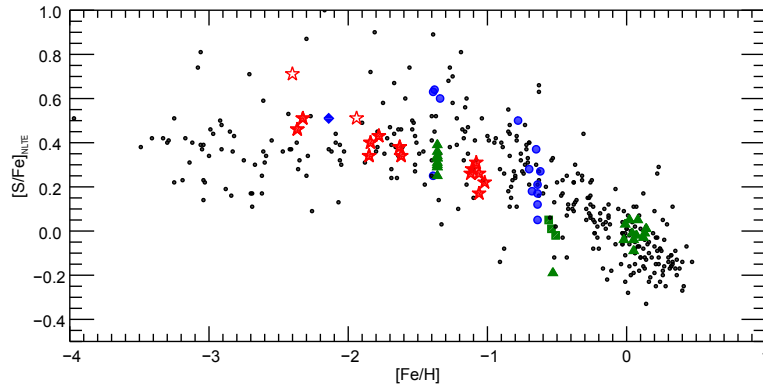
Figure 5.5: NLTE corrected [S/Fe] abundance ratios as a function of metallicity in Galactic disk and halos stars (black dots: Caffau et al. 2005a; Jönsson et al. 2011; Takeda & Takada-Hidai 2011; Spite et al. 2011) and cluster stars (colourful symbols). Blue circles indicate stars from 47 Tuc and NGC 6752 (Sbordone et al. 2009); one star marked with a blue diamond from NGC 6397 (Koch & Caffau 2011); green squares mark stars from Ter 7 (Caffau et al. 2005b); green triangles - stars from M 4, Tr 5, and the open clusters NGC 5822 and NGC 2477 (Caffau et al. 2014); red star symbols denote the results for M 4, M 22, and M 30 from this study; open star symbols denote the stars with abnormal [S/Fe] ratios as discussed in the text. All abundances are referenced to the Solar value of $A(S) = 7.16$ dex.

for this GC (see Figure 5.5), Caffau et al. (2014) assume lower metallicity for their stars, adopting [Fe/H] $= -1.36$ dex for M 4 (Monaco et al. 2012), while the mean [Fe/H] for our stars is -1.08 dex (Marino et al. 2008). This discrepancy results into much lower value of $A(S) = 6.11 \pm 0.04$ dex estimated by Caffau et al. (2014), compared to our estimate of $A(S) = 6.33 \pm 0.02$ dex in NLTE. The NLTE corrections for both multiplets are similar and in the order of 0.2 dex (Takeda et al. 2005). Both studies agree, however, that there is not any significant spread in [S/Fe] amongst the cluster stars.

Finally, we explore the behaviour of sulphur with respect to other light and α elements. One of the goals of this study is to check if star-to-star variations within an individual GC are possible as is the case for elements like C, N, O, Na, Al, and to some extent Mg and Si, which are all correlated between each other (see the review by Gratton et al. 2012a, and references therein). In Figure 5.6 (left panel), we plot existing measurements of [S/Fe] vs. [Na/Fe] for various GCs. In M 4, M 22, and M 30, we have deliberately targeted stars with different Na abundances and Figure 5.6 clearly shows that there is no S-Na correlation between stars from these GCs. So far, with the only tentative exception of 47 Tuc, already discussed in Sbordone et al. (2009), it seems that there are no star-to-star variations of the sulphuric abundance in GCs. We note, however, that we still lack an extensive study that includes a large number of stars in a single GC.
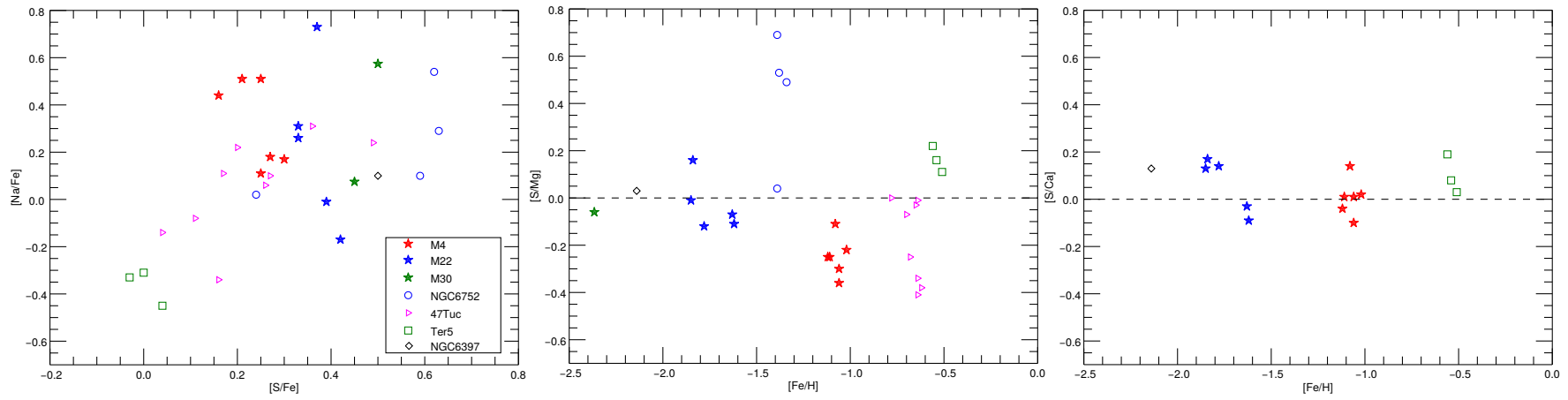
Figure 5.6: A comparison of the S abundances with the abundances of other light and α elements in GCs: [Na/Fe] vs. [S/Fe] (*left panel*); [Fe/H] vs. [S/Mg] (*middle panel*); [Fe/H] vs. [S/Ca] (*right panel*). Different symbols indicate stars from different clusters as indicated in the legend.

In the right panel of Figure 5.6 we show the behaviour of the [S/Ca] ratio in GCs - two α elements carved through the same production channels. The mean ratio is ~ 0.05 dex and there is no trend with metallicity, which suggests that the two elements do evolve in a lock-step, as expected. There is more scatter in the [S/Mg] ratio, although the mean value is 0 dex (Figure 5.6, middle panel). Both elements have slightly different production chains, so the larger scatter is not surprising. In the pre-supernova evolution, Mg is produced in the C-convective shell burning, while S - in the O-convective shell burning. During the explosive nucleosynthesis, Mg is produced in C and Ne burning, while S - in O burning (Limongi & Chieffi 2003). Magnesium could also participate in p-capture reactions through the MgAl cycle and hence star-to-star variations of this element are prominent in some GCs. The behaviour of sulphur with respect to other α elements, as traced by GCs, only strengthens our conclusion that S is a typical α element and no additional sources of production need to be invoked to explain its abundance in stellar photospheres covering a large range of metallicities.

5.4 Summary

Due to the lack of suitable lines to measure sulphur in the visible band at low metallicities, the S abundance measurements in GC stars are quite scarce to date. The present work helps to substantially increase the sample of cluster stars with determined S abundances. We measured the [S/Fe] abundance ratio from multiplet 3 at 1045 nm in 15 RGB stars from three GCs (M 4, M 22, and M 30) observed with the high-resolution, infrared spectrograph CRIRES, mounted at the VLT. The multiplet 3 is suited for S abundance derivation since the three lines are relatively strong even at low metallicity and are free of significant stellar blends and telluric contamination. The selected GCs cover a large range of metallicities ($-2.3 <$ [Fe/H] < -1.0 dex) and the individual RGB targets were specially selected to have different Na & O abundances or even different Fe abundances in the case of the massive GC M 22. This ensured that we have stars belonging to different cluster populations and allowed us to search for possible star-to-star variations of the S abundance in GCs. We used the stellar parameters determined by Marino et al. (2008, 2009, 2011) for the GCs M 4 and M 22, and by Carretta et al. (2009b,c) for the GC M 30 and used the same 1D, plane-parallel, model atmospheres interpolated from the Kurucz grid.

We found [S/Fe]$_{\text{LTE}} = 0.44 \pm 0.02 \pm 0.18$ dex (statistical and systematic error) based on 6 stars in the GC M 4 ([Fe/H] $= -1.06$ dex) without a sign of any star-to-star variations. The NLTE correction based on the grid of (Takeda et al. 2005) is expected to be ~ -0.20 dex at the metallicity of the cluster. In M 22, we obtained [S/Fe]$_{\text{LTE}} = 0.52 \pm 0.02 \pm 0.16$ dex without any significant star-to-stars variations, regardless of the metallicity of the stars ranging from -1.6 to -1.9 dex. One star is found to have slightly higher [S/Fe]$_{\text{LTE}} = 0.65 \pm 0.01$ dex but this could be accounted for if we assume a slightly higher effective temperature of this star by 100 K. The NLTE correction at the metallicity of M 22 is expected to be in the order of -0.15 dex. We measured the S abundances in three stars in M 30 ([Fe/H] $= -2.3$ dex). Two of them show consistent results with a mean [S/Fe]$_{\text{LTE}} = 0.58 \pm 0.03 \pm 0.14$ dex and the third stars shows abnormally high [S/Fe]$_{\text{LTE}} = 0.83 \pm 0.04$ dex. We note, however, that this is the star with the lowest SNR spectrum and at the metallicity of M 30 the lines of multiplet 3 are quite weak. We consider the possibility that this is an erroneous measurement due to some deviations from the true atmospheric parameters of this star and the poor quality data but we cannot undoubtedly exclude the possibility of observing a genuine S-rich star. The NLTE corrections at the metallicity of M 30 are expected to be ~ -0.10 dex. The use of 1D stellar atmospheres instead of 3D models results in an underestimate of the derived [S/Fe] abundance ratios by 0.20 dex at all metallicities. The systematic errors are mainly driven by uncertainties of the effective temperatures of the stars.

Although, we see a small trend of an increase of the [S/Fe] ratio with decreasing metallicity, there is no indication of extremely high S abundances (but note the tentative exception of a single star in M 30) as suggested by the measurements in some field stars (e.g. Caffau et al. 2005a). Considering the large systematic uncertainties, our measurements are consistent with a plateau, as expected for a typical α element. We also find that S varies in a lock step with Ca, a typical α element produced through the same nuclear channels. The mean [S/Mg] ratio is also Solar but with a larger scatter due to the more complex production path of Mg, which could also participate in the self-enrichment processes that take place in GCs.

We conclude that the chemical evolution of sulphur is typical for the genuine α elements as traced from abundances in GCs.

6

Summary & Outlook

6.1 Chemical abundances of Galactic globular clusters

With ages between 10 to 13 Gyr, the Milky Way GCs are amongst the oldest stellar populations in the Galaxy. For a long time they were considered as the best candidates for simple stellar populations. In the last couple of decades, however, an increasing abundance of evidence revealed a very complex nature of these objects - all GCs studied to date contain multiple stellar populations with distinct chemistry and kinematics. It is now established that the unique chemistry of GC stars is coming from pollution with chemically enriched gas, rather than an effect of stellar evolution. To this day, however, the nature of the polluters, the formation sites, and early evolution of GCs remain a mystery.

We presented the first ever comprehensive abundance study of the massive GC M 75 ([Fe/H]= -1.16 ± 0.02 dex) that involved more than 30 chemical elements including a variety of α, p-capture, Fe-peak, and n-capture elements in 16 RGB stars. We showed that, besides the typical light-element variations, M 75 shows a marginal spread in metallicity and likely has a small s-process rich population, similar to its well studied twin GC NGC 1851 (Carretta et al. 2011b). M 75 is an α-enhanced cluster but the majority of its stars show a surprising lack of s-process enrichment for its high metallicity, which hints to a formation in an environment that built metals very quickly and suggests an accretion origin of this GC into the Milky Way halo.

For the first time, we measured abundances of various chemical elements (O, Na, Si, Ca, Sc, Ti, Fe, Ni, Ba, Eu) using a FLAMES high-resolution ($R \sim 22000$), spectroscopic sample in a number of RGB stars in one of the most metal-poor GCs in the Galaxy – NGC 4372. We found a mean metallicity [Fe/H]= -2.25 ± 0.02 dex, a typical α enhancement [α/Fe]= 0.44 ± 0.02 dex, and a predominant r-process enrichment, also typical of objects at that metallicity. Additionally to the expected Na & O variations, we found a tentative indication of Eu spread in NGC 4372. Such r-process variation have been reported before in metal-poor GCs and are generally attributed to chemical inhomogeneities in the gas cloud, from which the cluster formed (Roederer 2011).

We traced for the first time the Galactic evolution of the α element sulphur from GC stars that cover a wide metallicity range ($-2.4 <$ [Fe/H] -1.2 dex). The α element abundances in GCs generally trace the α elements in field stars but the latter show a large scatter in the [S/Fe] ratio in this metallicity span, which is inconsistent with chemical evolution models and poorly understood. We

observed 15 stars belonging to the GCs M 4, M 22, & M 30 with the high-resolution ($R \sim 50000$), infrared spectrograph CRIRES at the VLT. We used spectral synthesis to derive S-abundances from the strong S-triplet at 1045 nm and found that sulphur behaves like a typical α element in the studied GCs, showing enhanced abundances with respect to the Solar value at metallicities below $[\text{Fe/H}] = -1.0$ dex without a considerable spread. But note the tentative exception of a single star in M 30, which has abnormally high S abundance, similar to some peculiar stars found in the halo field population.

6.2   Kinematic properties of Galactic globular clusters

In the past GCs have been viewed as spherically symmetric, non-rotating stellar systems, successfully described to first order by spherical, isotropic models. The increasing abundance of observational data, however, has revealed noticeable deviations from this simple picture. Internal rotation and mild deviation from sphericity often associated with the presence of tidal tails have been observed in most Milky Way GCs.

Our FLAMES spectroscopic sample of the metal-poor GC NGC 4372 contains a total of 131 unique cluster member stars confirmed from radial velocity and metallicity estimates. This allowed us to conduct an in-depth kinematic study of this object. We built a velocity dispersion profile and an intrinsic rotation curve using a discrete maximum likelihood technique, which showed that NGC 4372 has an unusually high ratio of rotation amplitude to central velocity dispersion (1.2 vs. $4.5\,\text{km}\,\text{s}^{-1}$). We also obtained an elliptical number density profile of NGC 4372 based on optical images and showed that NGC 4372 is flattened in the direction of its rotation axis. This suggests that the significant intrinsic rotation is indeed responsible for the cluster's flattening. Finally, we gave a physical interpretation of the observed morphological and kinematic properties of this GC by obtaining an axisymmetric, differentially rotating, dynamical model, which simultaneously fits the observed number density, velocity dispersion, and rotation profiles.

Aiming to better understand the origin of internal rotation in GCs, we showed for the first time that the rotation-to-dispersion (V/σ_0) ratio is well correlated with the half-light to Jacobian radius ratio (r_h/r_J) in the sense that GCs, which better fill their Roche lobes are faster rotators. This is particularly pronounced for the presumably less relaxed young halo GC population. It is a strong evidence that the Galactic tidal field plays a crucial role in shaping GCs and influences their internal kinematics. The more tidally filling GCs are more prone to lose stars and if stars on prograde orbits are preferentially lost, the clusters will gain angular momentum. Alternatively, N-body simulations suggest that stellar tidal streams dissipating from the GC can actually mimic rotation-like signal.

6.3   Outlook

The thesis presented new results for two previously neglected Galactic GCs and gave insights on their possible formation and evolution in the frame-work of the existing GC formation theories. It showed, however, that there are still a number of open questions in our understanding of the formation of these ancient systems. To address these pressing issues, we should be able to look into the sole process of GC formation and to directly observe GCs at different stages of their evolution, spanning a Hubble time. While GCs are no longer forming in the Milky Way, there are a number of young and intermediate-age, massive star clusters found in nearby galaxies with the prospective to become true GCs in the distant future. In the following sections we will outline some possible future paths to explore the mysteries of GC formation and evolution by applying the experience and techniques acquired during the work on the present thesis.

According to the existing GC formation scenarios, it is expected that sufficiently massive star clusters older than a few hundred Myr should also show light element abundance variations. There are a number of $1-3$ Gyr old Large Magellanic Cloud (LMC) clusters with extended or double turn-off regions (Milone et al. 2009), which could be explained by an age spread of $400-500$ Myr (Goudfrooij et al. 2009), in good agreement with predictions of the AGB scenario. Surprisingly, it is now established that these clusters are good representatives of simple stellar populations where no chemical peculiarities have been detected (Mucciarelli et al. 2008, 2014; Colucci et al. 2012).

The SMC provides a unique environment to search for multiple populations in massive intermediate-age clusters that cover a broad age range ($1-10$ Gyr). In particular, it has a unique population of $5-8$ Gyr, massive ($\sim 10^5$ M$_\odot$) clusters present neither in the LMC nor in the Milky Way. We will focus on a subset of these clusters (specifically on clusters for which very deep HST photometry is available and hence have very accurate ages Glatt et al. 2008). The sample also includes two extreme cases - NGC 121 and NGC 419, which will serve as important benchmark objects. NGC 121 is the only typical, old (10.5 ± 0.5 Gyr) GC in the SMC, where multiple populations should be present but no abundance studies have been performed to date. NGC 419, on the other hand, is a young ($\sim 1.2-1.6$ Gyr), massive ($\sim 2 \times 10^5$ M$_\odot$) cluster, and hosts a double turn-off region similar to the intermediate age GCs in the LMC.

Looking for variations in the CN and CH band-strengths of individual cluster stars has been proven to be an efficient and powerful method to detect multiple populations in Galactic GCs, which can be accomplished already at comparatively low spectral resolution (see Harbeck et al. 2003; Kayser et al. 2008; Pancino et al. 2010; Lardo et al. 2012b). The VLT/FORS2 spectrograph is ideal for such observations. This is the easiest way to achieve the goals of the proposed project, namely to search for multiple populations in star clusters at the distance of the SMC (~ 60 kpc). The CN band at 380 nm is sensitive to the N-abundance and the CH band at 430 nm is sensitive to the C-abundance and through a proper treatment of the stellar atmospheres one can derive the [C/H] and [N/H] abundances (Lardo et al. 2012b). They are anti-correlated in stars that belong to differently enriched groups. To ensure the detection of primordial C and N abundance variations, caused by self-enrichment (and not by dredged-up, nuclear processed material), one should target stars belonging to the sub giant branch and the base of the RGB (Kayser et al. 2008).

A further extension of this study will be to observe individual stars in these SMC clusters with high resolution spectroscopic instruments such as FLAMES and UVES, which will give very accurate metallicity estimates and will allow to measure the abundances of more elements, most importantly Na, O, and Al but also a variety of n-capture elements, which will allow to further constrain their chemical evolution.

The investigation of the present day structure and kinematics of individual SMC star clusters, on the other hand, is important to understand the dynamical evolution of the SMC cluster population. Glatt et al. (2009) published an extensive study of the structural parameters of 7 intermediate age and old SMC clusters providing accurate estimates for their core, half-light, and tidal radii, ellipticities, and central densities using number-density and surface brightness profiles obtained from deep HST photometry. They showed that the SMC and LMC massive clusters have similar structures despite the different environment of both galaxies. They are, however, more elliptical, more extended, and less concentrated than the Milky Way GCs. Glatt et al. (2009) argue that these differences are due to the different tidal influence of the parent galaxy. The Milky Way GCs show only mild deviations from the perfect sphere and the reasons for that are not yet fully established. Amongst others, internal rotation and external tides have significant impact.

Therefore, it is important to extend this study to the spectroscopic domain and derive velocity dispersion and rotation profiles for a sample of intermediate-age and old, massive SMC clusters. The relation between the rotation vs. dispersion ratio (V/σ) and ellipticity is a powerful tool to

assess the importance of internal rotation in shaping any stellar systems. Indeed, there is a clear correlation in the V/σ-ellipticity plane for Galactic GCs, despite a large scatter. Considering the large flattening of the SMC clusters, one could expect them to be rotationally supported, although Han & Ryden (1994) showed that they are better represented by triaxial ellipsoids rather than the rotationally supported oblate models representative for the Milky Way GCs. Only the proposed dynamical study can convincingly address the dynamical processes that lead to the present state of the SMC (and ultimately LMC) clusters and explain the observed differences with the Galactic GCs.

We recently discovered that the radial velocity gradient in the Milky Way GCs (usually interpreted as a sign of internal rotation) is well correlated with their half-light to Jacobian radius ratio - a probe of how tidally filling these systems are and hence how influenced they are by the Galactic tidal field. Tidal, stellar streams can also mimic rotation, as suggested by N-body simulations. Extending this study to clusters in more galaxies will bring new insights to our understanding of clusters' dynamics and the influence of different underlying tidal fields to their internal kinematic properties.

The wide field of view of the new VLT IFU instrument MUSE is ideal for such kinematic studies and one can cover the typical SMC clusters out to their half-light radii with a single pointing. The spectral resolution of MUSE ($R \sim 3000$) is not sufficient to measure the velocity dispersion directly from the broadening of the spectral features in the integrated light spectra (IL) as is the common technique. Instead, we can apply a new deconvolution method outlined in Kamann et al. (2013), which allows to extract the spectra of individual stars in crowded fields without blending effects and get radial velocities to a precision of ~ 1 kms^{-1} of an unprecedented number of stars. This method requires a pre-defined catalogue with the positions of all stars in the field, where the available deep HST photometry will be of great benefit. On the other hand, it will be possible to extract velocity gradients caused by rotation or tidal streams directly from the IFU map.

The results will allow us to answer whether multiple populations exist in intermediate age, massive clusters in the SMC, as well as to probe the mass regime (and hence ultimately formation theories) within which abundance anomalies originate. If they show that no clusters with ages < 10 Gyr have chemical spreads, this will point to some unknown physical processes that only occurred at $z > 2 - 3$ or that chemical enrichment only happens in low mass < 1 M$_\odot$ stars, as predicted by the early disc accretion scenario.

Acknowledgements

Bibliography

Alcaino, G., Liller, W., Alvarado, F., & Wenderoth, E. 1991, AJ, 102, 159 (cited on pages 43, 46).

An, D., Beers, T. C., Johnson, J. A., et al. 2012, ApJ, arXiv:1211.7073 (cited on page 2).

Asplund, M., Grevesse, N., Sauval, A. J., & Scott, P. 2009, ARA&A, 47, 481 (cited on pages 22, 69).

Baade, D., Meisenheimer, K., Iwert, O., et al. 1999, The Messenger, 95, 15 (cited on page 46).

Bastian, N., Cabrera-Ziri, I., Davies, B., & Larsen, S. S. 2013a, MNRAS, 436, 2852 (cited on pages 5, 6).

Bastian, N., Lamers, H. J. G. L. M., de Mink, S. E., et al. 2013b, MNRAS, 436, 2398 (cited on pages 4, 7).

Bastian, N. & Silva-Villa, E. 2013, MNRAS, 431, L122 (cited on page 5).

Baumgardt, H., Côté, P., Hilker, M., et al. 2009, MNRAS, 396, 2051 (cited on page 59).

Baumgardt, H., Grebel, E. K., & Kroupa, P. 2005, MNRAS, 359, L1 (cited on page 59).

Baumgardt, H. & Makino, J. 2003, MNRAS, 340, 227 (cited on page 11).

Baumgardt, H., Parmentier, G., Gieles, M., & Vesperini, E. 2010, MNRAS, 401, 1832 (cited on page 62).

Bekki, K. 2010, ApJ, 724, L99 (cited on pages 2, 4, 61).

Bekki, K., Campbell, S. W., Lattanzio, J. C., & Norris, J. E. 2007, MNRAS, 377, 335 (cited on page 6).

Bell, C. P. M., Naylor, T., Mayne, N. J., Jeffries, R. D., & Littlefair, S. P. 2013, MNRAS, 434, 806 (cited on page 8).

Bellazzini, M., Bragaglia, A., Carretta, E., et al. 2012, A&A, 538, 18 (cited on pages 2, 11, 53, 55, 59, 60, 61, 62, 63, 64).

Belokurov, V., Evans, N. W., Irwin, M. J., Hewett, P. C., & Wilkinson, M. I. 2006, ApJ, 637, L29 (cited on page 11).

Bergemann, M., Lind, K., Collet, R., Magic, Z., & Asplund, M. 2012, MNRAS, 427, 27 (cited on pages 16, 23).

Bianchini, P., Varri, A. L., Bertin, G., & Zocchi, A. 2013, ApJ, 772, 67 (cited on pages 11, 12, 43, 55, 57, 59, 60).

Binney, J. 2005, MNRAS, 363, 937 (cited on pages 59, 60).

Binney, J. & Tremaine, S. 1987, Galactic dynamics (Princeton, NJ, Princeton University Press, 1987, 747 p.) (cited on page 9).

Blecha, A., Cayatte, V., North, P., Royer, F., & Simond, G. 2000, SPIE, 4008, 467 (cited on page 44).

Blumenthal, G. R., Faber, S. M., Primack, J. R., & Rees, M. J. 1984, Nature, 311, 517 (cited on page 2).

Boily, C. M. 2000, in Astronomical Society of the Pacific Conference Series, Vol. 211, Massive Stellar Clusters, ed. A. Lançon & C. M. Boily, 190 (cited on page 44).

Bowen, D. V., Jenkins, E. B., Pettini, M., & Tripp, T. M. 2005, ApJ, 635, 880 (cited on page 75).

Bradford, J. D., Geha, M., Muñoz, R. R., et al. 2011, ApJ, 743, 167 (cited on page 10).

Briley, M. M., Bell, R. A., Hesser, J. E., & Smith, G. H. 1994, Canadian Journal of Physics, 72, 772 (cited on page 4).

Bundy, K., Ellis, R. S., & Conselice, C. J. 2005, ApJ, 625, 621 (cited on page 2).

Burris, D. L., Pilachowski, C. A., Armandroff, T. E., et al. 2000, ApJ, 544, 302 (cited on pages 33, 34, 39, 41, 72).

Caffau, E., Bonifacio, P., Faraggiana, R., et al. 2005a, A&A, 441, 533 (cited on pages 76, 84, 87).

Caffau, E., Bonifacio, P., Faraggiana, R., & Sbordone, L. 2005b, A&A, 436, L9 (cited on pages 76, 83, 84).

Caffau, E., Faraggiana, R., Bonifacio, P., Ludwig, H.-G., & Steffen, M. 2007, A&A, 470, 699 (cited on pages 76, 82).

Caffau, E. & Ludwig, H.-G. 2007, A&A, 467, L11 (cited on page 82).

Caffau, E., Ludwig, H.-G., Steffen, M., Freytag, B., & Bonifacio, P. 2011, Sol. Phys., 268, 255 (cited on pages 79, 82).

Caffau, E., Monaco, L., Spite, M., et al. 2014, A&A, 568, A29 (cited on pages 76, 77, 83, 84).

Caffau, E., Sbordone, L., Ludwig, H.-G., Bonifacio, P., & Spite, M. 2010, Astronomische Nachrichten, 331, 725 (cited on pages 76, 82).

Campbell, S. W., D'Orazi, V., Yong, D., et al. 2013, Nature, 498, 198 (cited on page 4).

Cardelli, J. A., Clayton, G. C., & Mathis, J. 1989, ApJ, 345, 245 (cited on page 47).

Carollo, D., Beers, T. C., Lee, Y. S., et al. 2007, Nature, 450, 1020 (cited on pages 2, 19).

Carretta, E., Bragaglia, A., Gratton, R., D'Orazi, V., & Lucatello, S. 2009a, A&A, 508, 695 (cited on pages 5, 29).

Carretta, E., Bragaglia, A., Gratton, R., D'Orazi, V., & Lucatello, S. 2011a, A&A, 535, 121 (cited on page 36).

Carretta, E., Bragaglia, A., Gratton, R., & Lucatello, S. 2009b, A&A, 505, 139 (cited on pages 2, 4, 31, 77, 86).

Carretta, E., Bragaglia, A., Gratton, R. G., et al. 2009c, A&A, 505, 117 (cited on pages 2, 4, 31, 36, 37, 38, 61, 69, 77, 78, 80, 86).

Carretta, E., Bragaglia, A., Gratton, R. G., et al. 2010, A&A, 516, A55 (cited on page 3).

Carretta, E. & Gratton, R. 1997, A&AS, 121, 95 (cited on page 29).

Carretta, E., Gratton, R., Bragaglia, A., D'Orazi, V., & Lucatello, S. 2012, A&A, 2012arXiv1212.1169C (cited on pages 36, 37).

Carretta, E., Gratton, R. G., Lucatello, S., et al. 2010, ApJ, 722, 1 (cited on page 40).

Carretta, E., Lucatello, S., Gratton, R. G., Bragaglia, A., & D'Orazi, V. 2011b, A&A, 533, 69 (cited on pages 3, 5, 38, 39, 41, 73, 89).

Casetti-Dinescu, D. I., Girard, T. M., Herrera, D., et al. 2007, AJ, 134, 195 (cited on pages 43, 62).

Casetti-Dinescu, D. I., Girard, T. M., Jílková, L., et al. 2013, AJ, 146, 33 (cited on page 62).

Casetti-Dinescu, D. I., Girard, T. M., Korchagin, V. I., van Altena, W. F., & López, C. E. 2010, AJ, 140, 1282 (cited on page 62).

Castelli, F. & Kurucz, R. L. 2003, IAUS, 210, 20 (cited on page 22).

Catelan, M. 2009, Ap&SS, 320, 261 (cited on pages 2, 60).

Catelan, M., Borissova, J., Ferraro, F. R., et al. 2002, AJ, 124, 364 (cited on pages 19, 20, 24, 29, 34, 36, 40).

Cayrel, R., Depagne, E., Spite, M., et al. 2004, A&A, 416, 1117 (cited on page 32).

Centurión, M., Bonifacio, P., Molaro, P., & Vladilo, G. 2000, ApJ, 536, 540 (cited on page 75).

Charbonnel, C., Chantereau, W., Decressin, T., Meynet, G., & Schaerer, D. 2013, A&A, 557, L17 (cited on page 4).

Chen, C. W. & Chen, W. P. 2010, ApJ, 721, 1790 (cited on pages 11, 48, 59).

Cohen, J. G. 2011, ApJ, 740, L38 (cited on page 73).

Cohen, J. G. & Meléndez, J. 2005, AJ, 129, 303 (cited on pages 1, 5).

Cohn, H. & Hut, P. 1984, ApJ, 277, L45 (cited on page 43).

Collet, R., Asplund, M., & Trampedach, R. 2007, A&A, 469, 687 (cited on page 82).

Collet, R., Nordlund, Å., Asplund, M., Hayek, W., & Trampedach, R. 2009, Mem. Soc. Astron. Italiana, 80, 719 (cited on page 82).

Colucci, J. E., Bernstein, R. A., Cameron, S. A., & McWilliam, A. 2012, ApJ, 746, 29 (cited on pages 5, 6, 91).

Côté, P., Marzke, R. O., West, M. J., & Minniti, D. 2000, ApJ, 533, 869 (cited on page 2).

Cottrell, P. L.; Da Costa, G. S. 1981, ApJ, 245, 79 (cited on page 5).

Cowan, J. J., Pfeiffer, B., Kratz, K.-L., et al. 1999, ApJ, 521, 194 (cited on page 34).

Cutri, R. M., Skrutskie, M. F., van Dyk, S., et al. 2003, VizieR Online Data Catalog, 2246 (cited on pages 44, 66).

Da Costa, G. S. 1982, AJ, 87, 990 (cited on page 10).

Da Costa, G. S., Held, E. V., Saviane, I., & Gullieuszik, M. 2009, ApJ, 705, 1481 (cited on page 77).

D'Antona, F., Bellazzini, M., Caloi, V., et al. 2005, ApJ, 631, 868 (cited on pages 3, 34, 36).

D'Antona, F. & Caloi, V. 2004, ApJ, 611, 871 (cited on page 36).

D'Antona, F., Caloi, V., Montalbán, J., Ventura, P., & Gratton, R. 2002, A&A, 395, 69 (cited on pages 2, 4, 34, 36, 61).

D'Antona, F., Gratton, R., & Chieffi, A. 1983, Mem. Soc. Astron. Italiana, 54, 173 (cited on page 5).

D'Antona, F., Ventura, P., Decressin, T., Vesperini, E., & D'Ercole, A. 2014, MNRAS, 443, 3302 (cited on page 8).

Davies, R. L., Efstathiou, G., Fall, S. M., Illingworth, G., & Schechter, P. L. 1983, ApJ, 266, 41 (cited on page 59).

Davoust, E. 1986, A&A, 166, 177 (cited on page 11).

De Mink, S. E., Pols, O. R., Langer, N., & Izzard, R. G. 2009, A&A, 507, 1 (cited on pages 4, 7).

Decressin, T., Meynet, G., Charbonnel, C., Prantzos, N., & Ekström, S. 2007, A&A, 464, 1029 (cited on pages 4, 6, 7, 61).

Dejonghe, H. 1987, MNRAS, 224, 13 (cited on page 53).

Denisenkov, P. A. & Denisenkova, S. N. 1989, A.Tsir., 1538, 11 (cited on page 30).

D'Ercole, A., D'Antona, F., & Vesperini, E. 2011, MNRAS, 415, 1304 (cited on page 36).

D'Ercole, A., Vesperini, E., D'Antona, F., McMillan, S. L. W., & Recchi, S. 2008, MNRAS, 391, 825 (cited on pages 4, 5, 31, 33, 36, 61).

Dinescu, D. I., Girard, T. M., & van Altena, W. F. 1999, AJ, 117, 1792 (cited on page 62).

Dinescu, D. I., Girard, T. M., van Altena, W. F., & López, C. E. 2003, AJ, 125, 1373 (cited on page 62).

Djorgovski, S. & King, I. R. 1984, ApJ, 277, L49 (cited on page 10).

Dotter, A., Sarajedini, A., Anderson, J., et al. 2010, ApJ, 708, 698 (cited on page 2).

Eggen, O. J., Lynden-Bell, D., & Sandage, A. R. 1962, ApJ, 136, 748 (cited on page 2).

Elson, R. A. W., Fall, S. M., & Freeman, K. C. 1987, ApJ, 323, 54 (cited on page 8).

Emsellem, E., Cappellari, M., Krajnović, D., et al. 2011, MNRAS, 414, 888 (cited on page 59).

Erben, T., Schirmer, M., Dietrich, J. P., et al. 2005, Astronomische Nachrichten, 326, 432 (cited on page 46).

Ernst, A., Glaschke, P., Fiestas, J., Just, A., & Spurzem, R. 2007, MNRAS, 377, 465 (cited on page 44).

Ernst, A. & Just, A. 2013, MNRAS, 429, 2953 (cited on pages 9, 62).

Fabbian, D., Nissen, P. E., Asplund, M., Pettini, M., & Akerman, C. 2009, A&A, 500, 1143 (cited on page 23).

Fiestas, J., Spurzem, R., & Kim, E. 2006, MNRAS, 373, 677 (cited on page 11).

Forbes, D. A. & Bridges, T. 2010, MNRAS, 404, 1203 (cited on page 2).

Frebel, A., Christlieb, N., Norris, J. E., et al. 2007, ApJ, 660, 117 (cited on page 34).

Fusi Pecci, F., Ferraro, F. R., Bellazzini, M., et al. 1993, AJ, 105, 1145 (cited on page 60).

Gallino, R., Arlandini, C., Busso, M., et al. 1998, ApJ, 497, 388 (cited on page 38).

García-Hernández, D. A., Manchado, A., Lambert, D. L., et al. 2009, ApJ, 705, 31 (cited on page 39).

Garnett, D. R. 1989, ApJ, 345, 282 (cited on page 75).

Geisler, D., Piatti, A. E., Claria, J. J., & Minniti, D. 1995, AJ, 109, 605 (cited on pages 43, 52).

Geisler, D., Wallerstein, G., Smith, V. V., & Casetti-Dinescu, D. I. 2007, PASP, 119, 939 (cited on page 1).

Gerashchenko, A. N., Kadla, Z. I., & Malakhova, Y. N. 1999, Astronomy Reports, 43, 20 (cited on page 46).

Geyer, E. H., Nelles, B., & Hopp, U. 1983, A&A, 125, 359 (cited on page 59).

Girardi, L., Williams, B. F., Gilbert, K. M., et al. 2010, ApJ, 724, 1030 (cited on pages 20, 21).

Glatt, K., Grebel, E. K., Gallagher, III, J. S., et al. 2009, AJ, 138, 1403 (cited on page 91).

Glatt, K., Grebel, E. K., Sabbi, E., et al. 2008, AJ, 136, 1703 (cited on page 91).

Gnedin, O. Y., Lee, H. M., & Ostriker, J. P. 1999, ApJ, 522, 935 (cited on pages 59, 63).

Gonzalez, G. & Wallerstein, G. 1998, AJ, 116, 765 (cited on page 40).

González Hernández, J. I. & Bonifacio, P. 2009, A&A, 497, 497 (cited on page 66).

Goodwin, S. P. 1997, MNRAS, 286, L39 (cited on pages 59, 60).

Goudfrooij, P., Puzia, T. H., Kozhurina-Platais, V., & Chandar, R. 2009, AJ, 137, 4988 (cited on pages 6, 91).

Governato, F., Willman, B., Mayer, L., et al. 2007, MNRAS, 374, 1479 (cited on page 2).

Gratton, R., Sneden, C., & Carretta, E. 2004, ARA&A, 42, 385 (cited on pages 2, 30).

Gratton, R. G., Bonifacio, P., Bragaglia, A., et al. 2001, A&A, 369, 87 (cited on pages 4, 31).

Gratton, R. G., Carretta, E., & Bragaglia, A. 2012a, A&ARv, 20, 50 (cited on pages 2, 4, 30, 61, 69, 76, 84).

Gratton, R. G., Carretta, E., Bragaglia, A., Lucatello, S., & D'Orazi, V. 2010, A&A, 517, A81 (cited on page 60).

Gratton, R. G., Lucatello, S., Carretta, E., et al. 2012b, A&A, 539, 19 (cited on pages 3, 36, 40).

Gratton, R. G., Lucatello, S., Carretta, E., et al. 2011, A&A, 534, 123 (cited on page 36).

Gray, D. F. 1992, The observation and analysis of stellar photospheres. (cited on page 16).

Gunn, J. E. & Griffin, R. F. 1979, AJ, 84, 752 (cited on page 11).

Gustafsson, B., Edvardsson, B., Eriksson, K., et al. 2008, A&A, 486, 951 (cited on pages 66, 79).

Haisch, Jr., K. E., Lada, E. A., & Lada, C. J. 2001, AJ, 121, 2065 (cited on page 8).

Han, C. & Ryden, B. S. 1994, ApJ, 433, 80 (cited on page 92).

Han, S.-I., Lee, Y.-W., Joo, S.-J., et al. 2009, ApJ, 707, 190 (cited on pages 34, 40).

Harbeck, D., Smith, G. H., & Grebel, E. K. 2003, AJ, 125, 197 (cited on pages 4, 91).

Harris, W. E. 1996, AJ, 112, 1487 (cited on pages 1, 20, 29, 41, 43, 46, 48, 60).

Hartwick, F. D. A. & Hesser, J. E. 1973, ApJ, 186, 1171 (cited on page 46).

Hastings, W. K. 1970, Biometrika, 57, 97 (cited on page 50).

Heiter, U. & Eriksson, K. 2006, A&A, 452, 1039 (cited on pages 16, 23).

Hendricks, B., Koch, A., Lanfranchi, G. A., et al. 2014, ApJ, 785, 102 (cited on pages 70, 75).

Hendricks, B., Stetson, P. B., VandenBerg, D. A., & Dall'Ora, M. 2012, AJ, 144, 25 (cited on page 46).

Huang, W. & Gies, D. R. 2006, ApJ, 648, 580 (cited on page 6).

Ibata, R., Nipoti, C., Sollima, A., et al. 2013, MNRAS, 428, 3648 (cited on pages 10, 59).

Ibata, R. A., Gilmore, G., & Irwin, M. J. 1995, MNRAS, 277, 781 (cited on page 2).

Ishigaki, M. N., Aoki, W., & Chiba, M. 2012a, AIPC, 1480, 379 (cited on page 39).

Ishigaki, M. N., Chiba, M., & Aoki, W. 2012b, ApJ, 753, 64 (cited on page 39).

Ivanov, V. D., Kurtev, R., & Borissova, J. 2005, A&A, 442, 195 (cited on page 1).

Jönsson, H., Ryde, N., Nissen, P. E., et al. 2011, A&A, 530, A144 (cited on pages 76, 82, 83, 84).

Kacharov, N., Bianchini, P., Koch, A., et al. 2014, A&A, 567, A69 (cited on pages 66, 69, 74).

Kacharov, N., Koch, A., & McWilliam, A. 2013, A&A, 554, A81 (cited on pages 3, 5, 72, 73).

Kaeufl, H.-U., Ballester, P., Biereichel, P., et al. 2004, in Society of Photo-Optical Instrumentation Engineers (SPIE) Conference Series, Vol. 5492, Ground-based Instrumentation for Astronomy, ed. A. F. M. Moorwood & M. Iye, 1218–1227 (cited on page 77).

Kamann, S., Wisotzki, L., & Roth, M. M. 2013, A&A, 549, A71 (cited on page 92).

Kayser, A., Hilker, M., Grebel, E. K., & Willemsen, P. G. 2008, A&A, 486, 437 (cited on page 91).

Kelson, D. D. 2003, PASP, 115, 688 (cited on page 20).

Kelson, D. D., Illingworth, G. D., van Dokkum, P. G., & Franx, M. 2000, ApJ, 531, 159 (cited on page 20).

Kim, E., Yoon, I., Lee, H. M., & Spurzem, R. 2008, MNRAS, 383, 2 (cited on page 44).

King, I. R. 1962, AJ, 67, 471 (cited on page 9).

King, I. R. 1966, AJ, 71, 64 (cited on page 9).

Koch, A. & Caffau, E. 2011, A&A, 534, A52 (cited on pages 76, 84).

Koch, A. & Côté, P. 2010, A&A, 517, 59 (cited on pages 19, 21, 32, 39).

Koch, A., Côté, P., & McWilliam, A. 2009, A&A, 506, 729 (cited on pages 1, 19, 21, 30, 32, 33, 39, 40, 72).

Koch, A., Odenkirchen, M., Grebel, E. K., & Caldwell, J. A. R. 2004, Astronomische Nachrichten, 325, 299 (cited on page 47).

Kravtsov, V., Alcaíno, G., Marconi, G., & Alvarado, F. 2007, A&A, 469, 529 (cited on pages 20, 21, 22).

Kroupa, P. 2001, MNRAS, 322, 231 (cited on page 7).

Kupka, F., Piskunov, N., Ryabchikova, T. A., Stempels, H. C., & Weiss, W. W. 1999, A&AS, 138, 119 (cited on pages 66, 69, 79).

Kupka, F. G., Ryabchikova, T. A., Piskunov, N. E., Stempels, H. C., & Weiss, W. W. 2000, Baltic Astronomy, 9, 590 (cited on pages 66, 69, 79).

Küpper, A. H. W., Kroupa, P., Baumgardt, H., & Heggie, D. C. 2010, MNRAS, 407, 2241 (cited on page 11).

Kurucz, R. L. 1992, in IAU Symposium, Vol. 149, The Stellar Populations of Galaxies, ed. B. Barbuy & A. Renzini, 225 (cited on page 79).

Kurucz, R. L., Furenlid, I., Brault, J., & Testerman, L. 1984, Solar flux atlas from 296 to 1300 nm (cited on page 82).

Lane, R. R., Kiss, L. L., Lewis, G. F., et al. 2010, MNRAS, 406, 2732 (cited on pages 53, 59).

Lane, R. R., Kiss, L. L., Lewis, G. F., et al. 2011, A&A, 530, A31 (cited on page 11).

Lane, R. R., Kiss, L. L., Lewis, G. F., et al. 2009, MNRAS, 400, 917 (cited on pages 53, 59).

Langer, G. E., Hoffman, R., & Sneden, C. 1993, PASP, 105, 301 (cited on page 30).

Lardo, C., Bellazzini, M., Pancino, E., et al. 2011, A&A, 525, A114 (cited on pages 2, 4).

Lardo, C., Milone, A. P., Marino, A. F., et al. 2012a, A&A, 541, A141 (cited on pages 2, 4, 5).

Lardo, C., Milone, A. P., Marino, A. F., et al. 2012b, A&A, 541, A141 (cited on page 91).

Lardo, C., Pancino, E., Mucciarelli, A., & Milone, A. P. 2012c, A&A, 548, A107 (cited on page 2).

Larsen, S. S., Brodie, J. P., Forbes, D. A., & Strader, J. 2014a, A&A, 565, A98 (cited on page 5).

Larsen, S. S., Brodie, J. P., Grundahl, F., & Strader, J. 2014b, ApJ, 797, 15 (cited on page 5).

Larsen, S. S., Strader, J., & Brodie, J. P. 2012, A&A, 544, L14 (cited on page 5).

Leaman, R., VandenBerg, D. A., & Mendel, J. T. 2013, MNRAS, 436, 122 (cited on pages 2, 61).

Lee, J.-W., Carney, B. W., & Habgood, M. J. 2005, AJ, 129, 251 (cited on page 40).

Lee, Y.-W., Demarque, P., & Zinn, R. 1990, ApJ, 350, 155 (cited on page 60).

Lee, Y.-W., Demarque, P., & Zinn, R. 1994, ApJ, 423, 248 (cited on page 60).

Lee, Y.-W., Gim, H. B., & Casetti-Dinescu, D. I. 2007, ApJ, 661, L49 (cited on page 2).

Limongi, M. & Chieffi, A. 2003, ApJ, 592, 404 (cited on pages 75, 86).

Lind, K., Asplund, M., Barklem, P. S., & Belyaev, A. K. 2011, A&A, 528, 103 (cited on pages 31, 69).

Lind, K., Bergemann, M., & Asplund, M. 2012, MNRAS, 427, 50 (cited on pages 16, 67).

Lützgendorf, N., Kissler-Patig, M., Gebhardt, K., et al. 2013, A&A, 552, A49 (cited on page 12).

Mackey, A. D., Da Costa, G. S., Ferguson, A. M. N., & Yong, D. 2013, ApJ, 762, 65 (cited on pages 53, 55).

Mackey, A. D. & Gilmore, G. F. 2004, MNRAS, 355, 504 (cited on pages 2, 60).

Mackey, A. D. & van den Bergh, S. 2005, MNRAS, 360, 631 (cited on pages 59, 60, 63).

Mandushev, G., Staneva, A., & Spasova, N. 1991, A&A, 252, 94 (cited on page 53).

Marigo, P., Girardi, L., Bressan, A., et al. 2008, A&A, 482, 883 (cited on pages 20, 21).

Marín-Franch, A., Aparicio, A., Piotto, G., et al. 2009, ApJ, 694, 1498 (cited on pages 2, 41, 61, 62, 63).

Marino, A. F., Milone, A. P., Piotto, G., et al. 2009, A&A, 505, 1099 (cited on pages 3, 73, 77, 78, 80, 86).

Marino, A. F., Sneden, C., Kraft, R. P., et al. 2011, A&A, 532, A8 (cited on pages 5, 77, 86).

Marino, A. F., Villanova, S., Milone, A. P., et al. 2011, ApJ, 730, 16 (cited on page 36).

Marino, A. F., Villanova, S., Piotto, G., et al. 2008, A&A, 490, 625 (cited on pages 3, 77, 78, 84, 86).

Martell, S. L. & Grebel, E. K. 2010, A&A, 519, A14 (cited on page 6).

Martell, S. L., Smolinski, J. P., Beers, T. C., & Grebel, E. K. 2011, A&A, 534, A136 (cited on page 6).

Martin, N. F., de Jong, J. T. A., & Rix, H.-W. 2008, ApJ, 684, 1075 (cited on page 49).

Mashchenko, S. & Sills, A. 2005a, ApJ, 619, 243 (cited on page 59).

Mashchenko, S. & Sills, A. 2005b, ApJ, 619, 258 (cited on page 59).

Mason, B. D., Hartkopf, W. I., Gies, D. R., Henry, T. J., & Helsel, J. W. 2009, AJ, 137, 3358 (cited on page 7).

Mateo, M. 1996, in Astronomical Society of the Pacific Conference Series, Vol. 92, Formation of the Galactic Halo...Inside and Out, ed. H. L. Morrison & A. Sarajedini, 434 (cited on page 2).

Mathis, J. S. 1990, ARAA, 28, 37 (cited on page 47).

Matrozis, E., Ryde, N., & Dupree, A. K. 2013, A&A, 559, A115 (cited on page 76).

Matteucci, F. & Brocato, E. 1990, ApJ, 365, 539 (cited on page 75).

McLaughlin, D. E. & van der Marel, R. P. 2005, ApJS, 161, 304 (cited on pages 8, 10).

McWilliam, A. 1997, ARAA, 35, 503 (cited on page 75).

McWilliam, A., Preston, G. W., Sneden, C., & Searle, L. 1995, AJ, 109, 2757 (cited on pages 21, 25, 66, 69, 81).

McWilliam, A., Rich, R. M., & Smecker-Hane, T. A. 2003, ApJ, 592, 21 (cited on page 32).

McWilliam, A. & Smecker-Hane, T. A. 2005, ApJ, 622, 29 (cited on page 32).

McWilliam, A., Wallerstein, G., & Mottini, M. 2013, ApJ, 778, 149 (cited on pages 21, 75).

Milone, A. P., Bedin, L. R., Piotto, G., & Anderson, J. 2009, A&A, 497, 755 (cited on pages 6, 91).

Milone, A. P., Bedin, L. R., Piotto, G., et al. 2008, ApJ, 673, 241 (cited on page 40).

Milone, A. P., Piotto, G., Bedin, L. R., et al. 2012, A&A, 537, A77 (cited on page 46).

Momany, Y., Vandame, B., Zaggia, S., et al. 2001, A&A, 379, 436 (cited on page 46).

Monaco, L., Villanova, S., Bonifacio, P., et al. 2012, A&A, 539, A157 (cited on pages 5, 84).

Muñoz, R. R., Padmanabhan, N., & Geha, M. 2012, ApJ, 745, 127 (cited on page 50).

Mucciarelli, A., Carretta, E., Origlia, L., & Ferraro, F. R. 2008, AJ, 136, 375 (cited on pages 5, 6, 91).

Mucciarelli, A., Dalessandro, E., Ferraro, F. R., Origlia, L., & Lanzoni, B. 2014, ApJ, 793, L6 (cited on pages 6, 91).

Mucciarelli, A., Origlia, L., Ferraro, F. R., & Pancino, E. 2009, ApJ, 695, L134 (cited on page 5).

Newell, B. & Oneil, Jr., E. J. 1978, ApJS, 37, 27 (cited on page 10).

Nissen, P. E., Akerman, C., Asplund, M., et al. 2007, A&A, 469, 319 (cited on page 76).

Nissen, P. E., Chen, Y. Q., Asplund, M., & Pettini, M. 2004, A&A, 415, 993 (cited on pages 75, 76).

Odenkirchen, M., Grebel, E. K., Rockosi, C. M., et al. 2001, ApJ, 548, L165 (cited on page 11).

Oh, K. S. & Lin, D. N. C. 1992, ApJ, 386, 519 (cited on page 63).

Osborn, W. 1971, OBS, 91, 223 (cited on page 2).

Pancino, E., Rejkuba, M., Zoccali, M., & Carrera, R. 2010, A&A, 524, A44 (cited on page 91).

Pasquini, L., Avila, G., Blecha, A., et al. 2002, Msngr, 110, 1P (cited on pages 44, 65).

Petrovic, J., Langer, N., & van der Hucht, K. A. 2005, A&A, 435, 1013 (cited on page 7).

Pietrinferni, A., Cassisi, S., Salaris, M., & Castelli, F. 2004, ApJ, 612, 168 (cited on pages 46, 67).

Pietrinferni, A., Cassisi, S., Salaris, M., & Castelli, F. 2006, ApJ, 642, 797 (cited on pages 46, 67).

Piotto, G., Bedin, L. R., Anderson, J., et al. 2007, ApJ, 661, 53 (cited on pages 3, 5, 34, 36).

Piotto, G., King, I. R., Djorgovski, S. G., et al. 2002, A&A, 391, 945 (cited on pages 43, 47).

Piotto, G., Milone, A. P., Anderson, J., et al. 2012, ApJ, 760, 39 (cited on pages 3, 34).

Piotto, G., Milone, A. P., Bedin, L. R., et al. 2014, ArXiv e-prints (cited on page 3).

Piotto, G., Villanova, S., Bedin, L. R., et al. 2005, ApJ, 621, 777 (cited on page 34).

Plummer, H. C. 1911, MNRAS, 71, 460 (cited on pages 8, 49, 53).

Portegies Zwart, S. F., McMillan, S. L. W., & Gieles, M. 2010, ARAA, 48, 431 (cited on page 7).

Prantzos, N. & Charbonnel, C. 2006, A&A, 458, 135 (cited on pages 4, 6).

Pritzl, B. J., Venn, A. K., & Irwin, M. 2005, AJ, 130, 2140 (cited on pages 1, 30, 39, 70).

Prochaska, J. X., Naumov, S. O., Carney, B. W., McWilliam, A., & Wolfe, A. M. 2000, AJ, 120, 2513 (cited on page 32).

Pryor, C. & Meylan, G. 1993, in Astronomical Society of the Pacific Conference Series, Vol. 50, Structure and Dynamics of Globular Clusters, ed. S. G. Djorgovski & G. Meylan, 357 (cited on pages 20, 53).

Pumo, M. L., D'Antona, F., & Ventura, P. 2008, ApJ, 672, L25 (cited on pages 4, 6).

Raiteri, C. M., Gallino, R., Busso, M., Neuberger, D., & Kaeppeler, F. 1993, ApJ, 419, 207 (cited on page 33).

Ramírez, I. & Meléndez, J. 2005, ApJ, 626, 465 (cited on page 22).

Ramírez, S. V. & Cohen, J. G. 2003, AJ, 125, 224 (cited on page 40).

Renzini, A. 2008, MNRAS, 391, 354 (cited on page 3).

Richer, H. B., Heyl, J., Anderson, J., et al. 2013, ApJ, 771, L15 (cited on pages 2, 7).

Robin, A. C., Reylé, C., Derrière, S., & Picaud, S. 2003, A&A, 409, 523 (cited on page 45).

Roederer, I. U. 2011, ApJ, 732, L17 (cited on pages 5, 72, 74, 89).

Roederer, I. U. & Sneden, C. 2011, AJ, 142, 22 (cited on pages 5, 72).

Rosenberg, A., Piotto, G., Saviane, I., & Aparicio, A. 2000, A&AS, 144, 5 (cited on page 43).

Ruchti, G. R., Bergemann, M., Serenelli, A., Casagrande, L., & Lind, K. 2013, MNRAS, 429, 126 (cited on pages 23, 67).

Rutledge, G. A., Hesser, J. E., Stetson, P. B., et al. 1997, PASP, 109, 883 (cited on page 43).

Sadakane, K., Arimoto, N., Ikuta, C., et al. 2004, PASJ, 56, 1041 (cited on page 21).

Sana, H., Gosset, E., Nazé, Y., Rauw, G., & Linder, N. 2008, MNRAS, 386, 447 (cited on page 7).

Satoh, C. 1980, PASJ, 32, 41 (cited on page 11).

Savage, B. D. & Sembach, K. R. 1996, ARAA, 34, 279 (cited on page 75).

Sbordone, L., Limongi, M., Chieffi, A., et al. 2009, A&A, 503, 121 (cited on pages 76, 83, 84).

Sbordone, L., Salaris, M., Weiss, A., & Cassisi, S. 2011, A&A, 534, A9 (cited on pages 3, 5).

Schirmer, M. 2013, ApJS, 209, 21 (cited on page 46).

Schlafly, E. F. & Finkbeiner, D. P. 2011, ApJ, 737, 103 (cited on page 47).

Schlegel, D. J., Finkbeiner, D. P., & Davis, M. 1998, ApJ, 500, 525 (cited on pages 20, 47).

Searle, L. & Zinn, R. 1978, ApJ, 225, 357 (cited on pages 2, 60).

Servillat, M., Webb, N. A., & Barret, D. 2008, A&A, 480, 397 (cited on page 43).

Shetrone, M., Venn, K. A., Tolstoy, E., et al. 2003, AJ, 125, 684 (cited on pages 30, 40, 70, 75).

Shetrone, M. D., Côté, P., & Sargent, W. L. W. 2001, ApJ, 548, 592 (cited on pages 30, 40, 70, 75).

Siess, L., Dufour, E., & Forestini, M. 2000, A&A, 358, 593 (cited on page 7).

Simmerer, J., Sneden, C., Cowan, J. J., et al. 2004, ApJ, 617, 1091 (cited on page 72).

Skrutskie, M. F., Cutri, R. M., Stiening, R., et al. 2006, AJ, 131, 1163 (cited on page 46).

Sneden, C., Johnson, J., Kraft, R. P., et al. 2000, ApJ, 536, 85 (cited on pages 33, 34, 40, 72).

Sneden, C. A. 1973, PhD thesis, the University of Texas at Austin (cited on page 21).

Sollima, A., Bellazzini, M., & Lee, J.-W. 2012, ApJ, 755, 156 (cited on page 59).

Spite, M., Caffau, E., Andrievsky, S. M., et al. 2011, A&A, 528, A9 (cited on pages 76, 83, 84).

Stetson, P. B. 1987, PASP, 99, 191 (cited on page 46).

Stetson, P. B. 1993, in IAU Colloq. 136: Stellar Photometry - Current Techniques and Future Developments, ed. C. J. Butler & I. Elliott, 291 (cited on page 46).

Stetson, P. B. 2000, PASP, 112, 925 (cited on page 46).

Stetson, P. B. 2005, PASP, 117, 563 (cited on page 46).

Strom, S. E., Wolff, S. C., & Dror, D. H. A. 2005, AJ, 129, 809 (cited on page 6).

Takeda, Y., Hashimoto, O., Taguchi, H., et al. 2005, PASJ, 57, 751 (cited on pages 81, 82, 83, 84, 86).

Takeda, Y. & Takada-Hidai, M. 2011, PASJ, 63, 537 (cited on page 84).

Tinsley, B. M. 1979, ApJ, 229, 1046 (cited on pages 30, 70, 75).

Tolstoy, E., Hill, V., & Tosi, M. 2009, ARA&A, 47, 371 (cited on pages 30, 39, 70, 75).

Tonry, J. & Davis, M. 1979, AJ, 84, 1511 (cited on page 52).

Trager, S. C., King, I. R., & Djorgovski, S. 1995, AJ, 109, 218 (cited on pages 8, 48).

Travaglio, C., Gallino, R., Arnone, E., et al. 2004, ApJ, 601, 864 (cited on page 33).

Trenti, M. & van der Marel, R. 2013, MNRAS, 435, 3272 (cited on page 58).

Truran, J. W. 1981, A&A, 97, 391 (cited on page 72).

Ueda, Y., Mitsuda, K., Murakami, H., & Matsushita, K. 2005, ApJ, 620, 274 (cited on page 75).

Valcarce, A. A. R. & Catelan, M. 2011, A&A, 533, 120 (cited on page 4).

Valenti, J. A. & Piskunov, N. 1996, A&AS, 118, 595 (cited on pages 66, 79).

van de Ven, G., van den Bosch, R. C. E., Verolme, E. K., & de Zeeuw, P. T. 2006, A&A, 445, 513 (cited on pages 11, 49, 52, 63).

van den Bergh, S. 1994, AJ, 108, 2145 (cited on page 62).

van den Bergh, S. 1999, A&AR, 9, 273 (cited on page 1).

van den Bergh, S. 2008, AJ, 135, 1731 (cited on pages 43, 59).

van den Bergh, S. & Mackey, A. D. 2004, MNRAS, 354, 713 (cited on page 1).

VandenBerg, D. A., Brogaard, K., Leaman, R., & Casagrande, L. 2013, ApJ, 775, 134 (cited on page 2).

Varri, A. L. & Bertin, G. 2012, A&A, 540, A94 (cited on pages 11, 43, 57).

Venn, K. A., Irwin, M., Shetrone, M. D., et al. 2004, AJ, 128, 1177 (cited on pages 39, 70, 75).

Ventura, P., Caloi, V., D'Antona, F., et al. 2009, MNRAS, 399, 934 (cited on pages 3, 40).

Villanova, S., Geisler, D., & Piotto, G. 2010, ApJ, 722, 18 (cited on pages 5, 40).

Walker, M. G., Mateo, M., Olszewski, E. W., et al. 2006, AJ, 131, 2114 (cited on page 52).

White, R. E. & Shawl, S. J. 1987, ApJ, 317, 246 (cited on pages 11, 48, 59).

Wilson, C. P. 1975, AJ, 80, 175 (cited on pages 10, 11).

Worley, C. C. & Cottrell, P. L. 2010, MNRAS, 406, 2504 (cited on page 23).

Worley, C. C., Cottrell, P. L., McDonald, I., & van Loon, J. T. 2010, MNRAS, 402, 2060 (cited on page 23).

Yong, D. & Grundahl, F. 2008, ApJ, 672, L29 (cited on page 5).

Yong, D., Grundahl, F., D'Antona, F., et al. 2009, ApJ, 695, 62 (cited on page 40).

Yong, D., Grundahl, F., Johnson, J. A., & Asplund, M. 2008, ApJ, 684, 1159 (cited on pages 3, 5).

Yong, D., Grundahl, F., & Norris, J. E. 2014, ArXiv e-prints (cited on pages 3, 5).

Yong, D., Karakas, A. I., Lambert, D. L., Chieffi, A., & Limongi, M. 2008, ApJ, 689, 1031 (cited on pages 21, 33, 39, 40).

Zhang, H. W., Gehren, T., Butler, K., Shi, J. R., & Zhao, G. 2006, A&A, 457, 645 (cited on page 32).

Zinn, R. 1993, ASPC, 48, 38 (cited on pages 1, 19).

Zinn, R. 1996, ASPC, 92, 211 (cited on page 1).

Zinn, R. & West, M. J. 1984, ApJS, 55, 45 (cited on pages 29, 61, 62).

Zocchi, A., Bertin, G., & Varri, A. L. 2012, A&A, 539, A65 (cited on pages 11, 43, 59).